Summer 8-15-2016

Actin-Based Feedback Circuits in Cell Migration and Endocytosis

Xinxin Wang
Washington University in St. Louis

WASHINGTON UNIVERSITY IN ST. LOUIS

Department of Physics

Dissertation Examination Committee:
Anders E. Carlsson, Chair
Philip V. Bayly
John A. Cooper
Ralf Wessel
Li Yang

Actin-Based Feedback Circuits in Cell Migration and Endocytosis

by

Xinxin Wang

A dissertation presented to the
Graduate School of Arts & Sciences
of Washington University in
partial fulfillment of the
requirements for the degree of
Doctor of Philosophy

August 2016
St. Louis, Missouri

TABLE OF CONTENTS

LIST OF FIGURES

LIST OF TABLES

ACKNOWLEDGMENTS

I wish to sincerely appreciate Washington University in St. Louis for providing the excellent doctoral program in physics. I owe special thanks to many personnels. Dr. John Cooper and Dr. Brian Galletta kindly offered me valuable experimental data and priceless advices. Dr. Philip Bayly, Dr. Ralf Wessel and Dr. Zohar Nussinov gave me many suggestions during group meetings and committee meetings. My family supported me with anything they can do during my five years in St. Louis. Last but most importantly, I sincerely thank my advisor, Dr. Anders E. Carlsson, for the solid knowledge he taught me, for the exciting career path he opened up for me, and for every bit of the effort and energy he put in my doctoral training.

DEDICATION

to my respected father, Dr. Rui Wang

ABSTRACT OF THE DISSERTATION

Actin-Based Feedback Circuits in Cell Migration and Endocytosis

by

Xinxin Wang

Doctor of Philosophy in Physics

Washington University in St. Louis, 2016

Professor Anders E. Carlsson, Chair

In this thesis, we study the switch and pulse functions of actin during two important cellular processes, cell migration and endocytosis. Actin is an abundant protein that can polymerize to form a dendritic network. The actin network can exert force to push or bend the cell membrane. During cell migration, the actin network behaves like a switch, assembling mostly at one end or at the other end. The end with the majority of the actin network is the leading edge, following which the cell can persistently move in the same direction. The other end, with the minority of the actin network, is the trailing edge, which is dragged by the cell as it moves forward. When subjected to large fluctuations or external stimuli, the leading edge and the trailing edge can interchange and change the direction of motion, like a motion switch. Our model of the actin network in a cell reveals that mechanical force is crucial for forming the motion switch. We find a transition from single state symmetric behavior to

switch behavior, when tuning parameters such as the force. The model is studied by both stochastic simulations, and a set of rate equations that are consistent with the simulations. Endocytosis is a process by which cells engulf extracellular substances and recycle the cell membrane.

In yeast cells, the actin network is transiently needed to overcome the pressure difference across the cell membrane caused by turgor pressure. The actin network behaves like a pulse, which assembles and then disassembles within about 30 seconds. Using a stochastic model, we reproduce the pulse behaviors of the actin network and one of its regulatory proteins, Las17. The model matches green fluorescence protein (GFP) experiments for wild-type cells. The model also predicts some phenotypes that modify or diminish the pulse behavior. The phenotypes are verified with both experiments performed at Washington University and with other groups' experiments. We find that several feedback mechanisms are critical for the pulse behavior of the actin network, including the autocatalytic assembly of F-actin, the negative feedback of F-actin on Las17, and the autocatalytic self-assembly of Las17. These feedback mechanisms are also studied by a simple ordinary differential equation (ODE) model. Finally, we develop a partial differential equation (PDE) model that is more realistic than the ODE model and more computationally efficient than the stochastic model. We use the PDE model to explore the rich spectrum of behaviors of the actin network beyond pulses, such as oscillations and permanent patches. The predictions of the PDE model are of high interest for suggesting future experiments that can test the model.

Chapter 1

INTRODUCTION

Cells depend on an enormous number of regulatory interactions among intracellular components, protein molecules and the external environment. The interactions comprise a complex and extensive network. Through evolution, the network is usually far from random, indicating that some substructures appear much more frequently than random structures. These special structures, known as network motifs [19], perform useful functions for the cell. Two functions are of particular interest to the author, switching and the generation of pulses. In the first part of the thesis (Chapter 2), a possible origin of the switch function in cell migration, mechanics, is studied mathematically. In the second part (Chapters 3 and 4), the pulse function in endocytosis is studied with quantitative models and experimental data.

Actin dynamics plays a major role in driving switching and pulse generation in these two biological processes, cell migration and endocytosis. Actin dynamics is thus the main subject of this thesis. In this chapter, Section 1.1 presents an overview of actin dynamics, cell migration and endocytosis. Next, the switch and pulse functions are conceptually and mathematically described in Sections 1.2 and 1.3. Then, the significant roles of these two functions in cell migration and endocytosis are addressed respectively in Sections 1.4 and 1.5, as well as important experimental and theoretical studies in the literature. Last, the

contribution of this thesis to the cell migration and endocytosis is summarized in Section 1.6.

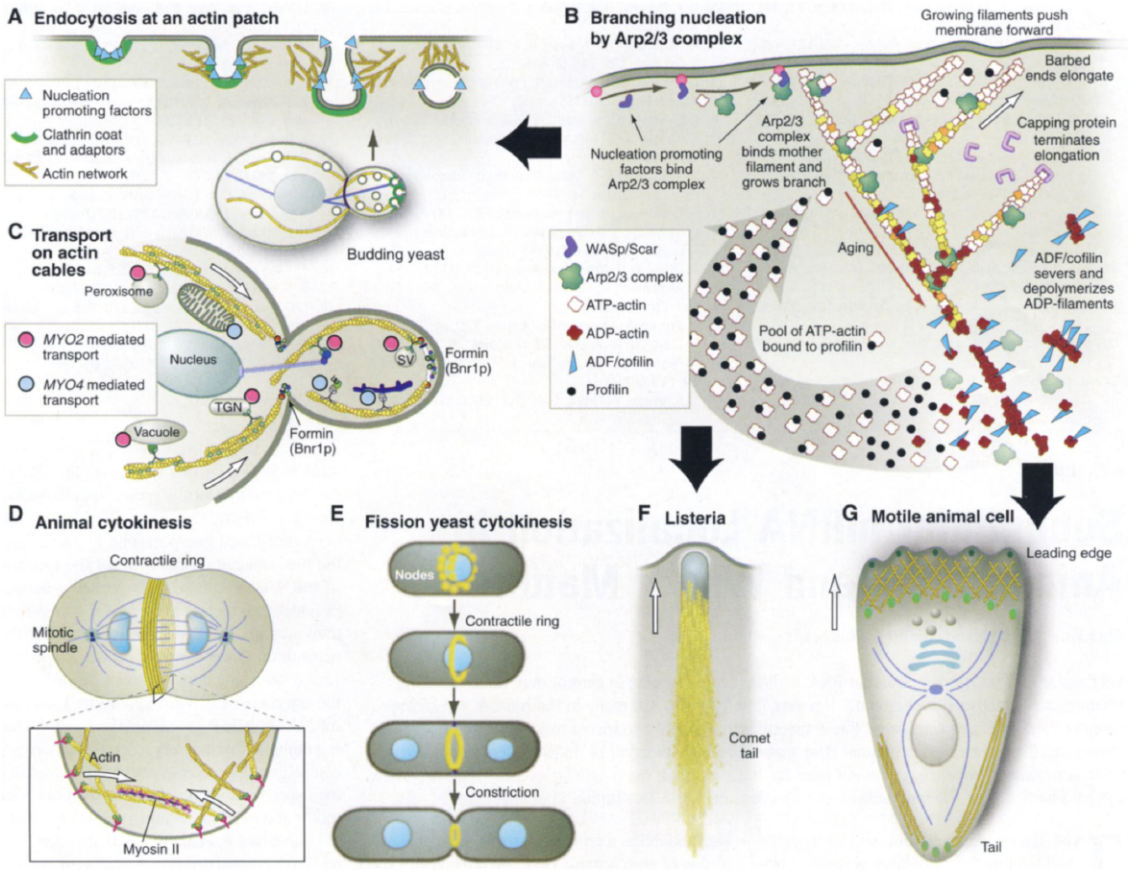

Figure 1.1: Adapted from [1]. **A**, clathrin-mediated endocytosis. **B**, the formation of dendritic actin network via branching by Arp2/3 complex. **C**, membrane-bound vesicles transportation by class V myosins. **D**, contractile ring formed by actin filaments and myosin II in cytokinesis. **E**, condensation of nodes in fission yeast cytokinesis. **F**, *Listeria* bacterium promotes actin network assembly, forming a actin comet tail that push it through the host cell. **G**, cell migration following the leading edge and retracting the tail.

1.1 Overview

Actin is an abundant protein in eukaryotic cells, and is involved in many mechanochemical processes, such as transportation of key substances, cell polarization, and membrane

bending, see Fig. 1.1. Single actin molecules in the cytoplasm, known as monomers, can polymerize into actin filaments. The filaments can form higher-order structures as actin cables, contractile rings, or dendritic networks. The cables serve as trails for intracellular cargo transportation, while contractile rings aid cell division in cytokinesis. On the other hand, the dendritic network plays a central role in cell polarization and membrane bending. Cell polarization can lead to cell migration, while membrane bending is the main process in endocytosis. The roles of actin dynamics in cell migration and endocytosis comprise the core of this thesis.

As shown in Fig. 1.1, when a actin monomer binds to an ATP (adenosine triphosphate) molecule, it can polymerize at one end of an actin filament at a high rate, while polymerizing at the other at a low rate or depolymerizing. The end with high polymerization rate is called the barbed end, and the other end with a low rate is the pointed end. When an ATP-binding monomer is polymerized, it becomes one subunit of the filament. The subunit can hydrolyze ATP at a certain rate and become ADP-binding actin, which is much more loosely bound in the filament. The ADP-binding actin can depolymerize and thus shorten the filament. Depolymerization is favored at the pointed end. This is because the pointed end polymerizes ATP-binding actin slowly, i.e. it is at a lower rate. So the pointed end normally keeps depolymerizing ADP-binding actins that are hydrolyzed some time after being polymerized at the barbed end. Overall, the asymmetry in the polymerization and depolymerization rates causes the actin filament to elongate from the barbed end and shorten from the pointed end. This phenomenon is known as actin treadmilling.

A subunit in an actin filament can also form a base for the polymerization of a new filament via the Arp2/3 (Actin Related Protein) complex. In this context, the existing filament is called the mother filament and the new filament is called the daughter filament. When a mother filament binds an Arp2/3 and an actin monomer, the base is formed. The monomer becomes the first subunit of the daughter filament. This process is dramatically expedited by WASP (Wiskott-Aldrich Syndrome protein). A WASP molecule has a domain that binds and conformationally activates Arp2/3 so that the Arp2/3 can bind the mother filament. WASP also has another domain that can bind actin monomers. WASP domains are discussed in Section 1.5 in more detail. When the initial nucleation process among the WASP, Arp2/3 and mother filament is complete, the WASP will detach from the new formed base. Upon the WASP leaving the base, the daughter filament can start polymerizing [20]. This process is known as branching. One distinctive feature of branching is that the daughter filament has a 70° angle with respective to its mother filament. Thus, after generations of filaments polymerize for some time, a dendritic network of actin is formed, see Fig. 1.2. When the actin network's component filaments polymerize and eventually disappear, the network can treadmill as a coherent entity. All the filaments polymerize roughly in the same direction. Usually, little or no polymerization away from the membrane happens. Then the question is: can the network treadmill against an external force? When a force is exerted on the filaments by an obstacle, the polymerization is reduced by an exponential "Brownian Ratchet" factor [21] but not stalled, unless the force is too large, see details in Chapter 2. Thus, the network is able to keep treadmilling while pushing the obstacle to move in the

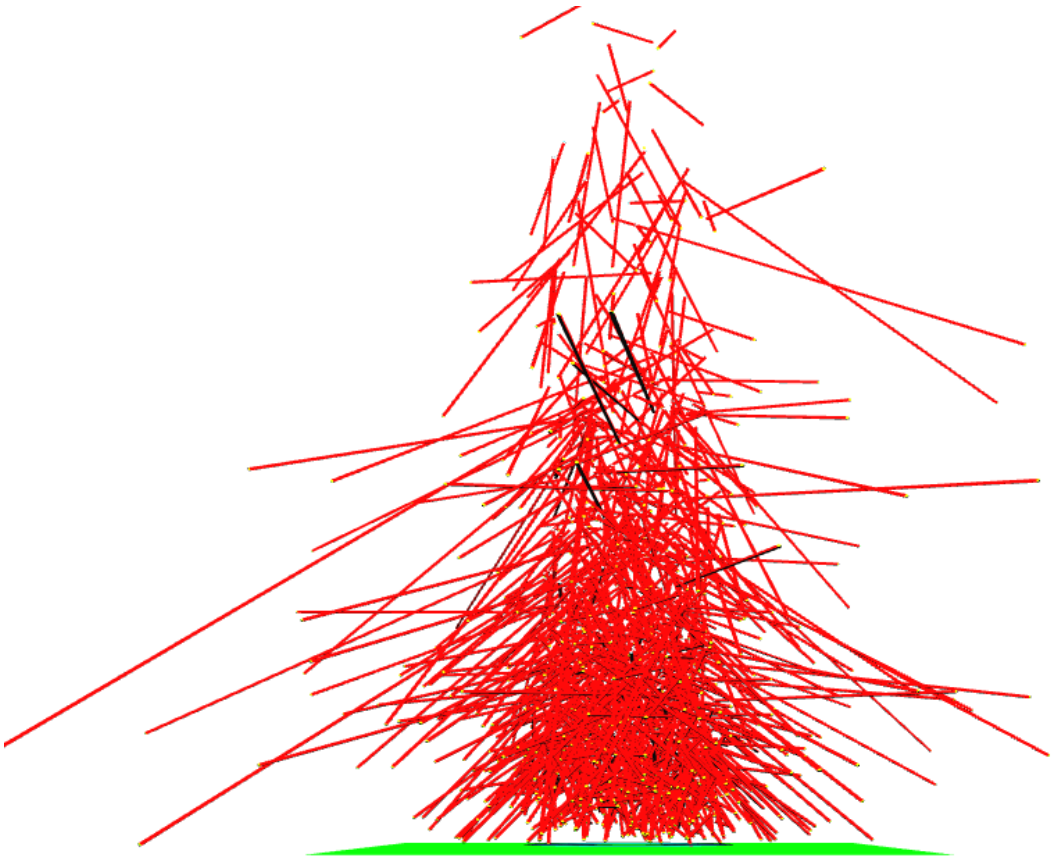

Figure 1.2: Adapted from [2]. A dendritic network of actin. Actin filament is in red. Cell membrane is in green.

same direction [22].

The actin network can also treadmill against the cell membrane and thus move the cell. But this movement is only possible when the majority of the actin network is assembled at one end of the cell instead of being uniformly distributed in the cell, as shown in Fig. 1.1. This broken symmetry of actin network distribution is known as cell polarization. It is not intuitively difficult to understand that the cell can polarize when a directional cue is present, like chemotaxis in a spatial gradient. The chemotactic cue can be sensed by the

cell, which then sends downstream signals for the WASP to control actin assembly according to the direction of the gradient. However, it is observed in many experiments that cells can spontaneously polarize without any directional cue. In addition, the polarization is usually long lasting, see Section 1.4 for details. The spontaneous cell polarization is not intuitively trivial, but rather shares a typical trait of a biological switch. The trait is that a polarized state is stable, which is like one state of a toggle switch. Changing the state requires large fluctuations or a new cue. An important question that is answered in Chapter 2 is why the actin network can behave like a switch and lead to cell polarization, based on mechanical feedback interactions between the actin network and the cell membrane.

The actin network is also important in endocytosis, a process by which cells devour external substances, regulate plasma membrane activities, and recycle membrane components. During endocytosis, the pressure difference across the membrane and the bending force of the membrane must be overcome, see details in Section 1.5. Unlike the case of migration, the actin network pulls the cell membrane inward instead of pushing it. More importantly, no steady state of the network is present in endocytosis, because the network will no longer be needed once the substance reaches inside of the cell or membrane components have been recycled. It usually takes tens of seconds for the actin network to assemble and disassemble. Thus endocytosis is not like a biological switch but a biological pulse. The important questions of why the actin network can behave like a pulse, and what interventions can diminish the pulse, are throughly studied with quantitative models and experiments in Chapters 3 and 4.

1.2 Biological Switches

Cells have various kinds of switches employed in different situations. By activating these switches, the cells can fulfill their biological needs. For example, when *Escherichia coli* (*E. coli*), a human intestine bacterium, is living in an environment that lacks glucose (a preferred sugar), it has to assemble large quantities of enzymes that can assist it to consume other sugars like arabinose. But the enzymes are not required when glucose reappears in the environment. Thus, the states of high or low concentration of the enzymes form a typical biological switch. For another example, flagella, the propeller of many kinds of cells, can rotate in the clockwise or counter-clockwise directions. Switching between the two directions can drive the cells to move forward or backward. There are many types of biological switches that can be tuned between distinctive physical or chemical states [19, 23, 24]. In particular, the migration switch studied in this thesis has two states of the actin network distribution, which are the majority of the network is being assembled at one end of the cell or at the other end.

Usually, the switch is bistable, consisting of two stable states. This means a cell can remain in either of the two states stably until it receives a certain cue or is influenced by a large perturbation to switch to the other state. We thus ask what biological mechanisms lead to such a switch, and what mathematical criteria can describe the mechanism. In this section, we discuss two types of switches, the inhibitor-inhibitor switch and the activator-activator switch.

1.2.1 Inhibitor-Inhibitor Switch

The first type is the inhibitor-inhibitor switch [23], illustrated by the feedback loop in Fig. 1.3. The loop shows an interaction network with two components x and y, which can be regarded as the numbers of two proteins. The numbers are determined by the expression levels of their genes. x and y also label the two transcription factors of the genes. It is assumed that x can bind to a DNA region right before the gene that expresses y. This preceding region is called the promoter of the gene. The binding between x and the promoter of y inhibits y's expression. Likewise, the transcription factor y inhibits x's expression by binding to the promoter of x. The transcription factor and gene interaction is illustrated in Fig. 1.4. From here on in this section, the transcription factor is called the inhibitor for simplicity, to avoid confusion.

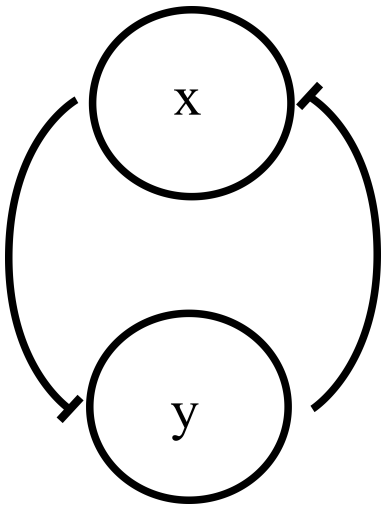

Figure 1.3: The inhibitor-inhibitor switch consists of two genes x and y.

Mathematically, this feedback loop can be written as

$$\begin{aligned} \frac{dx}{dt} &= f(y) - \mu x, \\ \frac{dy}{dt} &= g(x) - \nu y, \end{aligned} \tag{1.1}$$

where $f(y)$ is a monotonically decreasing function of y, and likewise $g(x)$ of x; μ is the disassembly rate of x, and ν is the disassembly rate of y. Now, what forms of $f(y)$ and $g(x)$ are required for the switch?

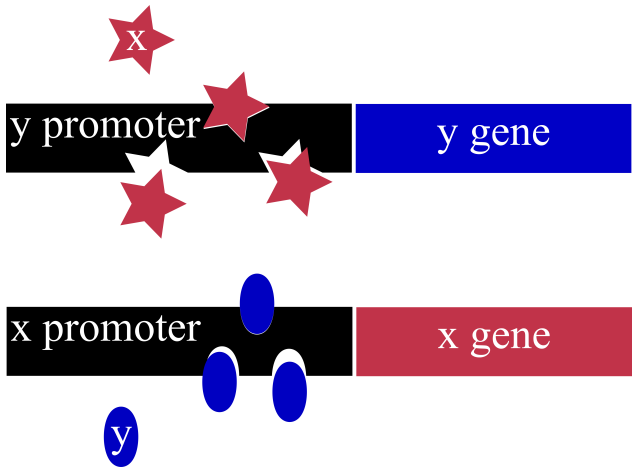

Figure 1.4: The expression of genes x and y is inhibited when three y proteins bind to the x promoter, and three x proteins bind to the y promoter.

Normally the feedback interactions operate within two limits. The first one is the upper limit. Without the inhibitors, the genes are expressed at finite levels x_{max} and y_{max}. The second limit is set by the expression levels of the genes, x_{min} and y_{min}, when the inhibitors are saturated. Often, x_{min} and y_{min} are both taken to be 0. These limits and the monotonically

decreasing feature of $f(y)$ and $g(x)$ are well described mathematically by the Hill functions

$$f(y) = \frac{k_x}{1+y^n},$$
$$g(x) = \frac{k_y}{1+x^n}, \tag{1.2}$$

where k_x and k_y are the assembly rates of x and y respectively, and n characterizes the cooperative binding on the promoter. For $n > 1$, the gene is inhibited only when multiple molecules bind to its promoter, while $n = 1$ is the single binding case. The cooperative binding causes a steeper response curve of the inhibition than the single binding does, see Chapter 3 of [19] for details. In the cooperative binding case, the inhibition of the gene increases very suddenly when the inhibitor reaches a critical value; in the single binding case, the inhibition increases gradually as the inhibitor increases.

A steep response of the gene to its inhibitor is required for switching. To explore this requirement, it is convenient to prove why the single binding case can not form a switch, namely when $n = 1$ in Eq. 1.2. Plugging Eq. 1.2 in the differential equations Eq. 1.1, while letting $n = 1$, we obtain only one steady state or fixed point. The fixed point is where both $\dot{x} = 0$ and $\dot{y} = 0$ on the phase plane of x and y, see [25] for details. The curves $\dot{x} = 0$ and $\dot{y} = 0$ in Eq. 1.1 are called the x nullcline and y nullcline on the phase plane respectively. Thus, the intersection of the two nullclines is nothing but the fixed point.

In the single binding case, the x and y nullclines are $x = \frac{k_x/\mu}{1+y}$ and $y = \frac{k_y/\nu}{1+x}$. The second derivatives of the two nullclines do not change their signs on the phase plane. In other words, they do not change their curving directions (always concave upward). Also,

considering that the two nullclines are monotonically decreasing functions, there is thus at most one intersection, or stable state of the system. But at least two fixed points are needed for the switch, which means the single binding case is disqualified.

However in the multiple binding case ($n > 1$), there could be three fixed points. The nullclines in this case are $x = \frac{k_x/\mu}{1+y^n}$ and $y = \frac{k_y/\nu}{1+x^n}$. Being different from the previous case, the nullclines can change from concave to convex, thus having three intersections or fixed points, see [23] for detailed proof. This scenario is illustrated in Fig. 1.6. Among these fixed points, two are stable, and the other one is unstable. The two stable fixed points then form a biological switch.

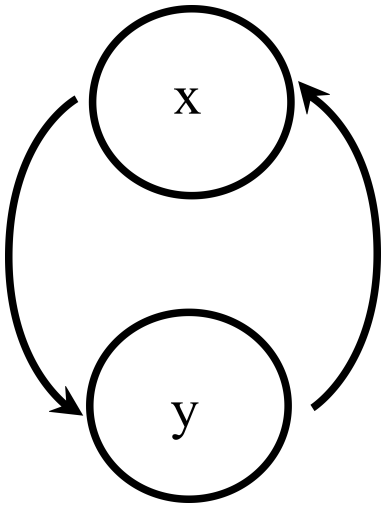

Figure 1.5: The activator-activator switch, consisting of two genes x and y.

To conclude this subsection, two genes inhibiting each other can work together as a biological switch. The inhibition caused by proteins binding gene promoters must be cooperative in order to form the switch. The biological mechanism and its mathematical criterion are

thus clear for the inhibitor-inhibitor switch.

1.2.2 Activator-Activator Switch

The second type is the activator-activator switch. This is also the switch that is studied in the second chapter to explain cell polarization. Unlike the previously discussed inhibitor, an activator can activate a gene's expression by binding to its promoter. The activator is thus another kind of transcription factor. The above analysis still holds if the monotonically decreasing Hill functions are replaced by the monotonically increasing ones below

$$\begin{aligned} f'(y) &= \frac{k'_x y^n}{1+y^n}, \\ g'(x) &= \frac{k'_y x^n}{1+x^n}, \end{aligned} \tag{1.3}$$

where the primes are used to distinguish them from the inhibitors. This switch is shown in Fig. 1.5. When $n > 1$, increasing the parameters k'_x and k'_y, the nullclines give two extra fixed points, see Fig. 1.6. This is known as the blue sky bifurcation. For the inhibitor-inhibitor switch, the bifurcation is the pitchfork bifurcation, also shown in Fig. 1.6. For $n = 1$ in the activator-activator switch, the blue sky bifurcation does not exist because the curving directions of the nullclines do not change. It is thus clear that the biological mechanism behind this switch is the cooperative binding between the gene promoters and the activators. They can cause multiple stable states. This is the activator-activator bistable switch.

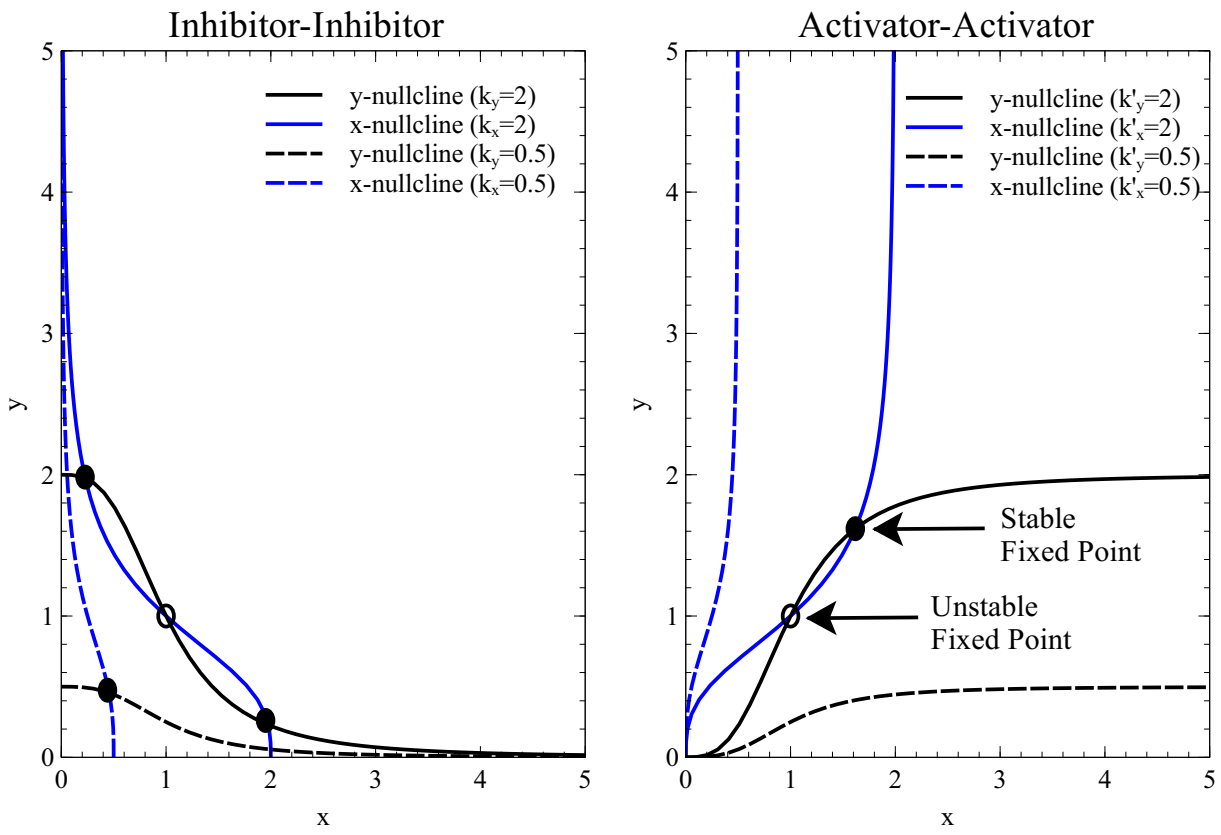

Figure 1.6: The nullclines of two types of switches. The nullclines are for $n = 3$ in both inhibitor-inhibitor and activator-activator switches. The inhibitor-inhibitor switch presents a pitchfork bifurcation when k_x and k_y increase. The activator-activator switch presents a blue sky bifurcation when k'_x and k'_y increase.

1.3 Biological Pulses

Besides the switch, the biological pulse is also an important function needed by cell. Unlike the switch that provides a pair of steady states, a pulse of a physical or chemical quantity in a biological system transiently exceeds a threshold value. The threshold is determined by the nature of the relevant biological processes.

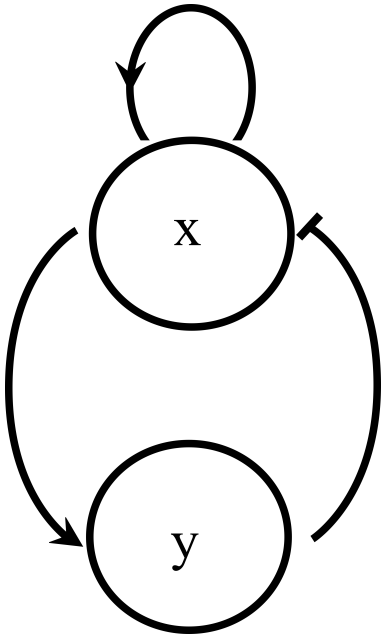

Figure 1.7: Excitable feedback system represents the FitzHugh-Nagumo model, Eq. 1.4. In this feedback loop, the sign of y in Eq. 1.4 is reversed, namely replaced by $-y$.

For example, a voltage difference can activate a neuron only when a certain threshold voltage is reached. Thus, voltage pulses that have maxima higher than the threshold can activate neurons in a sequence. For another example, in order to transport external substance into the cell via endocytosis, yeast needs to assemble a certain amount of force-generating proteins to overcome a large pressure difference across the membrane. The proteins, however, are no longer needed once the vesicle containing the substance is inside the cell. This process is studied throughly in Chapters 3 and 4.

To understand neural information transmission and endocytosis, it is crucial to understand what feedback mechanisms can lead to both transient increase and decrease of the pulse quantities. In Section 1.2, two types of feedback were studied, inhibition and activa-

tion. In this section, it is seen that the combination of one inhibition, one activation and one self-activation (see Fig. 1.7) can lead to pulse behavior. The analysis is based on the FitzHugh-Nagumo model [3, 26], which is written as

$$\begin{aligned} \frac{dx}{dt} &= c\left(x + y - \frac{1}{3}x^3 + z\right), \\ \frac{dy}{dt} &= -\frac{1}{c}\left(x - a + by\right), \end{aligned} \tag{1.4}$$

where the parameters $a = 0.7$, $b = 0.8$ and $c = 3$ are used for the calculation in this section. The other parameter z acts as a constant external stimulus on the system.

First, without the stimulus ($z = 0$), the model gives a single pulse of the two variables if perturbed at the beginning. The perturbation is achieved by setting the initial conditions $x_0 = -0.5$ and $y_0 = -0.5$. The result of a numerical calculation of this scenario using the 4th-order Rung-Kutta method is shown in Fig. 1.8. The nullclines in the figure have one stable fixed point. Immediately following the perturbation away from the fixed point, we see a transient increase of both x and y. Eventually, x and y are absorbed into the fixed point. Therefore, without any external stimulus, an initial perturbation can cause a single pulse in the system.

Second, when the external stimulus is large enough, for example $z = -0.4$ (Fig. 1.8), it drives the system to a limit cycle, and destabilizes the fixed point. The transient increase of x and y thus happens periodically. This transition from a single pulse to an infinite series of pulses is known as the Hopf bifurcation, see [25] for details.

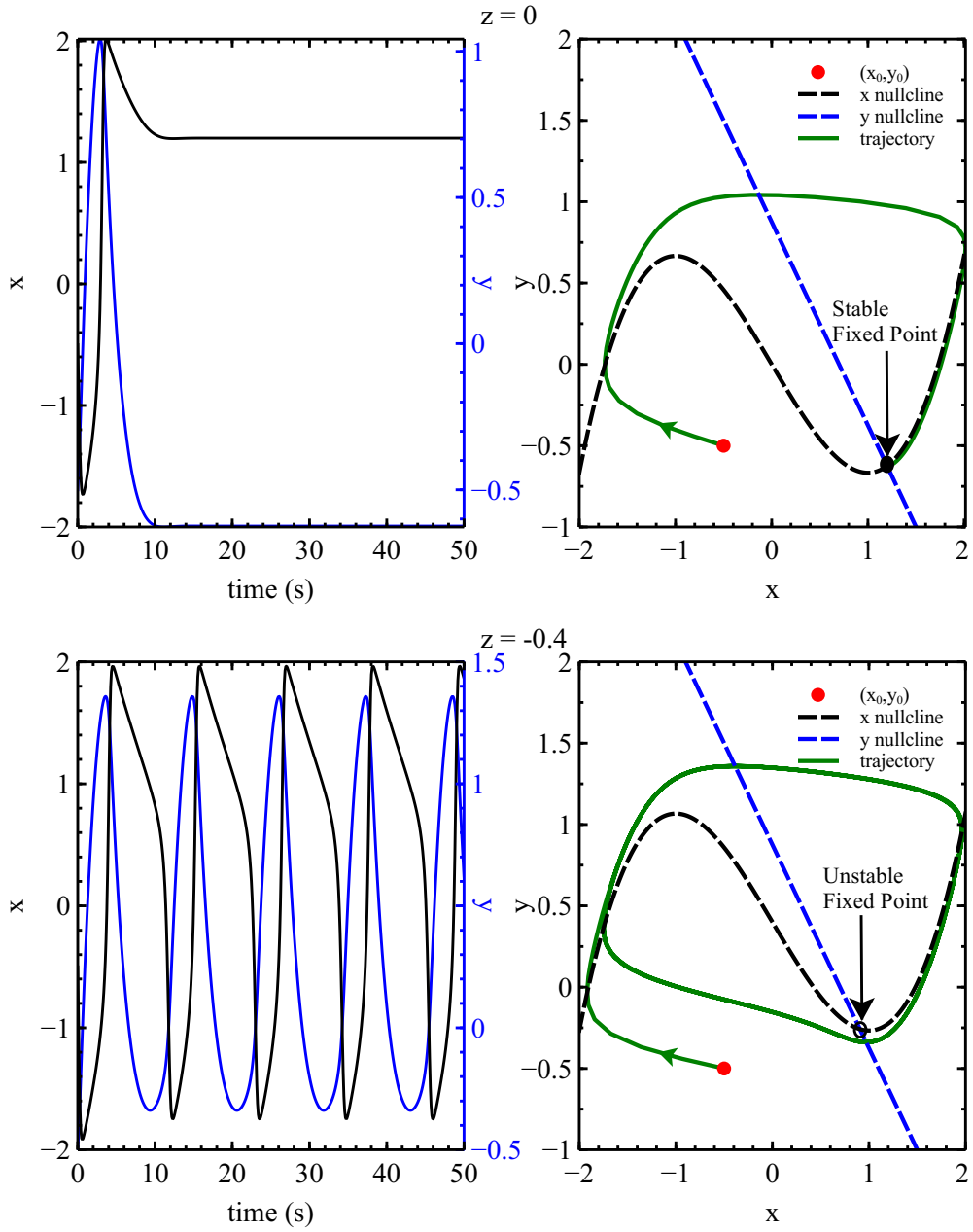

Figure 1.8: Reproduction of the result in [3] by calculating Eq. 1.4. The first row of figures are the time courses (left), and the phase planes (right) when $z = 0$. The phase plane contains the initial position, nullclines and trajectory of the calculation. The same for the second row, except that $z = -0.4$.

It is therefore clear that an inhibitor-activator system can generate pulses if an initial

perturbation occurs, with or without an external stimulus. Such perturbations are very common because the cell is a highly fluctuating system. Also, fluctuations in the environment can serve as an effective perturbation. Either the internal or the external fluctuations are good candidates for the perturbation required by the model. In our studies of endocytosis in Chapters 3 and 4, x and y correspond to actin regulators and actin polymerization.

1.4 Cell Migration

As discussed in the Overview, an actin network can push an obstacle when growing in certain directions. When an actin network grows inside of a cell, the cell membrane can be regarded as the obstacle. The membrane normally accumulates WASP or other regulators on the inner surface, thus promoting the growth of the network. At first glance, all positions on the entire inner surface of the membrane of an initially circular cell should be almost identical. Therefore, it is intuitive to assume that the actin network is also identical everywhere near the inner surface, namely the network is symmetrical. The network thus pushes the membrane in all the directions symmetrically. According to this symmetry of the actin network, there should not be any motion.

However, in several cases this intuitive view is not valid. Firstly, if a directional chemoattractant is present in the environment, the cell can sense the direction. Responding to it, the cell can activate WASP at one end closest to the higher concentration of the chemoattractants, and repress the actin growth at the other end closest to the lower concentration of the chemoattractants. The result of this response is that the network grows more at the first end and less at the other end. After a short while, the majority of the network is present

at the first end, known as the leading edge, which will push the cell in the direction of the chemoattractant. On the other hand, the minority of the network present at the second end, known as the trailing edge, can not push the membrane enough in the opposite direction against the leading edge. Therefore, the cell will move in the same direction as the chemoattractant. Similarly, the cell can respond to directional chemorepellents and move away from them.

But more surprisingly, the actin network symmetry can be broken even without directional chemotaxis. Some cells can spontaneously break the symmetry and thus beginning to move. This spontaneous symmetry breaking (SSB) is studied in Chapter 2. A purely mechanical model proposed in the chapter can lead to SSB.

Several important experiments illustrate SSB as modified by mechanical effects. In Ref. [4], the authors treat fish epidermal keratocytes with drugs that can cause the cells to divide into fragments. The drugs used are either the protein kinase inhibitor staurosporine (100 nM), or the myosin light chain kinase inhibitor KT5926 (20 mM). The resulting fragments in some cases, spontaneously polarize and persistently move in one direction. Others stay stationary or polarize through collision. The results are shown in Fig. 1.9. The time course of distance in the figure reveals a fragment's transition from a stationary state to a motile state. Noticeably, the fragment is clearly moving in one direction without stopping or changing direction for tens of minutes.

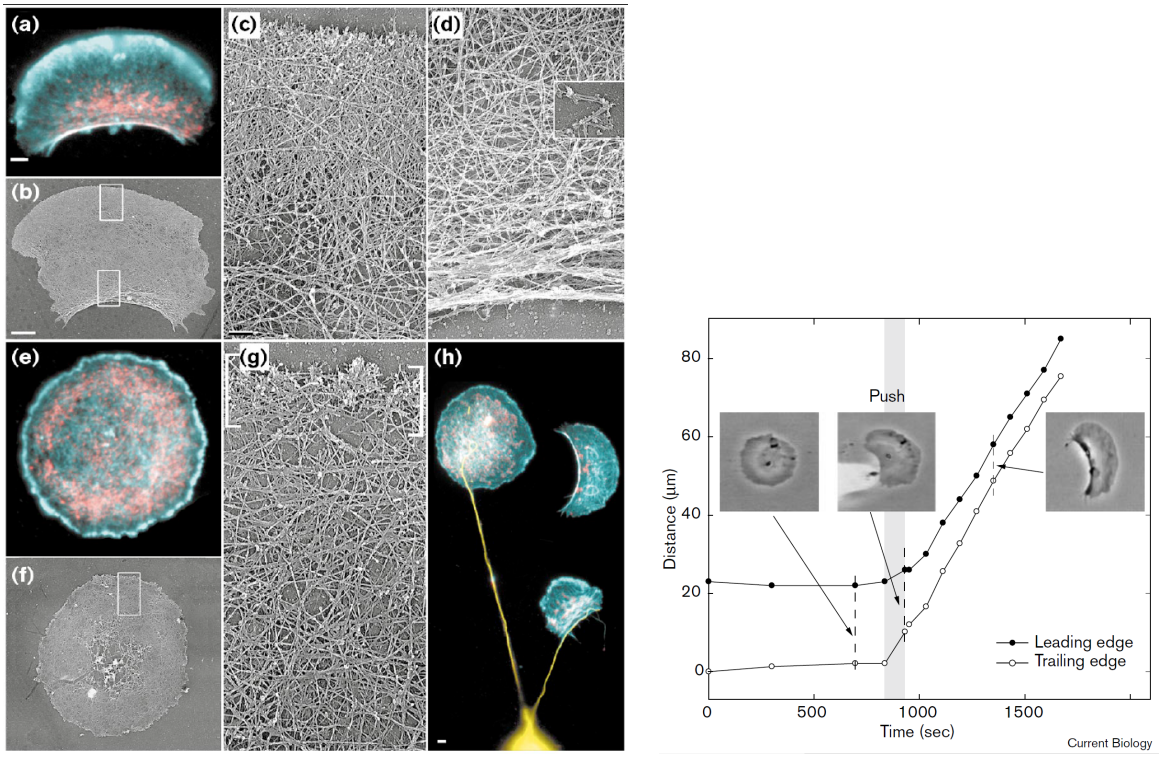

Figure 1.9: Adapted from [4]. Staining: myosin II in red, actin in cyan and tubulin in yellow. Scale bars: 2 mm in (a, b, h) and 200 nm in (c). (a) Mobile keratocyte fragment. (b-d) Platinum replicas of (a) revealed by electron microscopy. (e) Stationary keratocyte fragment. (f, g) Platinum replicas of (e) revealed by electron microscopy. (h) Actin, myosin and tubulin in several fragments. The time course on the right reveals a stationary fragment being pushed and becoming motile.

In Ref. [5], the authors treat epithelial cells with the small-molecule drug blebbistatin (BBS, $25\mu M$) to inhibit myosin II activity. The myosin II is believed to organize the actin in a ring-shaped region right inside the cell membrane, thus preventing actin from polarizing and forming the leading edge. The results shown in Fig. 1.10 support their argument. The cells treated with BBS can spontaneously break the symmetry of actin distribution and polarize. The cells then migrate in a roughly constant direction for hours. In contrast, the normal cells are stationary. The most intriguing finding of their work is that it reveals a

mechanism by which the cells can break the symmetry spontaneously. The treatment they used does not create artificial asymmetry because all of the symmetrically distributed myosin II molecules are evenly affected by the drug.

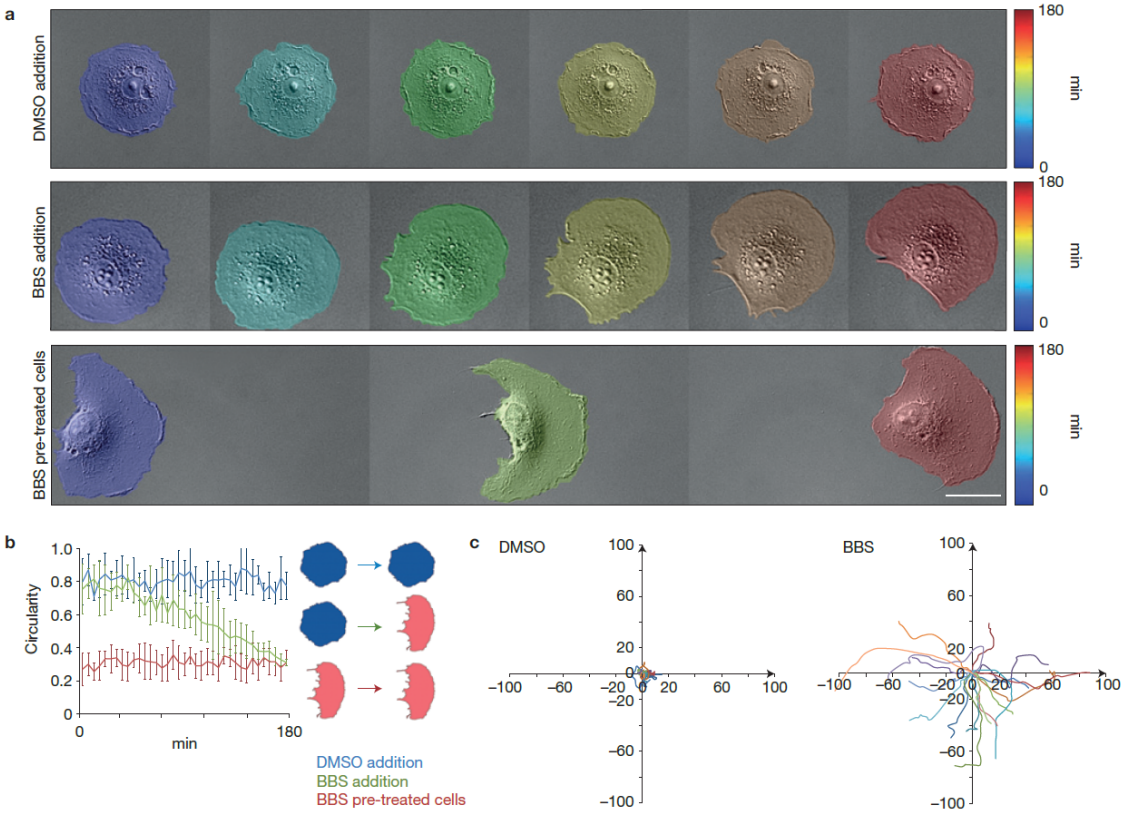

Figure 1.10: Adapted from [5]. **a**, movie frames during 180 *mins*, first row: control cell (DMSO addition); second row: cell treated with BBS (BBS addition); third row: cell after exposed to BBS (BBS pre-treated). Scale bar: $20\mu m$. **b**, time course of cell shape circularity index ($(4\pi\ area/perimeter^2)$). **c**, tracks of DMSO addition and BBS pre-treated cells over 180 *mins*.

In Ref. [6], the authors create tethers in HL-60 cells using heat shock. The cell polarizes with a protruding leading edge that links to the cell body through a very narrow neck, see Fig. 1.11. The result suggests that a long-ranged but fast transmitting inhibitor is required

for the polarization. The inhibitor needs to stop actin network assembly at the other end of the cell (trailing edge). The trailing edge connects to the leading edge via the narrow neck, in which chemical diffusion is dramatically slowed down. Thus any diffusion-reaction based inhibitor that needs to tunnel through the neck is not fast enough to prevent the trailing edge from assembling the actin network. However, the authors suggest that membrane tension is a good candidate for the inhibitor. The membrane tension meets the two requirements of the inhibitor, being long-range and fast transmitting. This is because the tension can travel from one end of the cell to the other almost instantaneously.

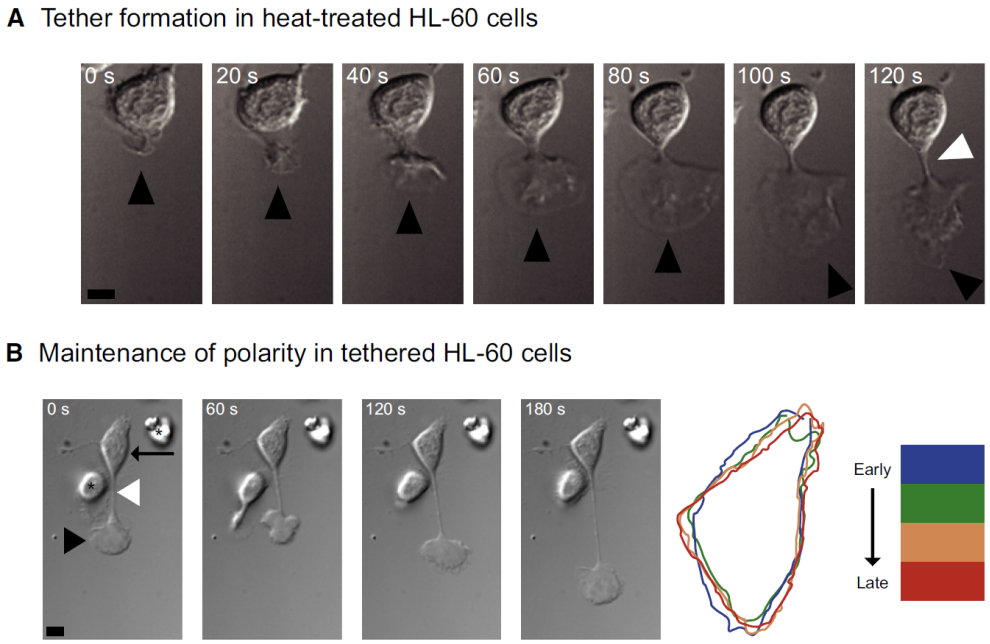

Figure 1.11: Adapted from [6]. **A**, Tether formation in HL-60 cells by heat treatment. Black arrowhead: pseudopod. White arrowhead: tether. Scale bar is $5\mu m$. **B**, Polarity maintenance in HL-60 cells after tether formation. Black arrow: cell body. Black arrowhead: pseudopod. White arrowhead: tether. Colored contours: outlines of the cell from early to late.

A long-range inhibitor is modeled in the simulations of Ref. [7]. The authors formulate

a local-excitation and global-inhibition (LEGI) response system that drives an excitable network. The LEGI system responds to uniform stimulus. Instead of being excited directly, the network is excited by the output of the LEGI system. The network is also a FitzHugh-Nagumo type network discussed in the "Biological Pulses" section. But, the network in [7] is modeled with two probability distribution functions (PDF) that have spatial gradients. When the network is excited by the LEGI system, it can break the symmetry of the cell and persistently polarize, see Fig. 1.12. The fascinating result shows that the LEGI system can excite the FitzHugh-Nagumo network utilizing its pulse nature, then create steady states that have non-zero spacial gradients. The LEGI driven FitzHugh-Nagumo network is thus transformed to a biological switch that can well describe cell polarization.

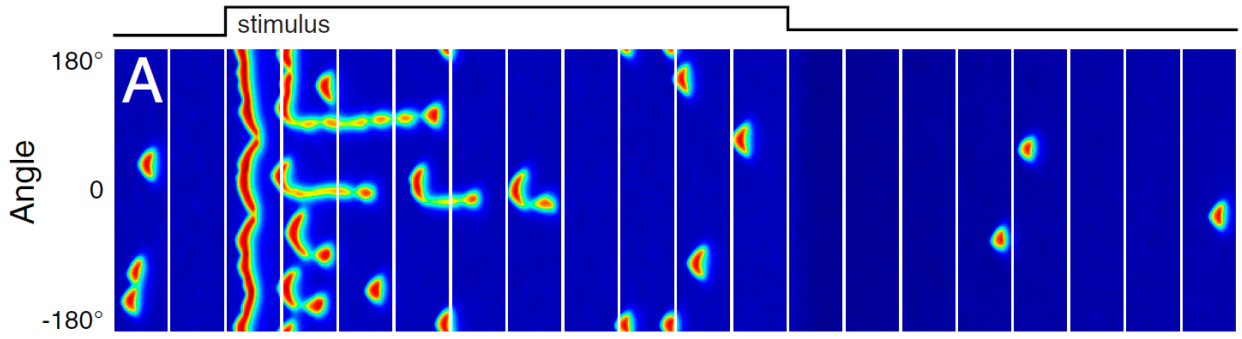

Figure 1.12: Adapted from [7]. Kymograph of the distribution of a global inhibitor from the model at all angles. Duration is $1200s$. At $120s$ a uniform stimulus was applied. At $720s$ the stimulus was removed.

These experimental studies provide great motivation for this thesis to understand the key network interactions driving SSB. Also, as suggested in [7] and [6], these interactions should contain a long-range and fast traveling inhibitor, most likely membrane tension.

In developing our understanding of such interaction networks, quantitative models are as supportive and important as experiments. First and foremost, quantitative modeling is an excellent tool for interpreting corresponding experimental data. In studying complex systems, all the experiments have limits on measuring the observables. The parts missing in the experiments can cause confusion and uncertainty. This problem is often well addressed by adding plausible assumptions in the model. If the result from the model agrees with the experiment, then a much better understanding of the topic is obtained than by working solely from the experimental data. Secondly, a quantitative model can predict new results that might be verified by experiments. Thus, modeling is a well established method to propose new experiments for studying important phenomena. In particular, there are several important competing models of cell polarization and migration that theory coupled with experiment, can help distinguish.

In Ref. [27], the authors model stochastic actin growth inside a rectangular shaped membrane. Their stochastic model predicts transient polarization of the actin network. Thus, the cell undergoes Brownian like motion. Their stochastic model is further understood by a deterministic master equation. When describing the two ends of the cell with two similar master equations, they find the approximate solutions being bistable if the network grows autocatalytically. The autocatalytic network is the key trait of branching, because the more mother filaments exist the more daughter branches will form. However, the model has a few issues needed to be solved. First, the motion of the cell predicted by the stochastic model is not persistent. Unlike the directional motions of the cells in [4] and [5], the modeled cell

moves like a Brownian particle that frequently changes directions. Second, the stochastic model does not include several important processes in actin network growth, such as capping and severing. These two processes might change their prediction based merely on branching and polymerization. Third, the actin polymerization in their model is not coupled to force, and thus misses an important negative feedback. The polymerization should be slowed down by the Brownian ratchet mechanism [21]. Thus, their conclusion could be affected by mechanical effects. Last, their analytical study of the stochastic model is approximate. There is no direct comparison between the analytical and stochastic models. Therefore, it is unclear why a bistable state gives Brownian motion instead of directional motion.

In Ref. [28], the authors propose a mechanical model with only a few degrees of freedom, that predicts cell shapes similar to those experimentally observed in [4]. Their model is bistable. There is a state with symmetric shape and another with polarized shape. The two states are separated by free energy barrier and are thus locally stable. The free energy is calculated based on actin polymerization, actin-myosin contraction in the lamellipodium and actin-myosin bundle contraction in the cell rear. The cell is thermodynamically relaxed on the free energy landscape. This model gives good predictions of the cell membrane, but still oversimplifies actin dynamics. The actin force is assumed as a constant. Therefore, there is no information of how actin dynamics can affect the cell shape. So it is still unclear what feedback mechanisms involving the actin network can lead to the cell polarization.

1.5 *Endocytosis*

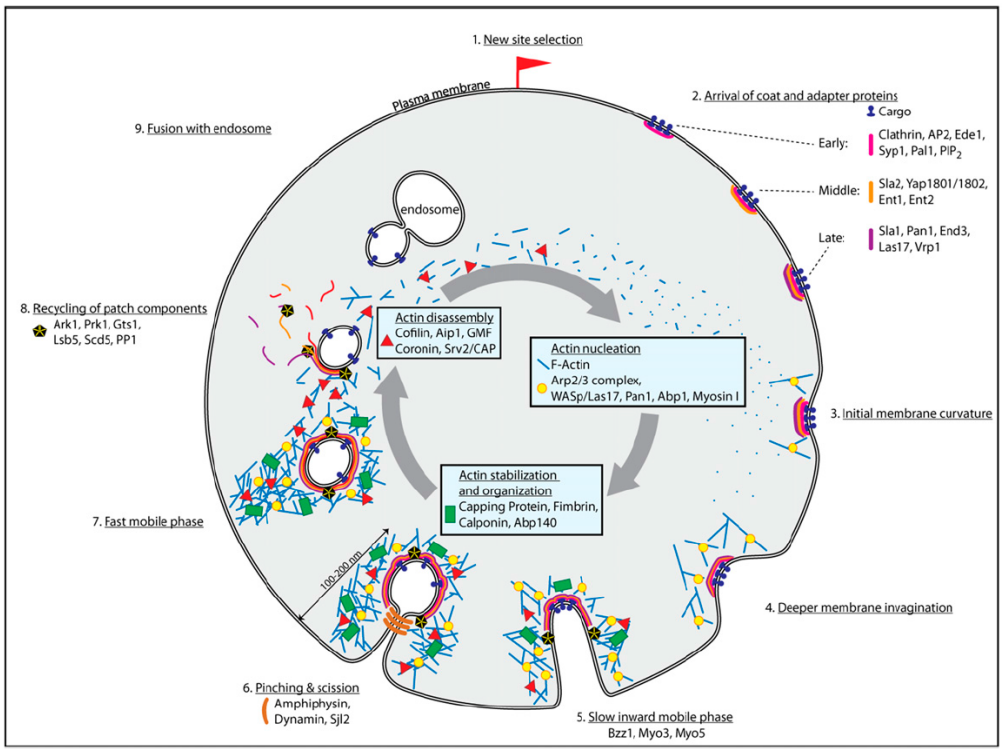

Figure 1.13: Adapted from [8]. Different stages of endocytosis and crucial proteins involved are illustrated.

A cell is enclosed in a cell membrane, consisting of a bilayer of lipid molecules. The membrane can open channels for small molecules to pass through. For transportating larger cargoes, and to recycle the membrane, the cell needs to proceed by endocytosis. In mammalian cells, endocytosis does not always require the actin network, but relies on dynamin for some of the mechanical force. On the contrast, in budding and fission yeast, the actin network is required. This is because yeast maintains a large turgor pressure that is opposed by a rigid cell wall over most of the membrane. Once the membrane is pulled off the cell wall, the

actin network and curvatyre-generating proteins must exert a large force to overcome the turgor pressure. Specifically, endocytosis in budding yeast is studied in this thesis, using both quantitative models and experimental data.

Fig. 1.13 gives a nice overview of endocytosis in budding yeast. Overall, there are over 60 kinds of proteins involved. The proteins arrive in a well arranged time sequence. In the early stage, the cargo arrives and various proteins assemble a coat inside the cell membrane. Coat proteins can recruit cargo or vice versa. Among these coat proteins, clathrin has a preferred curvature to force the membrane to bend, but the membrane is bent very little and moves inward only slightly in this stage (see Ref. [18]). Sla2 is an adapter protein for clathrin that co-works with Ent1. Sla2 and Ent1 also serve as an anchor that can bind actin filaments, so that the filaments can pull the coat and membrane inward. In the middle stage, the actin network assembles. Las17 is the yeast homolog of WASP, which can activate Arp2/3 complex to assemble the actin network. The barbed ends of the filaments in the network usually point toward the outside of the cell (see Fig. 1.14). Thus the filaments can push the membrane and pull the cargo inward while polymerizing. Upon actin network formation, the membrane is bent. In the network, capping proteins bind to the barbed ends of the filaments to prevent the filaments from getting too long. Usually the filaments at the endocytic site are about 20-30 subunits long. Physically, longer filaments are more likely to buckle or break into pieces, thus failing to exert force. In the late stage, cofilin appears, which severs actin filaments and thus disassembles the network. The cargo is inside the cell within a vesicle, which is transported into the cytosol. The vesicle is pinched off the membrane and released

via late BAR-domain proteins, like Rvs161/167. The BAR-domain proteins have preferred curvature to bend the membrane.

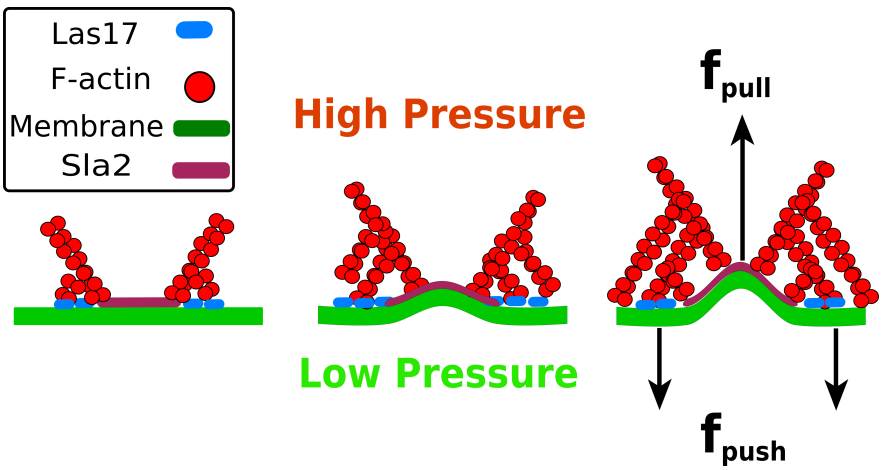

Figure 1.14: Adapted from [2]. Schematic of actin exerting forces on Sla2 cap and membrane to overcome turgor pressure.

Fig. 1.14 shows the mechanical properties of endocytosis. At the endocytic site, the actin network is "glued" to the Sla2 cap, and polymerizes and branches (the two processes are referred as growth) at the bottom close to the membrane. The growing network thus can push a ring-shaped region of the membrane down while pulling the Sla2 cap up. The pushing force and the pulling force are approximately equal despite random forces caused by thermal fluctuations. The Sla2 cap leads an invagination into the cell. The invagination embraces the cargo right under the Sla2 cap. To create such an invagination, the actin network needs to overcome a large opposing force and a smaller opposing force. The large force is caused by the difference in osmotic pressure from inside and outside of the cell, known as the turgor pressure. The turgor pressure can be as large as $\approx 10^6 Pa$ (see [2]),

and normally hard to measure. Therefore the corresponding force is considered within a large range from $100pN \rightarrow 1200pN$ [2]. The smaller opposing force is caused by bending the cell membrane, which is normally an order of magnitude smaller than the larger force. Because endocytosis fails when actin growth is inhibited in yeast cells [29, 30], actin force probably counts at least for 50% of the total external force. Curvature generating proteins, like clathrin, are not capable of generating enough force to overcome the external forces, see Ref. [31].

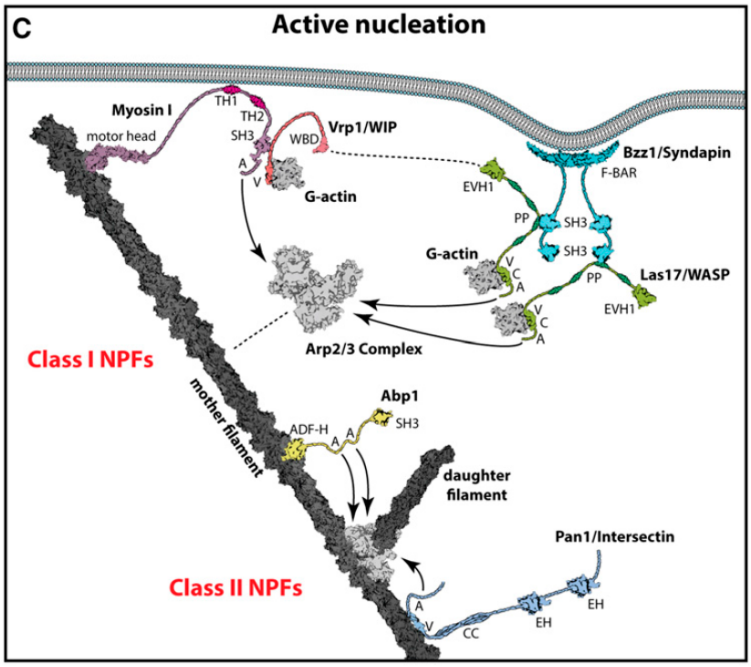

Figure 1.15: Adapted from [8]. Interaction of actin with Arp2/3 complex and actin regulators (also known as nucleation promoting factors (NPFs)). Class I NPFs activate Arp2/3 complexes and bind to free actin monomers (G-actin). Class II NPFs activate Arp2/3 complexes and bind to filamentous actin (F-actin). Normally, Class I NPFs are more efficient than class II NPFs to activate new branch formation.

A feature of the actin network that can grow against the forces from turgor pressure and

membrane bending is that it is in a dendritic form. As discussed in Section 1.1, the dendritic actin network requires activated Arp2/3 complex molecules to bind existing mother filaments and create bases for daughter filaments. The activation process of the Arp2/3 complex is greatly accelerated by Las17 (yeast WASP), see *in vitro* data of actin growth in [14]. The activation process is triggered when Las17 is dimerized by Bzz1, see Fig. 1.15. The activated Las17 then binds a Arp2/3 complex via its "*acidic*" domain, the "A" domain in Fig. 1.15. The Las17 also binds to an actin monomer via its "V" domain. The monomer is to become the first subunit of the daughter filament. When the Arp2/3 and the monomer are bound together on a mother filament, the Las17 molecule will leave the two molecules. Then the daughter filament can start to polymerize at the first subunit. Therefore, Las17, especially its "A" domain, is important in dendritic network formation.

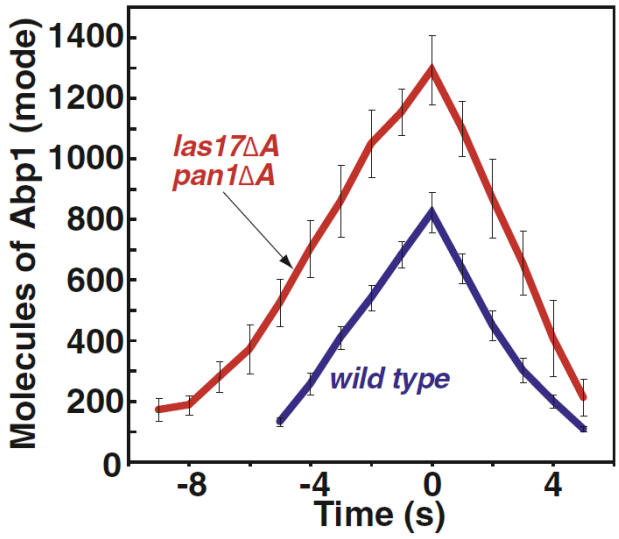

Figure 1.16: Adapted from [9]. Time course of Abp1 during budding yeast endocytosis. Wild-type in blue and *las17*Δ*acidic pan1*Δ*acidic* mutant in red. ΔA means Δ*acidic*. The mutant has **more** Abp1.

Now the question is how many actin filaments and actin subunit are present at each endocytic site? The question is challenging but well addressed in Refs. [9, 10]. Ref. [9] is the first paper that measures molecule numbers of several important proteins during endocytosis in budding yeast. The authors use Green Fluorescent Protein (GFP) to label the proteins in interest, such as Abp1 and Las17. They compare the intensity of the endocytic proteins with the intensity of Cse4, which is a protein in the kinetochore. Cse4 has a relatively fixed number of about 109 in each cell during the anaphase of mitosis. Thus, the comparison of any measured protein intensity with Cse4 intensity can give the number of the measured protein. See Fig. 1.16, for example, shows the time courses of Abp1 in measured for wild-type and mutant cells. Abp1 is a good proxy for F-actin because Abp1 labeling does not cause serious disfunctions, while actin labeling does. The GFP labeled protein is seen as a protein patch using a wide-field microscope, which is a Conventional Microscopy (CM) method. The patch looks like a blurred circle. The detailed structure of the endocytic site is not observable using CM due to the diffraction limit (the minimal distinguishable distance) of the microscope, $d = \frac{\lambda}{2n \sin\theta}$, where λ is the wavelength of the observed florescence light, and $n \sin\theta \equiv NA$ is the numerical aperture of the microscope. For GFP excited by a $488nm$-wavelength laser in [10], the emission green light peaks at $\lambda = 509nm$ [32]. For the microscope used in [10], $NA = 1.45$. Thus $d \approx 175nm$, which is on par of the whole endocytic site ($\approx 150nm$). The detail of the network is then lost in the blurred patch.

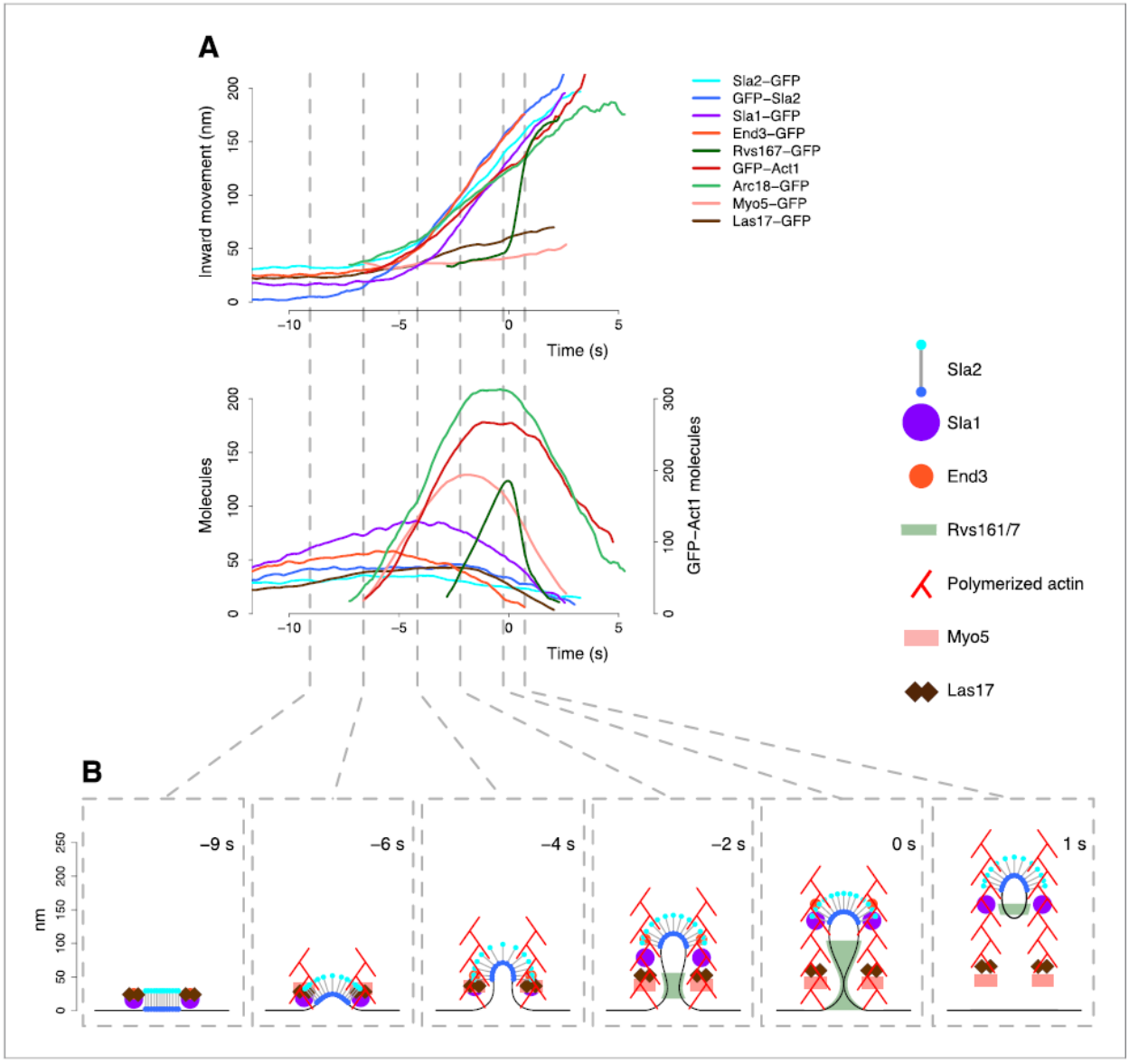

Figure 1.17: Adapted from [10]. Time courses during budding yeast endocytosis. **A**, time courses of the inward motion and the molecule numbers of the GFP labeled proteins. **B**, spatial localization of the proteins at several time points marked by dashed lines from the time courses.

This diffraction limit could be overcome by the technology of the Super Resolution Microscopy (SRM). But SRM usually requires super intense exciting laser power, 1-2 orders

of magnitude higher than CM needs. The intense laser is photo-toxic to the cell and thus interferes with endocytosis. Also, SRM is poor at temporal resolution, which is is required by the rapid time scale of endocytosis. Ref. [10] presented SRM data for the endocytic protein Sla1 in fixed yeast cells. Some SRM data of live mammalian cells are also emerging, see [33]. Besides SRM, Electron Microscopy (EM) can reveal endocytosis at much smaller scales [11, 12, 34]. However, EM can only provide images of fixed samples and has many potential artifacts. Thus, the wide-field microscope is still a powerful tool to evaluate the time evolution of endocytosis. In addition, although CM can not distinguish the detailed structure of the actin network in endocytosis, it can still show the average position of the network accurately. This is because the network, seen as a blurred patch, is well approximated by a two dimensional Gaussian intensity function. The center of the Gaussian function is thus the average position of the network.

In Ref. [10], the trajectories and intensities of the patches are measured. The resulting time courses and trajectories are aligned so that a weighted difference in space and time is minimized, through spatial rotation, spatial translation and temporal translation. The intensities are also calibrated to absolute numbers of protein again by comparing the observed proteins with a kinetochore protein Nuf2. Lastly, the temporal differences among the GFP labeled proteins are obtained by comparing them with Abp1-mCherry. mCherry is an alternative to GFP. The Abp1-mCherry is different in color compared to the GFP labeled proteins. Measuring one GFP labeled protein and Abp1-mCherry gives the relative timing of the two. Then another GFP labeled protein is measured in the same way. The final result

is shown in Fig. 1.17. All the observed proteins behave like "pulses". Tracking patches for CM is still challenging due to the large amount of data and the noise from background fluorescence.

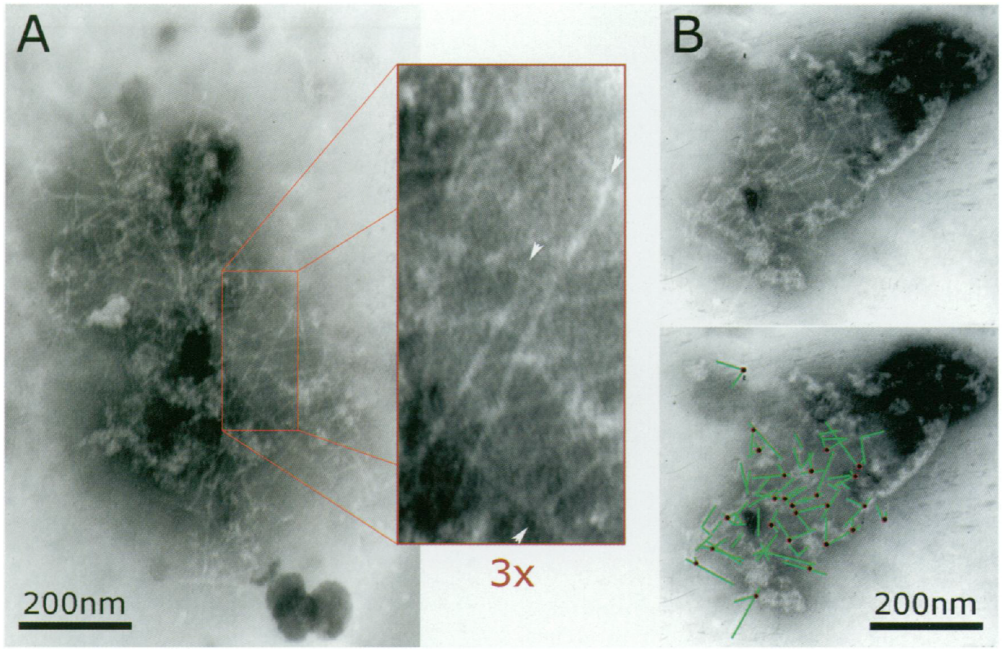

Figure 1.18: Adapted from [11]. **A**, Patch of branched actin network. Arrowheads: actin branches. **B**, quantitative representation of actin filaments, shown by green lines and red dots.

As just mentioned, EM reveals some structures of endocytosis that are to small to observe using wide-field microscope [11, 12], see Fig. 1.18 and 1.19. In Ref. [11], the authors remove endocytic protein patches from cells and scan the patches using EM. They find dendritic actin network at the sites. In the second paper, the authors use also EM to reveal the invagination in different stages, from shallow dimples (early) to long tubes (late). The authors also label several important proteins in endocytosis with gold, and show the positions of the proteins relative to the invagination. In both papers, although the samples scanned by EM are fixed,

some important information about the actin network is obtained, such as the actin network structure and endocytic protein distributions.

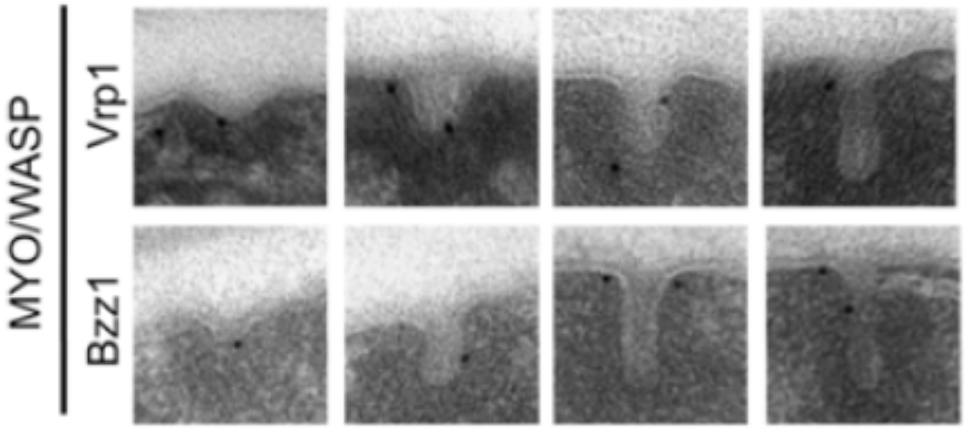

Figure 1.19: Adapted from [12]. Immuno-EM micrographs of cell membrane in endocytosis. Black dots show the stained proteins Vrp1 and Bzz1, in the two rows respectively. The four columns from left to right represent shallow, short intermediate and long invaginations.

Similar results of GFP labeled proteins in fission yeast endocytosis are obtained in [13], see the time courses in Fig. 1.20. Here absolute protein counts were obtained using a whole-cell calibration curve. In fission yeast, fewer similar proteins share equivalent functions, in comparison with budding yeast. For example, fission yeast has only one type I myosin, Myo1. Budding yeast, however, has two, Myo3 and Myo5. Thus in some ways it is more convenient to study fission yeast having various mutations. The mutations in budding yeast often have replacement effects that can interfere with the mutations. The proteins similar to the mutated proteins can replace their functions. In Fig. 1.20, the fission yeast proteins are also like "pulses". From Refs. [9, 10] and [13], it is seen that endocytic proteins in both budding and fission yeasts also behave like "pulses". However, this conclusion holds only

for wildtype cells and some mutants. Other mutated cells, or drug treated cells, can behave differently.

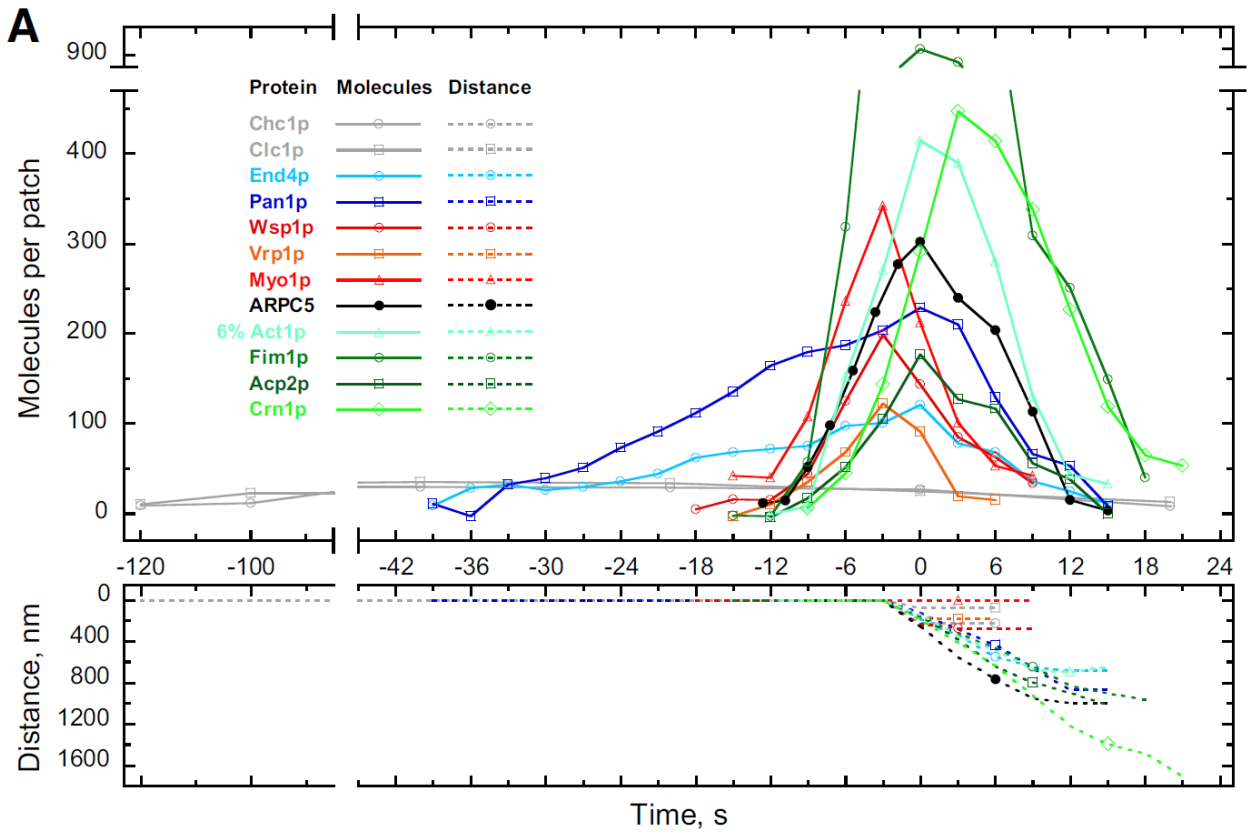

Figure 1.20: Adapted from [13]. Time courses during fission yeast endocytosis. On top, time courses of molecule numbers of endocytic proteins labeled with fluorescence proteins. At bottom, the corresponding motion from the membrane of the endocytic proteins.

Some mutations change the peak height and/or duration of the pulses of the proteins. Sometimes the phenotypes of these mutations are counter-intuitive and thus crucial for understanding endocytosis. For example, in [9], the authors delete the *acidic* domain of Las17 and Pan1 (another adapter protein), creating *las17*Δ*acidic pan1*Δ*acidic* mutants. The mutation leads to a higher peak height of Abp1. This means that the F-actin in this mutant

cell is higher than in the wildtype cell. This is a typical counter-intuitive phenotype: mutating the actin network regulator causes even **more** F-actin assembled. The counter-intuitive phenotypes indicate that the endocytosis is not a simple linear system, but rather a complex non-linear system that contains crucial feedback mechanisms. One goal of this thesis is to understand the counter-intuitive phenotype, *las17*Δ*acidic pan1*Δ*acidic*, which is remeasured, confirmed, and quantitatively studied in Chapter 3.

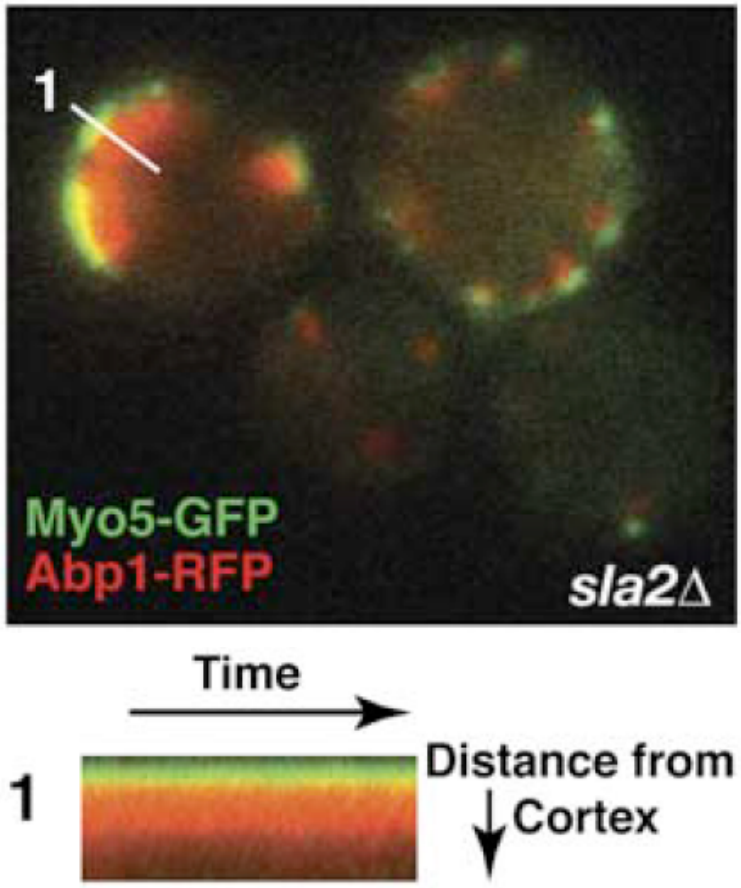

Figure 1.21: Adapted from [14]. One movie frame of Myo5 and Abp1 in *sla2*Δ mutant cells during budding yeast endocytosis. "1" marks the point of kymograph at the bottom.

Other interventions completely change the "pulse" like patches to permanent patches.

For example, in [14], the authors delete the entire protein Sla2, *sla2*Δ. The result, Fig. 1.21, shows that endocytic patches of Myo5 and Abp1 become permanent. Comparing the phenotype to the wildtype data, Fig. 1.17, it is clear that a behavioral transition of the patches from transient to static can happen when certain proteins are missing.

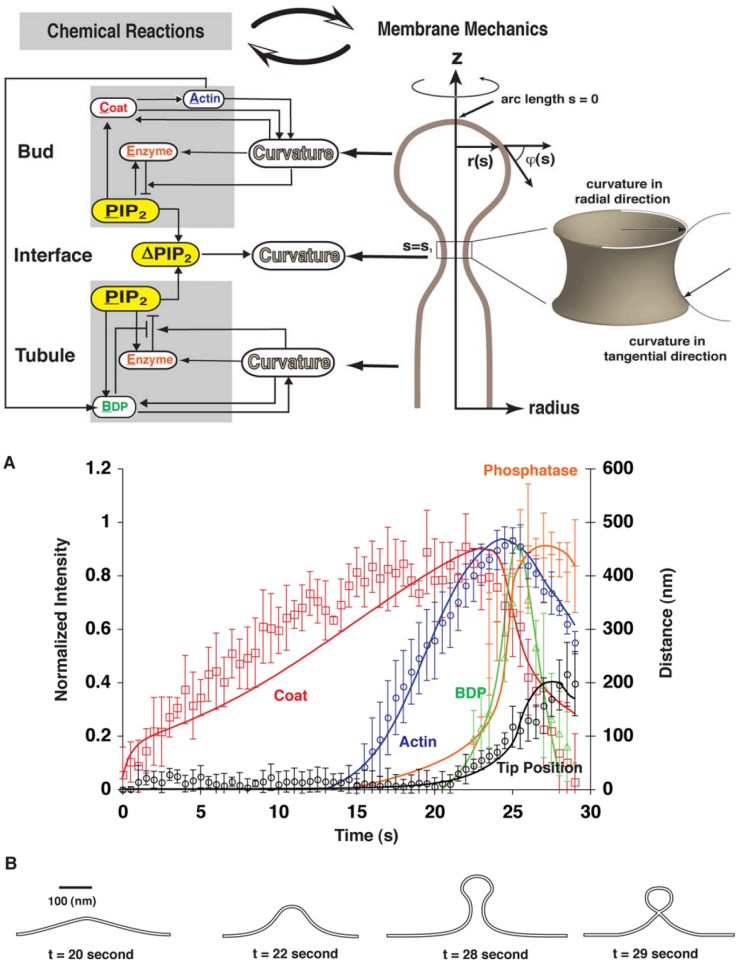

Figure 1.22: Adapted from [15]. Feedback interaction among actin, coat protein, enzyme, PIP_2, BDP and membrane curvature. **A**, comparison of the model with experimental data on a time course of normalized intensity and distance from membrane. **B**, calculated membrane shape from the model.

The experimental data have been interpreted by previous quantitative models. In [15],

the authors propose a model based on feedback interactions among endocytic proteins and membrane curvature. The feedback mechanisms and time courses are shown in Fig. 1.22. The authors suggest that actin network generates curvature by pulling the "bud", namely the top region of the invagination. The curvature determines the assembly rate of an enzyme that can hydrolyze PIP_2. PIP_2 is required for coat protein accumulation. There are at least two important functions of the coat proteins in endocytosis. The first is that they are required for F-actin assembly. The second is that they can bind actin filaments to facilitate the pulling force. Thus the coat proteins promote actin growth and force generation. A similar feedback interaction mechanism is in the tubule region, where curvature can recruit bar domain proteins, which can protect the PIP_2 from being hydrolyzed on the tubule. The PIP_2 rich tubule also stabilizes the bar domain proteins.

The model matches the experiment well for normalized intensity of the various proteins. However, there is no comparison with the experiment on protein numbers. The model might not predict the correct behavior when fitted to the protein numbers measured in experiments. Besides, the authors treat all the coat proteins as only one kind. But there are at least two kinds, one on top of the invagination, the other in a ring region surrounding the invagination, see Ref. [10]. The ring proteins do not travel with the top of the invagination as suggested by the authors. One likely ring is Las17, which promotes actin network growth. Therefore, it is still unclear how and where the coat proteins activate actin growth, and whether the process is affected by membrane curvature or not.

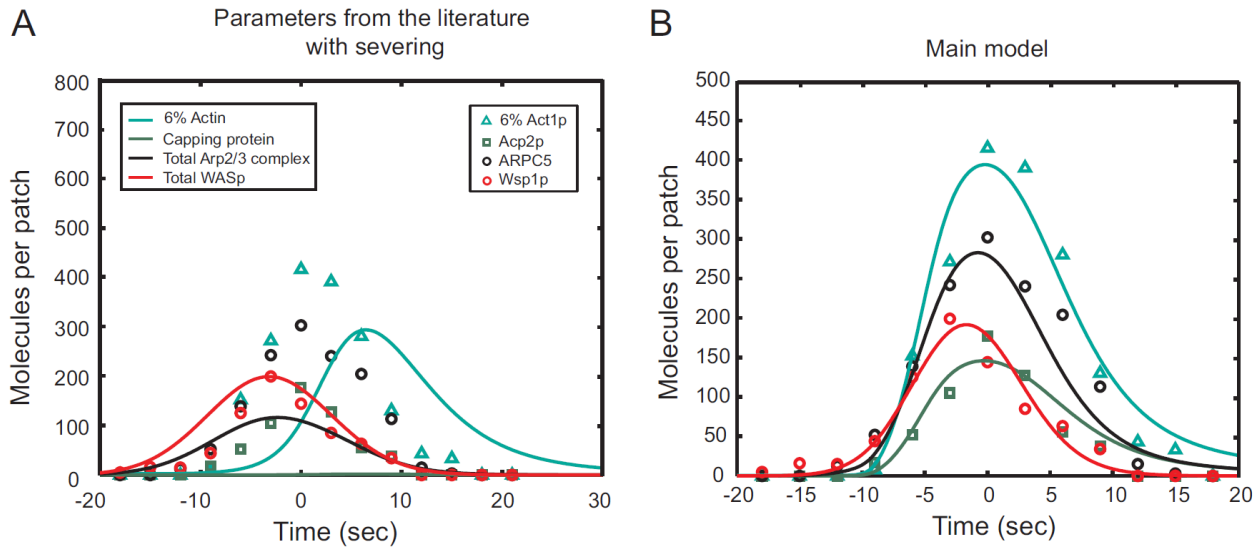

Figure 1.23: Adapted from [16]. **A**, model compared with experiment without parameter optimization. **B**, model compared with experiment after parameter optimization.

In Ref. [16], the authors develop a model that can match the protein numbers in the associated experiments [13]. The model predicts the correct pulse behavior when the parameters are optimized, see Fig. 1.23. However, the model relies on a presumed Gaussian pulse of WASP. The origin of this Gaussian pulse is unclear. Thus the mechanism that diminishes the WASP at the end of the endocytic process is missing in the model.

1.6 Scope of Thesis

In this thesis, the dendritic actin network is studied using quantitative models and fluorescence imaging data. The models include the processes of actin network formation and the mechanochemical interactions between the network and the membrane. The stochastic, theoretical and experimental results are matched. These three aspects render the models novel. The questions remaining from previous models are thus clarified to some extent by

this thesis. A fully automatic tracking method is also developed to conquer the challenge of processing massive data. Lastly, the computation in this thesis is greatly accelerated using CUDA, a computer language for GPU computation.

In Chapter 2, a cell consisting of actin filaments and subunits, modulated by membrane tension, is modeled. The model has a stochastic and a deterministic version, which agree well. The model predicts a phase transition from unpolarized to polarized cells. When polarized, a cell moves in the same direction persistently. The stochastic version gives a two dimensional view of the cell, vividly revealing that the mechanisms in the model can reproduce cell polarization. The deterministic version gives an intact mathematical description of the polarization process by including all the assumptions and interactions among the variables. An instability of the unpolarized state is found mathematically, which clarifies the cause of the cell polarization. The transition from the unpolarized to the polarized state happens when the cell can produce enough membrane tension. When the cell is in the polarized state, it can move persistently either to the left or right, which makes it a biological motion switch. The key merit of this model is that the cell polarization phenomenon seen in the vivid picture from the stochastic simulation is clearly explained by the deterministic calculation.

In Chapter 3, a stochastic model and a simplified deterministic model of endocytosis in budding yeast are proposed. The models give time courses of crucial endocytic proteins, F-actin and Las17, that match experimental results well. Besides, the model predictions of several mutant and drug treatment phenotypes, especially the counter-intuitive phenotype

described in the previous section, are verified by experiments. The stochastic model provides a three dimensional actin network pulling the cell membrane while resisting the turgor pressure. The time courses of Las17 and F-actin are pulses that emerge one after the other. The deterministic model gives a similar result. Although the deterministic model does not quantitatively match the stochastic model, it provides the latter with reasonable parameter values to start fitting to the experiments. More importantly, the core feedback interactions in the deterministic model are the same as those in the stochastic model. So, the qualitative conclusions from the two models are the same. It is found that a negative feedback interaction from F-actin on Las17, and an autocatalytic positive feedback from Las17 on F-actin, and an autocatalytic positive feedback of Las17 on itself, are needed to reproduce the correct biological pulses in endocytosis.

The deterministic models in Chaper 2 and 3 are all based on ordinary differential equations (ODE). However, it is often challenging to describe the actin network using ODEs. This is because the branching process in the actin network can only happen in a narrow region close to the membrane. This region is known as the branching layer, see [22]. Besides, the force generated by the actin polymerization to push the membrane is also near the contacting surface between the network and the membrane, defined here as the force layer. Therefore, the bulk portion of the network neither branches new filament nor exerts force. To distinguish the branching layer and force layer from the rest of the network, a new model based on partial differential equations (PDE) is developed in Chapter 4. The PDE model incorporates the geometry of the network. Therefore, it provides much more infor-

mation than the ODE. When it includes the same feedback interactions as the ODE model from Chapter 3, the PDE model can also match the experimental data and the stochastic model in Chapter 3 well. More surprisingly, both cell polarization and the endocytosis can be well described by the same PDE model. There might thus be a unified theory for both phenomena.

In sum, this thesis sheds some light on the biological physics of cell migration and endocytosis by studying actin dynamics, using a novel combination of approaches.

Chapter 2

FEEDBACK MECHANISMS IN A MECHANICAL MODEL OF CELL POLARIZATION

2.1 Introduction

Many important functions of cells and microorganisms rely on directed migration based on polarization, including cancer metastasis and neutrophil tracking of bacteria. Polarization arises from an asymmetric actin distribution where a denser actin network grows at one side (leading edge) and a sparser network at the other side (trailing edge) of the cell [35]. Cells can polarize either spontaneously [4] or in response to extracellular signals such as chemoattractants [6, 7] and mechanical force [4]. After the stimulus is removed, cells sometimes maintain their polarity and keep migrating [4]. Thus under some conditions, the polarized state of a state is stable, while the unpolarized state is unstable or metastable. The connection between polarization and the direction of cell migration has recently been emphasized by experiments in which cells were polarized by micropatterns and subsequently allowed to migrate [36].

Several recent reviews [37, 38, 35, 39, 40, 41, 42] have treated the mathematical modeling of cell polarization. At this point the relative contributions of different interactions, and the conditions which favor the polarized state, are still not known in detail. Both chemical interactions and mechanical interactions play a role. Most models of cell polarization

have employed the general framework of the local excitation and global inhibition (LEGI) mechanism [43], based on a slowly diffusing (local) activator and a fast diffusing (global) inhibitor. Several treatments have identified the activator with signalling proteins such as Rac and phosphatidylinositol (3,4,5)-trisphosphate (PIP3) [6, 44], and the inhibitor with phosphatase and tensin homolog (PTEN). Recent measurements [6] have clarified the role of mechanical interactions in driving cell polarization. It was shown that the inhibitory interactions propagate too quickly for diffusing signal proteins to play the role of the global inhibitor. Mechanical tension, which propagates almost instantaneously, was suggested as a candidate for the fast inhibitor. This is consistent with previous work in which polarization was induced by the application of mechanical force [4]. However, it is not known precisely how tension aids the symmetry breaking, nor how it interacts with the chemistry of actin polymerization.

Several theoretical treatments have aimed to clarify the role of mechanical force and actin polymerization in polarization, some of which are reviewed in Ref. [41]. Ref. [45] treated a simple model of "inside-out" polarization, in which actin filaments fixed at their nongrowing ends pushed on a bead from different sides. They found that this model led to directed motion of the bead via a force-dependent symmetry-breaking mechanism. However, it is not clear over what range of parameters symmetry breaking would occur, nor to what extent the same mechanism would operate in cells. Ref. [27] treated a model of autocatalytic actin network growth based on filament branching caused by Arp2/3 complex, in a simple cell geometry. The force was transmitted via flexible springs between the ends of the cell,

which were treated as flexible polymers. Autocatalytic actin polymerization was found to provide a positive-feedback mechanism that temporarily polarized the cell. However, at large time scales, the model obtained Brownian motion rather than stable directed motion. In addition, transitions between polarized and unpolarized states with varying parameters were not explored. Finally, because the polarization relied on autocatalytic actin filament nucleation, it was not clear to what extent mechanical effects were important for polarization.

A simplified mechanical model of cell fragments treated the interplay between pushing force exerted by actin polymerization on the cell edges, contractile force powered by myosin II across the cell, and elastic tension in the cell membrane [28]. Forces from actin and myosin were treated as assumed force densities. In the energy as a function of deformation, two stable energy minima were found, one polarized and unpolarized. In this model, application of a force, as in Ref. [4], could induce a transition to a polarized state. Ref. [46] treated the interplay between membrane tension, filament force generation at the front of a cell, and filament breaking at the rear. Again using a distributed force density, they calculated a self-consistent polarized profile of polymerized actin. They found a correlation between front-to-rear distance of the cell and curvature of the leading edge, consistent with experiment.

The work of [47] treated a membrane that was deformed by actin polymerization and actomyosin contraction. The front and back of the cell were coupled by the elasticity of the membrane. The distributions of actin and myosin were treated as continuous variables in two dimensions. After perturbation of an initially circular cell by a pulse of F-actin at the front, the asymmetry in the actin distribution persisted, and the cell deformed, becoming

longer in the direction transverse to its motion. Myosin moved to the rear of the cell. The authors calculated a phase diagram giving cell shape as a function of cell-substrate adhesion strength and myosin activity. They found that cell asymmetry was most favored at a point where myosin activity and cell-substrate adhesion are intermediate.

In the models of Refs. [28], [46], and [47], the key mechanical interactions and their effect on actin polymerization are given explicitly. However, the treatment of actin polymerization in these models is simplified. Here we aim to grasp the key mechanical interactions in a more complete, stochastic model of actin polymerization. In order to focus on the mechanical interactions, we treat a model including only actin polymerization and mechanical force, and do not treat the upstream signaling pathways. The model treats actin networks present at the two sides of an idealized square cell fragment. The two sides serve as identical obstacles to actin polymerization, which slow the polymerization according to the the Brownian Ratchet mechanism [21]. The model is solved using both a stochastic simulation approach, and a rate equation approach that is systematically derived from the stochastic approach. The results of the two approaches agree closely, for both steady-state and dynamic properties of the system. Both treatments predict symmetry breaking over a broad range of parameter values. The origins of the symmetry breaking are explored by a linear stability analysis of the rate equations. We find that the symmetry breaking is caused by a feedback loop connecting fluctuations in the number of filaments on the two sides of the cell with fluctuations in the amount of polymerized actin. Increasing polymerized actin on one side favors growth of the number of filaments on that side, while the increased number

of filaments can favor or inhibit actin polymerization depending on the parameter values. A key factor in obtaining accurate estimates of polarization in the rate-equation approach is the use of a state-dependent filament decay rate.

The development of an accurate rate-equation approach for treating actin polymerization and depolymerization will have applications beyond the specific problem of cell polarization treated here. Simulations of whole-cell structure and function usually require simplifying approximations such as the description of actin and related proteins by continuous densities. A major difficulty in such calculations has been knowing how to treat actin network disassembly correctly, and the state-dependent decay rate developed here is a step in this direction.

This chapter is based on an article published as Xinxin Wang and Anders E Carlsson, "Feedback mechanisms in a mechanical model of cell polarization", *Physical Biology*, 11(6): 066002, 2014.

2.2 Model

2.2.1 Stochastic Model

We treat a $2\mu m \times 2\mu m$ square cell fragment with height $0.2\mu m$, containing actin filaments. The lateral size is taken to correspond to a small cell fragment, while the height is chosen to correspond to a typical lamellipodium thickness. Changing the system size leads to changes in parameter values, but not in the qualitative behavior seen below. For example, doubling the length of the cell changes the critical values of the parameters required for polarization by about 50%. The model treats free actin (G-actin) and polymerized actin filaments (F-actin).

The actin filaments are located at either end of the cell. The G-actin monomers diffuse freely in the cytoplasm of the cell, and are converted to F-actin by polymerization or nucleation events. Conversely, F-actin subunits convert to G-actin through depolymerization from filaments. Each individual filament has two chemically distinct ends, a "barbed" end where polymerization is favored, and a "pointed" end where depolymerization is favored. Force on the barbed ends slows actin polymerization according to the Brownian Ratchet mechanism [21]. In order to focus on the effects of mechanical interactions on cell polarization, we treat only the most basic unit processes: nucleation and growth of actin filaments. This model is similar to that of Ref. [27], but differs in that autocatalytic branching is not included, and that we treat a rigid membrane at each side of the cell. In both approaches to solving the model, the following assumptions are made:

1. Filaments nucleate only right at the front and back of the cell, as indicated in blue in Fig. 2.1. This assumption is based on the fact that actin filament nucleation requires Arp2/3 complex, which is activated by agents in the membrane [48]. The nucleated filament network is taken to be two dimensional because of the limited height of the simulation cell. Thus the height controls only the actin monomer supply and the rate of filament nucleation at the cell edges.

2. Arp2/3 complex is present in excess, so that we can ignore the effect of filament nucleation on the cytosolic Arp2/3 concentration. Thus chemical feedbacks involving the Arp2/3 concentration are ignored.

3. G-actin diffusion is infinitely fast. In the present model, actin assembly and disas-

sembly occur at the same side of the cell, rather than assembly at one end and disassembly at the other end. Therefore, there is no net transport of monomers from one side of the cell to the other. Previous analysis [49] has shown that diffusion of G-actin in this case is not a significant constraint. The rate-limiting G-actin diffusion process is from the front to the rear of the actin network at either side of the cell. Typical diffusion coefficients of actin monomers *in vivo* are $\sim 5 \times 10^{-8} cm^2/s$ [50], which implies that the time scale for this process is on the order of a second, much smaller than the calculated time scale of polarization. Thus the steady state of the model is not affected strongly this assumption. However, diffusion rate limitations could affect the dynamics of polarization more strongly.

4. The actin filament barbed ends point out of the cell fragment, as found in many studies including Ref. [51]. Each filament has an angle $\alpha = \pm 35^\circ$ with respect to the forward direction [51, 52]. In Fig. 2.1, the red filaments are growing and generating force against the membrane.

5. There is no pointed-end growth.

6. Filament capping and branching are ignored, in order to limit the number of variables. However, as discussed below, our model may in some ways mimic the nucleation-growth-capping-depolymerization cycle believed to control actin dynamics cells.

7. The actin filaments are rigid and tightly attached to an underlying substrate. The most pronounced departures from this scenario would result from retrograde flow at the leading edge, in which polymerized actin slides over the substrate. The extent of retrograde flow varies between cell types, and our results will be most relevant to those where retrograde

flow is slow.

8. The positions X_1 and X_2 of the membrane at the two sides of the cell are determined by the average of the barbed-end coordinates $x_{1,i}$ and $x_{2,j}$: $X_1 = \frac{1}{N_1}\sum_{i=1}^{N_1} x_{1,i}$, with a similar result for side 2, where where N_1 and N_2 are the numbers of filaments at the two sides.

9. Actin polymerization stretches the top and side membranes of the cell elastically, with a spring constant K, as indicated by the purple springs in Fig. 2.1. The interaction force between the membrane and the actin filament network at is equal to the tension

$$T = K\,(L - L_0) \equiv K\Delta L, \tag{2.1}$$

where L_0 is the original length of the cell and

$$L = X_1 - X_2 \tag{2.2}$$

is the length after being stretched by the filaments. We do not include the effect of volume changes during the simulation on the actin concentration. Our additional tests showed that including this effect changed the critical parameter values for polarization by less than 5%.

The stochastic approach is implemented via Monte-Carlo simulation of the polymerization, depolymerization and nucleation processes. We use a time-driven evolution algoreithm with a constant time step Δt, rather the event-driven Gillespie algorithm [53], because this simplifies the updating of the continuous variable T. During each time step, uniformly distributed random numbers ξ between 0 and 1 are generated for each process.

a) A free actin will polymerize onto a barbed end if ξ is less than $k_i^+ \Delta t$, where

$$k_i^+ = k_{on} G \exp\left(-\beta \frac{T\delta}{N_i}\right), \tag{2.3}$$

is the polymerization rate, k_{on} is the on-rate constant, δ is the filament length increment per added actin subunit, and β is the inverse temperature. The exponential behavior comes from the analysis of Ref. [21]. This process is repeated for each filament. When polymerization occurs, G is reduced appropriately.

b) Barbed-end depolymerization will occur if ξ is less than $k_B^- \Delta t$, where k_B^- is the barbed-end depolymerization rate. A subunit from the a barbed end is removed and G is increased. Pointed end depolymerization is treated similarly. When the last subunit of a filament depolymerizes, the filament is removed from the simulation.

c) Filament nucleation occurs if ξ is less than $k_n \Delta t$, where k_n is the random nucleation rate. A number l_0 of G-actins are removed from solution to form a new filament of length l_0.

The nucleation rate k_n is taken proportional to G^2 as suggested by Ref. [54]:

$$k_n = \frac{1}{2} k_r G^2 \frac{A}{A_0}, \tag{2.4}$$

where k_r is a constant, A is the frontal area of the leading edge, and $A_0 = 0.4\mu m^2$ is the reference value of the area. The area scaling is based on the assumption that actin nucleators are uniformly distributed across the front edge of the cell. During the course of a given simulation, the frontal area is kept fixed. The above scaling was used to compare

simulations for cells with different volumes. The new filaments are placed at the average barbed-end locations X_1 and X_2 with equal probability, and distributed uniformly parallel to the leading and trailing edges of the cell.

In reality, some filaments will push farther into the membrane than others, and one might expect some filaments to be left behind the moving membrane. However, these differences are reduced by membrane flexibility. Our previous studies of filament-membrane interactions (Ref. [55]) showed that filaments can grow while attached to the membrane. Trailing filaments being pulled by the membrane grow faster, and the ones that penetrate into the membrane grow slower, tending to equalize the positions of the filaments. We account approximately for flexibility by assuming that the filaments realign after each time step so that their barbed ends are at the same location as the membrane, placing them at X_1 and X_2 (see Fig. 2.1).

We have also considered an alternative model with explicitly flexible front and back membranes. Each filament has an individual harmonic force acting on its barbed end, which is evaluated from its extension beyond the original position of the unextended membrane. This does not cause any qualitative changes in the results. The same type of bifurcation is found in this case, and the effects of the bifurcation parameters described have the same sign. However, it is hard to compare these two treatments quantitatively since the membrane spring constant K must be very different in the two cases.

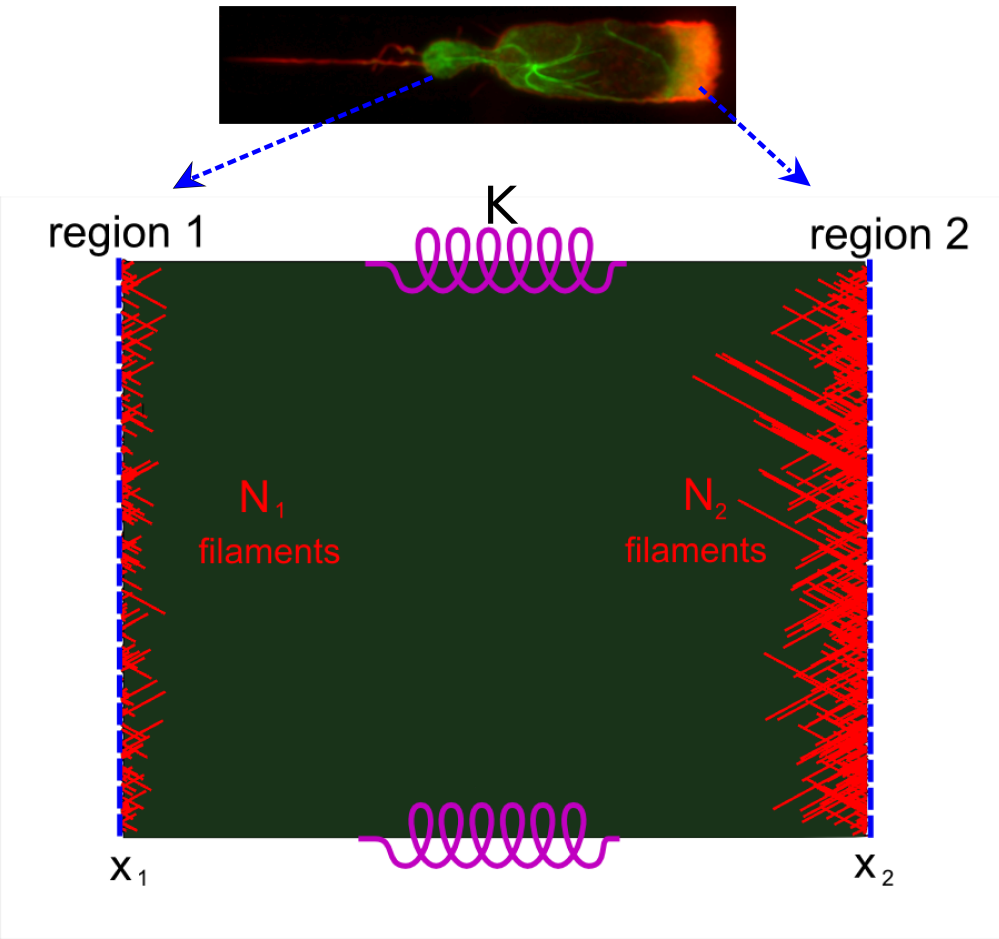

Figure 2.1: Schematic of model. Actin filaments are represented by red lines and the two nucleation regions by blue dashed lines. Springs mimicking the mechanical function of the cell membrane along the sides and top of the cell are shown in purple. The schematic is compared with a polarized neutrophil, where red labels polymerized actin and green labels tubulin [17] (https://www.london-nano.com/cleanroom-and-facilities/facilities/confocal-microscopes).

For l_0, we consider both small and large values implementing different physical assumptions. The "small" value corresponds to the critical nucleus required to nucleate an actin filament. We choose $l_0 = 8$ rather than commonly used values of $3-4$, for practical reasons. If l_0 is substantially smaller than 8, an unphysical scenario can occur in the stochastic simulations where all the filaments at the rear decay rapidly, so the extension vanishes. Then

all the filaments will nucleate at the leading edge and experience zero opposing force. We avoid this scenario, in order to focus on the the interactions mediated by membrane force. For the "large" value, we choose $l_0 = 100$. Here, the nucleation step in the model is viewed as including the first rapid steps in the filament life cycle in cells [48]. These include the creation of the filament and its growth until it is capped. The polymerization/depolymerization phase in our simulations corresponds to the last step in the life cycle, which is hydrolysis to ADP-actin and depolymerization.

This model is a first step in understanding the key interactions between mechanical force and actin polymerization. It is missing explicit treatment of several key features of importance in cells, including : i) barbed-end capping, which limits the length of filaments after they are nucleated, ii) ATP hydrolysis, which converts filament tips from growing to shrinking states (although hydrolysis it is included implicitly via the differences in critical concentrations between the barbed and pointed ends), and iii) autocatalytic filament nucleation [22], in which the rate of filament nucleation depends in the F-actin concentration. However, effects i) and ii) are included implicitly in our large-l_0 model, and the effect of iii) is evaluated in the **Discussion**. The model is highly simplified, but this simplicity allows us to develop and test an analytic approach based on a combination of rate equations and bifurcation analysis. This provides a roadmap for the analysis and interpretation of more complex models in the future.

Figure 2.2: Filament distribution from simulations, for parameters giving a symmetric steady state (frame a), and an polarized steady state (frame b). Color usage is as in Fig. 2.1.

2.2.2 Rate-Equation Model

Our rate-equation approach attempts to mimic the stochastic simulations using three local variables at each end of the cell, and one global variable. Our derivation of the rate equations is based on a biased-diffusion description [56] of polymerization and depolymerization. A filament with l F-actin subunits can polymerize to length $l+1$ or depolymerize to length $l-1$. The length l is viewed as a continuous random variable, and its distribution function is described by the diffusion equation

$$\frac{\partial \rho_i(l,t)}{\partial t} = D_i \frac{\partial^2 \rho_i(l,t)}{\partial l^2} - u_i \frac{\partial \rho_i(l,t)}{\partial l} + k_n \delta(l - l_0), \tag{2.5}$$

where the index i denotes the region in the cell and the boundary conditions are $\rho_i(l,t) = 0$ for $l = 0$ or $l \to \infty$. Here $D_i = \frac{1}{2}\left(k_i^+ + k_B^- + k_P^-\right)$ is the effective diffusion coefficient in

region i and

$$u_i = \left[k_i^+ - \left(k_B^- + k_P^-\right)\right] \tag{2.6}$$

is the effective convection coefficient. Eq. (2.5) differs from that given in Ref. [56] by the additional δ-function term, which describes the creation of new filaments with length l_0.

We choose the local variables to be the zeroth, first and second moments of ρ_1 and ρ_2, as defined in Ref. [57], and the global variable to be the tension T. Note that the zeroth moment is just the number of filaments: $N_i = \int \rho_i dl$. Similarly, the first moment is the F-actin count $F_i = \int l\rho_i dl$. Thus the free G-actin concentration is

$$G = G_0 - \frac{F_1 + F_2}{V}, \tag{2.7}$$

where V is the volume of the cell and G_0 is the initial free-actin concentration before polymerization begins.

The second moment $\Sigma_i = \int l^2 \rho_i dl$ highlights a very important feature of the length distribution: its spread. We work with the standard deviation $\sigma_i = \sqrt{\Sigma_i/N_i - F_i^2/N_i^2}$. The value of σ_i strongly affects the concentration of filaments near $l = 0$. Since these are the only filaments that can decay, this means that the decay rate of the filament number is strongly sensitive to σ_i.

Our equation set is:

$$\frac{dT}{dt} = K\delta\cos\alpha\left[k_1^+ + k_2^+ - 2k_B^- + \frac{k_B^-}{k_B^- + k_P^-}\left(k_1^d + k_2^d\right)\right] \tag{2.8}$$

$$\frac{dN_1}{dt} = k_n(G) - k_1^d N_1 \tag{2.9}$$

$$\frac{dN_2}{dt} = k_n(G) - k_2^d N_2 \tag{2.10}$$

$$\frac{dF_1}{dt} = k_n(G)l_0 + u_1 N_1 \tag{2.11}$$

$$\frac{dF_2}{dt} = k_n(G)l_0 + u_2 N_2 \tag{2.12}$$

$$\frac{d\Sigma_1}{dt} = k_n(G)l_0^2 + 2D_1 N_1 + 2u_1 F_1 \tag{2.13}$$

$$\frac{d\Sigma_2}{dt} = k_n(G)l_0^2 + 2D_2 N_2 + 2u_2 F_2, \tag{2.14}$$

where we have introduced the decay rate

$$k_i^d = \left(k_B^- + k_P^-\right)\frac{\partial_l \rho_i\left(l,t\right)\big|_{l=0}}{N_i} \tag{2.15}$$

and k_n is given by Eq. (2.4).

Eq. (2.8) is derived as follows. The relations $dX_1/dt = \delta\cos\alpha(k_1^+ - k_B^-)$ and $dX_2/dt = \delta\cos\alpha(-k_2^+ + k_B^-)$, together with Eqs. (2.1) and (2.2), justify the first three terms. Pointed-end depolymerization does not appear in Eq. (2.8) because it does not affect the tension. The fourth term results from overcounting of barbed-end depolymerization in the first three terms. When a filament consisting of a single subunit depolymerizes, the filament disappears.

In this case, the depolymerization does not affect the tension, which depends only on existing filaments (see Eq. (2.1)). Thus, the overcounted depolymerization contribution to $\dot{T}$ must be subtracted off. The overcounted depolymerization rate is $k_B^- \rho_i(1,t)$. On the other hand, since $\rho_i(0,t) = 0$, $\rho_i(1,t) \simeq \partial_l \rho_i(l,t)\big|_{l=0}$. Combining this with Eq. (2.15) gives the fourth term in Eq. (2.8).

The remaining equations are straightforwardly derived except for Eqs. (2.13), (2.14), and 2.15. Using Eq. (2.5), we obtain

$$\frac{d\Sigma_i}{dt} = \int_0^\infty l^2 \frac{\partial \rho_i(l,t)}{\partial t} dl = \int_0^\infty l^2 \left[D_i \frac{\partial^2 \rho_i(l,t)}{\partial l^2} - u_i \frac{\partial \rho_i(l,t)}{\partial l} + k_n \delta(l - l_0) \right] dl. \tag{2.16}$$

Then Eq. (2.13) and Eq. (2.14) are obtained by integrating the first two terms in Eq. (2.16) by parts. Eq. 2.15 is obtained from the definition $k_d N_i = (k_B^- + k_P^-)\rho(1,t)$, by again taking $\rho(1,t) \simeq \partial_l \rho_i(l,t)\big|_{l=0}$.

The contribution of nucleation to the dF/dt terms in Eqs. (2.11) and (2.12) gives corrections to the conventional formulas for the critical concentration G_c, where polymerization balances depolymerization [58]. For a bulk solution with no force acting on the filaments, and only one population N_1 of filaments, G_c is determined by the conditions $dF_1/dt = dN_1/dt = 0$. Multiplying Eq. (2.9) by l_0, and using Eq. (2.6), shows that $-k_1^d l_0 N_1 = (k_{on} G_c - k_B^- - k_P^-) N_1$, so that $G_c = (k_B^- + k_P^- - k_1^d l_0)/k_{on}$. The k_1^d term lowers G_c, corresponding to the physical effect that nucleation removes free monomers from solution. When tension is are present, the polymerization rate is reduced and the critical concentration is increased. As we shall see later, the tension is higher when the cell is polarized,

corresponding to a higher free-actin concentration.

Because our expressions involve $\partial_l \rho_i(l,t)\big|_{l=0}$ in addition to the moments, it is necessary to estimate this quantity. For calculating steady-state solutions of the equations, $\partial_l \rho_i(l,t)$ can be obtained from the steady-state solution $\rho_i^{ss}(l,t)$ of Eq. (2.5). By matching the boundary conditions at $l=0$, and $l=\infty$, and enforcing continuity at $l=l_0$, we obtain

$$\rho_i^{ss}(l) = \begin{cases} \frac{k_n}{u_i}\left[\exp\left(\frac{u_i}{D_i}l\right) - 1\right] & l \le l_0 \\ \frac{k_n}{u_i}\left[1 - \exp\left(-\frac{u_i}{D_i}l_0\right)\right]\exp\left(\frac{u_i}{D_i}l\right) & l \ge l_0 \end{cases} \tag{2.17}$$

Note that the exponential in the second of Eqs. 2.17 is decaying because u_i must be negative in steady state, to counter contributions to dF_i/dt from nucleation.

From Eq. (2.17), we can calculate the three moments:

$$N_i = -\frac{k_n}{u_i}l_0 \tag{2.18}$$

$$F_i = N_i\left(\frac{l_0}{2} - \frac{D_i}{u_i}\right) \tag{2.19}$$

$$\Sigma_i = \frac{1}{3}N_i l_0^2 - F_i l_0 + 2\frac{F_i^2}{N_i}. \tag{2.20}$$

By solving for k_n/u_i and u_i/D_i in terms of N_i and F_i, we obtain

$$\rho_i^{ss}(l) = \begin{cases} \frac{N_i}{l_0}\left[1 - \exp\left(-\frac{l}{l_i - l_0/2}\right)\right] & l \le l_0 \\ \frac{N_i}{l_0}\left[\exp\left(\frac{l_0}{l_i - l_0/2}\right) - 1\right]\exp\left(-\frac{l}{l_i - l_0/2}\right) & l \ge l_0, \end{cases} \tag{2.21}$$

where $l_i = F_i/N_i$ are the mean filament lengths (measured in subunits). Differentiating Eq.

(2.21) and inserting into Eq. (2.15), we obtain the steady state decay rate:

$$k_i^d\big|_{ss} = \frac{k_i^+ + k_B^- + k_P^-}{2l_0} \frac{1}{l_i - \frac{1}{2}l_0}. \tag{2.22}$$

We note that it is mathematically possible for the decay rate in Eq. (2.22) to become negative, if l_i becomes less than $l_0/2$. This cannot occur in the stochastic treatment, because even in the extreme limit of no polymerization, $l_i = l_0/2$. However, because the rate equations are approximate, it can happen in rare cases that $l_i < l_0/2$. We avoid this by limiting ourselves to parameter values where the filaments are not too short.

The steady-state values of k^d from Eq. (2.22), together with Eqs. (2.8-2.14), specify a dynamical system whose solution will give correct fixed points. However, it will not necessarily describe the dynamics of actin polymerization correctly, because the k_i^d obtained by Eq. (2.22) are only guaranteed to be correct at steady state. Obtaining the k_i^d exactly from Eq. (2.15) would require knowledge of all the moments of ρ, or another numerical approach to calculating ρ, both of which are impractical. Therefore, to obtain a practical approach, we truncate our description of ρ at the second moment. We devise a correction to Eq. (2.22) with a form $k_i^d = f\left(\sigma_i, l_i\right) k_i^d\big|_{ss}$ based on the standard deviation σ_i and the average filament length l_i. We take the correction to have the functional form

$$f\left(\sigma_i, l_i\right) = \frac{\left(\sigma_i/\sigma_i^{ss}\right)^n}{\left(l_i/l_i^{ss}\right)^m}, \tag{2.23}$$

where σ_i^{ss} and l_i^{ss} are the steady state values of σ_i and l_i calculated from Eqs. (2.18), (2.19)

and (2.20). This form is chosen for simplicity, and is guaranteed to give the correct values of k_i^d at steady state. Fits to the decay rate obtained from the stochastic simulations for baseline values of the bifurcation parameters, plus an additional set using a k_P^- value equal to 150% of its baseline value, obtained the best agreement for $n = 3$ and $m = 1.6$. Thus, the corrected decay rate reads:

$$k_i^d\big|_{corr} = \frac{\left(\sigma_i/\sigma_i^{ss}\right)^3}{\left(l_i/l_i^{ss}\right)^{1.6}} k_i^d\big|_{ss}. \tag{2.24}$$

The physical mechanism underlying the correction is shown in Fig. 2.8. The blue curve has a larger variance σ than the red one, although they have the same zeroth moment N and first moment F. The larger spread in the blue curve causes a larger value of $\partial_l \rho_i\,(l,t)$ at the origin, increasing the filament decay rate according to Eq. (2.15).

In our implementation of this approach, we obtained n and m from a given parameter set, and tested the resulting method over a broad range of parameter values, from 50% to 150% of their baseline values. We found consistently improved agreement with the dynamic stochastic simulations (see Stochastic Results below), relative to using the steady-state k_i^d values. The correction in Eq. (2.24) thus appears to be a broadly applicable approach. However, it is not essential for the the steady-state stability of the polarized vs. the unpolarized state.

2.3 Stochastic Results

The simulation parameters are given in Tables 2.1 and 2.2. Some of these are kept constant for all of the runs, while other key parameters, which can be adjusted experimentally, are

tuned to drive symmetry-breaking transitions. K is chosen such that the time for the cell to equilibrate is moderate. We also chose K large enough to eliminate excessive volume changes. The tuned parameters G_0, k_P^-, k_B^-, and k_r are given relative to baseline values (see Table 2.2), which define the threshold between polarized and unpolarized states. They are in the same general range as existing estimates, but some of them differ from the values typically used to fit *in vitro* experiments (see Ref. [54]). Relative to standard parameters, the main difference is that our value of k_B^- is larger and k_P^- is smaller. This choice is made in order to maintain a reasonable filament length in our simplified model, while keeping the tension continuous during the transition from the symmetric to asymmetric state. Note that in the four-dimensional parameter space there are many possible choices of baseline values at the threshold. Our results are fairly independent of the particular choice of baseline values. For example, we have increased k_P^{-c} by 35% and k_B^{-c} by 20 %, which kept the system at the threshold. The critical values of the other parameters did not change, and the shape of the bifurcation plots was the same. Figs. 2.3, 2.4, and 2.9-2.11 present typical time courses of

Parameter	Value (for both small and large l_0)
Temperature	$300K$
K	$5.7pN/nm$
k_{on}	$11.6M\mu^{-1}s^{-1}$ (Ref. [59])
δ	$2.7\ nm$

Table 2.1: Values of constant parameters. K is the spring constant, k_{on} is the polymerization rate, and δ is the length increment per monomer.

the filament count N and the polymerized-actin count F at the two ends of the cell. Figure 2.3 shows results for the unpolarized regime. At the beginning of the simulation, actin

Parameter	Baseline value (small l_0)	Baseline values (large l_0)
G_0^c	$12\mu M$	$12\mu M$
k_P^{-c}	$0.05s^{-1}$	$0.05s^{-1}$
k_B^{-c}	$2.9s^{-1}$	$2.9s^{-1}$
k_r^c	$70\mu M^{-2}s^{-1}$	$2.5\mu M^{-2}s^{-1}$

Table 2.2: Baseline values of key parameters that are varied.

filaments nucleate and polymerize very rapidly (within about a second). The nucleation is fast because of the high initial G-actin concentration and the G^2-dependence of the nucleation rate. In the small-l_0 case, the cell polarizes after the initial period. Then the polarization decays to symmetric steady state results. The time scale of the convergence to the final symmetric state is slow because the only disassembly mechanism included in the model is depolymerization; disassembly by severing would lead to faster convergence. The dynamics of N are fairly similar to those of F. In the large-l_0 case, the initial polarization phase is absent.

Increasing or decreasing the key parameters relative to the baseline values, while keeping the other parameters fixed, causes symmetry breaking. This is seen in Figs. 2.4 and (2.9-2.11), where individual parameters are varied from 50% to 150% of their baseline values while the others remain fixed. The polarization jumps rapidly over a period of a few hundred seconds, and then slowly drops to a finite value. The large-l_0 results are similar to the small-l_0 results. Polarization is favored by large G_0, large k_P^-, small k_B^-, and small k_r. Again, the dynamics of N are similar to those of F.

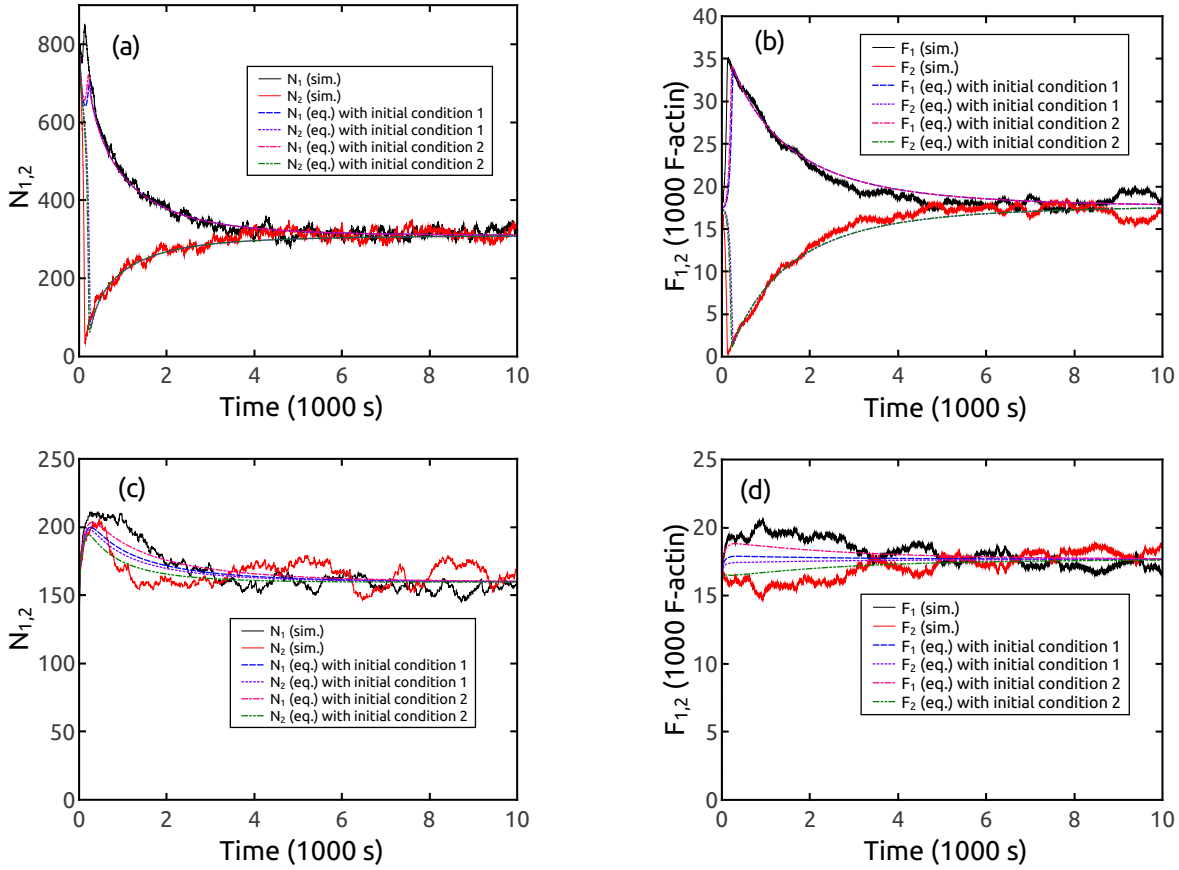

Figure 2.3: Dynamics of F and N before reaching symmetric steady states, for $k_P^- = 0.5k_P^{-c}$ (see Table 2.2). Other parameters are as in Tables 2.1 and 2.2. Frames a) and b) are for small l_0, while frames c) and d) are for large l_0.

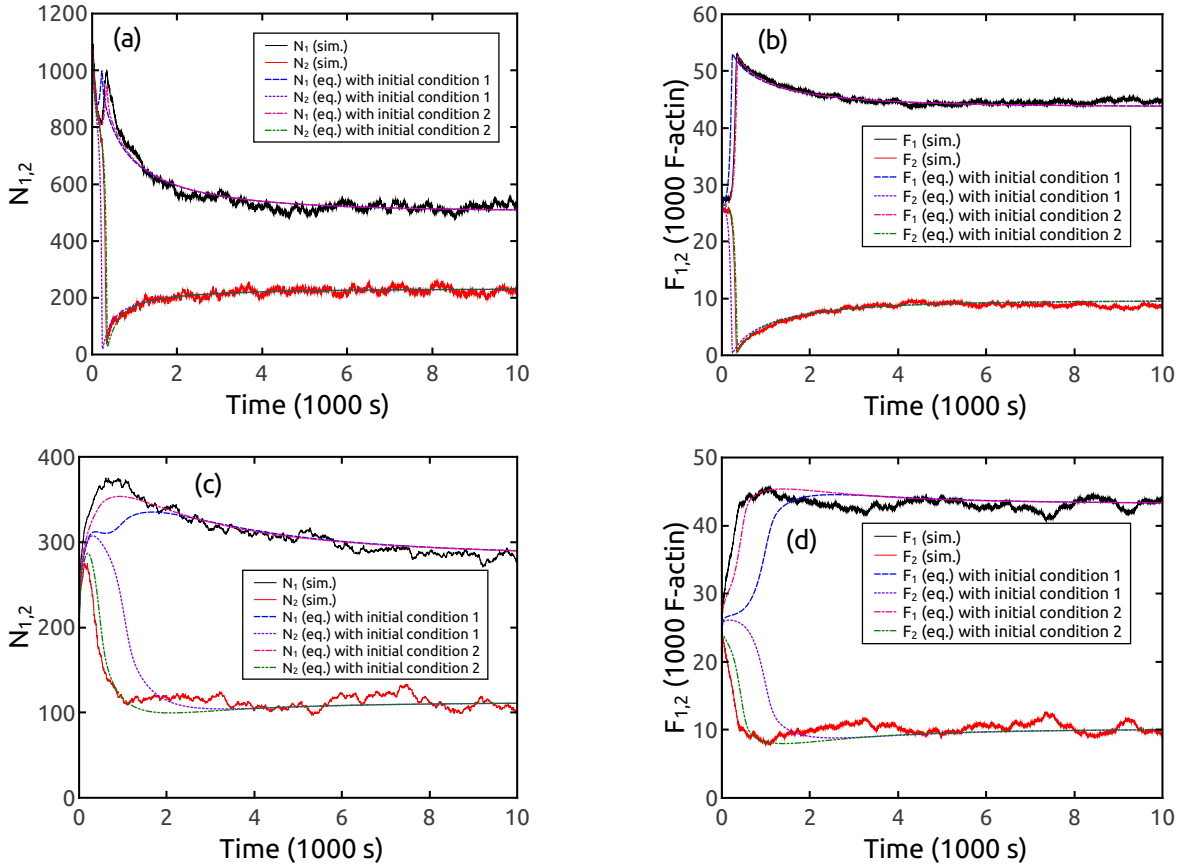

Figure 2.4: Dynamics of F and N before reaching asymmetric steady states, for $G_0 = 1.5G_0^c$ (see Table 2.2). Other parameters have the values given in Tables 2.1 and 2.2. Frames a and b are for small l_0 and frames c and c are for large l_0.

2.4 Rate-Equation Results

It is not possible for a deterministic rate-equation approach to precisely reproduce the dynamics leading to polarization from a symmetric starting point, since the polarization results from the growth of an initial stochastic fluctuation. Thus we use two sets of slightly asymmetric initial conditions to solve Eqs. (2.8-2.14). Set 1 has a minimal asymmetry: $N_1 = 2$, $N_2 = 1$, $F_1 = 2l_0$, $F_2 = l_0$, $\Sigma_1 = 2l_0^2$, $\Sigma_2 = l_0^2$. Set 2 consists of stochastic-simulation values of T, $N_{1,2}$, $F_{1,2}$ and $\Sigma_{1,2}$ evaluated (for the same parameter set) after 1 second of simulation

time, so that the rate equations start at $t = 1s$. In this way the rate-equations treat the entire dynamics of polarization, except for its very initial stages. As seen in Figs. 2.3 and 2.4, the rate-equation results for small l_0 match those from the stochastic simulation well for both the dynamic behavior and steady state values of F, independent of initial conditions. For large l_0, the results are more sensitive to initial conditions. Using initial conditions 1 leads to noticeable delays in the polarization, while these delays are much smaller when using initial conditions 2.

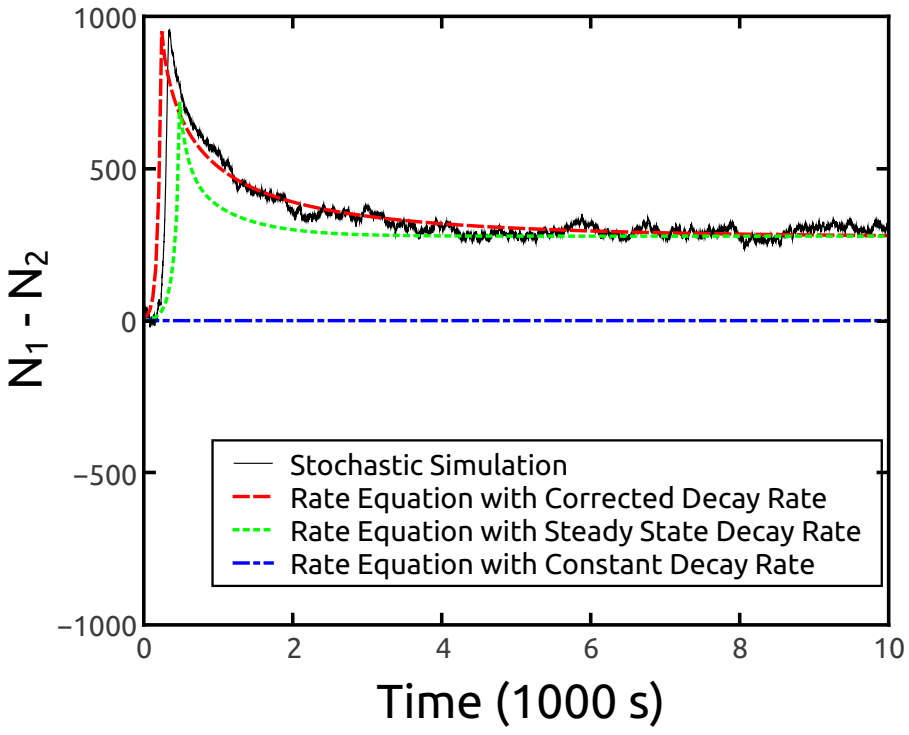

Figure 2.5: Dynamics of cell polarization, for different treatments of the filament decay rate k_d. Parameters: $G_0^c = 1.5G_0^c$ (see table 2.2). Other parameters have the values given in Tables 2.1 and 2.2. Initial conditions are $N_1 = 2$, $N_2 = 1$.

To evaluate the necessity of the correction in Eq. (2.23) for accurate polymerization

dynamics, Fig. 2.5 shows results for $N_{1,2}$ with the correction (using Eq. (2.24)), and without the correction (using Eq. (2.22)), together with stochastic-simulation results for a typical polarized case. The rate-equation dynamics with the correction are much closer to the simulation dynamics. The curve with constant decay rate drops well below the stochastic-simulation curve at around 2000s, while the curve with the corrected decay state follows the stochastic-simulation curve closely. As a indicator of how methods typically used in the literature perform, we also show results for a constant decay rate set to be 50% greater than the average of the decay rates in the two regions at steady state. The polarization in both the initial period and steady state disappears completely. Other constant values of the decay rate also abolish the polarization. Thus the prediction of either steady-state or dynamic properties of polarization requires the use of a state-dependent decay rate.

2.5 Bifurcation Analysis of the Rate-Equation Results

Bifurcation analysis is an efficient method for understanding the qualitative behaviour of symmetry-breaking transitions, pinning down key interactions, and establishing possible long-term behaviors of a dynamical system [25]. By examining the stability of the solution of a dynamical system via diagonalization of a small matrix, one can find bifurcations and establish the key interactions responsible for the bifurcations. Such an instability analysis cannot be used directly for the stochastic simulations, but our development of a dynamical system in Eqs. (2.8-2.14) that mimics the simulation results allows us to perform a stability analysis of the unpolarized state. Because we seek only steady-state properties, we simplify the analysis by using the steady-state version of the decay rate from Eq. (2.22), so the

variables $\Sigma_{1,2}$ are not required. Fig. 2.6 shows the bifurcation diagram obtained from both the rate-equation calculation and the stochastic simulation. For each data point on the bifurcation diagram, both the simulation and rate equations were run for 50,000 seconds. The rate-equation result is the last data point, while the simulation result is the time average of the last 20,000-30,000 seconds' data. The results from the two approaches match well, showing that the rate-equation method handles the bifurcation accurately. The continuous variation of the polarization as the various parameters are adjusted, together with the symmetry-breaking nature of the transition, suggests that the bifurcation is a supercritical pitchfork bifurcation [25]. Polarization is favored by increasing G_0 and k_P^-, and decreasing k_B^- and k_r.

The symmetry breaking mechanism driving polarization results from an instability of the symmetric steady state to small perturbations. We perform a quantitative analysis of the instability, and identify the feedback loop that causes it. The instability is determined by the 5×5 Jacobian matrix [25] of the five variables T, $N_{1,2}$ and $F_{1,2}$, evaluated in a symmetric state. If all of the eigenvalues of this matrix are negative, the symmetric state is stable; if one or more is positive, the symmetric state is unstable. We force the system to be in a (potentially unstable) symmetric state by requiring that $N_1 = N_2$ and $F_1 = F_2$ as we solve the equations. If this restriction is lifted, for some parameter values the system will leave the symmetric steady state and polarize spontaneously. For clarity, we use symmetrized variables: N_1, $N_2 \rightarrow N = 1/2\,(N_1 + N_2)$, $\Delta N = 1/2\,(N_1 - N_2)$, and F_1, $F_2 \rightarrow$

$F = 1/2\,(F_1 + F_2)$, $\Delta F = 1/2\,(F_1 - F_2)$. The Jacobian matrix is then

$$\hat{A} = \begin{pmatrix} \frac{\partial \dot{T}}{\partial T} & \frac{\partial \dot{T}}{\partial N} & \frac{\partial \dot{T}}{\partial F} & \frac{\partial \dot{T}}{\partial \Delta N} & \frac{\partial \dot{T}}{\partial \Delta F} \\ \frac{\partial \dot{N}}{\partial T} & \frac{\partial \dot{N}}{\partial N} & \frac{\partial \dot{N}}{\partial F} & \frac{\partial \dot{N}}{\partial \Delta N} & \frac{\partial \dot{N}}{\partial \Delta F} \\ \frac{\partial \dot{F}}{\partial T} & \frac{\partial \dot{F}}{\partial N} & \frac{\partial \dot{F}}{\partial F} & \frac{\partial \dot{F}}{\partial \Delta N} & \frac{\partial \dot{F}}{\partial \Delta F} \\ \frac{\partial \Delta \dot{N}}{\partial T} & \frac{\partial \Delta \dot{N}}{\partial N} & \frac{\partial \Delta \dot{N}}{\partial F} & \frac{\partial \Delta \dot{N}}{\partial \Delta N} & \frac{\partial \Delta \dot{N}}{\partial \Delta F} \\ \frac{\partial \Delta \dot{F}}{\partial T} & \frac{\partial \Delta \dot{F}}{\partial N} & \frac{\partial \Delta \dot{F}}{\partial F} & \frac{\partial \Delta \dot{F}}{\partial \Delta N} & \frac{\partial \Delta \dot{F}}{\partial \Delta F} \end{pmatrix}, \tag{2.25}$$

where the derivatives with respect to the new variables are

$$\frac{\partial}{\partial N} = \frac{\partial}{\partial N_1} + \frac{\partial}{\partial N_2} \text{ and } \frac{\partial}{\partial \Delta N} = \frac{\partial}{\partial N_1} - \frac{\partial}{\partial N_2}, \tag{2.26}$$

with similar expressions for $\partial/\partial F$ and $\partial/\partial \Delta F$.

The calculation is simplified by the decoupling of a 2×2 submatrix from the rest of the matrix. Since Eqs. (2.8-2.12) are invariant under the operation $N_1, F_1 \leftrightarrow N_2, F_2$ the variables can be chosen to be either symmetric or symmetric under this operation. $\dot{T}$, $\dot{N}$ and $\dot{F}$ are symmetric under the operation, while $\Delta\dot{N}$ and $\Delta\dot{F}$ are asymmetric. Therefore the elements of $\hat{A}$ coupling ΔN and ΔF to the other variables vanish, so that

$$\hat{A} = \begin{pmatrix} \frac{\partial \dot{T}}{\partial T} & \frac{\partial \dot{T}}{\partial N} & \frac{\partial \dot{T}}{\partial F} & 0 & 0 \\ \frac{\partial \dot{N}}{\partial T} & \frac{\partial \dot{N}}{\partial N} & \frac{\partial \dot{N}}{\partial F} & 0 & 0 \\ \frac{\partial \dot{F}}{\partial T} & \frac{\partial \dot{F}}{\partial N} & \frac{\partial \dot{F}}{\partial F} & 0 & 0 \\ 0 & 0 & 0 & \frac{\partial \Delta \dot{N}}{\partial \Delta N} & \frac{\partial \Delta \dot{N}}{\partial \Delta F} \\ 0 & 0 & 0 & \frac{\partial \Delta \dot{F}}{\partial \Delta N} & \frac{\partial \Delta \dot{F}}{\partial \Delta F} \end{pmatrix} \tag{2.27}$$

We define the lower right 2×2 sub-matrix of $\hat{A}$ to be

$$\hat{a} = \begin{pmatrix} \frac{\partial \Delta \dot{N}}{\partial \Delta N} & \frac{\partial \Delta \dot{N}}{\partial \Delta F} \\ \frac{\partial \Delta \dot{F}}{\partial \Delta N} & \frac{\partial \Delta \dot{F}}{\partial \Delta F} \end{pmatrix} \tag{2.28}$$

Numerical diagonalization of $\hat{A}$ reveals four eigenvalues that are always negative, and one that is positive for parameters that yield polarization. This eigenvalue is one of the eigenvalues of the $\hat{a}$ submatrix. Thus the symmetry-breaking instability is determined by $\hat{a}$ and independent of the other parts of $\hat{A}$. The interactions driving the instability can then be identified by examining the signs of the elements of $\hat{a}$:

i) $\partial \Delta \dot{N} / \partial \Delta N < 0$. This is derived in **Appendix B**.

ii) $\partial \Delta \dot{F} / \partial \Delta F = 0$. According to Eqs. (2.11) and (2.12), $\Delta \dot{F}$ is not explicitly dependent on ΔF. The only dependence of these equations on F_1 and F_2 is via G, and G depends on the total F-actin number F, but not on ΔF.

iii) $\partial \Delta \dot{N} / \partial \Delta F > 0$. A positive ΔF corresponds to increasing F_1 while keeping N_1 constant. This causes the filaments in region 1 to be longer. The longer filaments will

decrease the decay rate according to Eq. (2.22), and thus increase $\Delta\dot{N}$. As for case *ii)* above, G entering k_n does not depend on ΔF.

iv) Finally, two competing mechanisms determine $\partial\Delta\dot{F}/\partial\Delta N$, so it can be either positive or negative. Differentiation of Eqs. (2.11) and (2.12) shows that

$$\frac{\partial\Delta\dot{F}}{\partial\Delta N} = \frac{1}{2}T\delta\beta\left(\frac{k_1^+}{N_1} + \frac{k_2^+}{N_2}\right) + \frac{1}{2}\left(k_1^+ + k_2^+\right) - \left(k_B^- + k_P^-\right). \tag{2.29}$$

a) The positive contribution comes from the first term in Eq. (2.29). Positive ΔN reduces the force per filament in region 1 while increasing the force per filament in region 2. Then the polymerization rate given by Eq. (2.3) in region 1 will be greater than that in region 2. The difference in the polymerization rates created by ΔN then increases ΔF, so the contribution to $\partial\Delta\dot{F}/\partial\Delta N$ is positive.

b) The negative contribution comes from the remaining terms in Eq. (2.29). Increasing ΔN increases the number of barbed and pointed ends in Region 1. At steady state, depolymerization exceeds polymerization because the sum of depolymerization and polymerization must cancel the actin subunits added by filament nucleation. Therefore, F-actin in region 1 will depolymerize faster than in region 2. Thus the contribution to $\partial\Delta\dot{F}/\partial\Delta N$ is negative.

It is shown in **Appendix B** that, since $\partial\Delta\dot{N}/\partial\Delta N < 0$, $\partial\Delta\dot{F}/\partial\Delta F = 0$, and $\partial\Delta\dot{N}/\partial\Delta F > 0$, polarization will occur only if $\partial\Delta\dot{F}/\partial\Delta N > 0$, so that the positive contribution exceeds the negative contribution. Thus the transition in the sign of this element drives the transition from a symmetric steady state to an asymmetric one. As shown under iv), this transition occurs when the interactions between N and F mediated by force become strong, which re-

quires that the polymerization rate decreases with opposing force. The feedback loop driven by $\partial\Delta\dot{F}/\partial\Delta N > 0$ is illustrated in Fig. 2.7, where the arrow leading from ΔF to ΔN is always positive as discussed under *iii)*, while the one from ΔN to ΔF can be either negative or positive depending on the magnitude of the tension T.

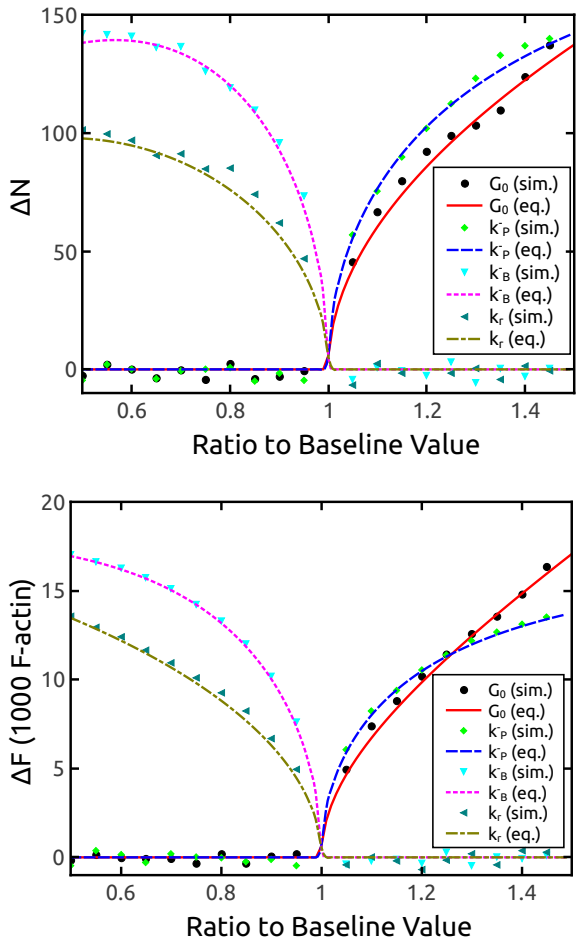

Figure 2.6: Bifurcation diagram of polarization as function of G_0, k_P^-, k_B^-, k_r, using the small l_0 value. The parameters are varied from $0.5G_0^c$, $0.5k_P^{-c}$, $0.5k_B^{-c}$, $0.5k_r^c$ to $1.5G_0^c$, $1.5k_P^{-c}$, $1.5k_B^{-c}$, $1.5k_r^c$. In the simulation, each parameter is varied by 5% from dot to dot. In the rate equations, each parameter is varied by 1%, forming a smooth curve.

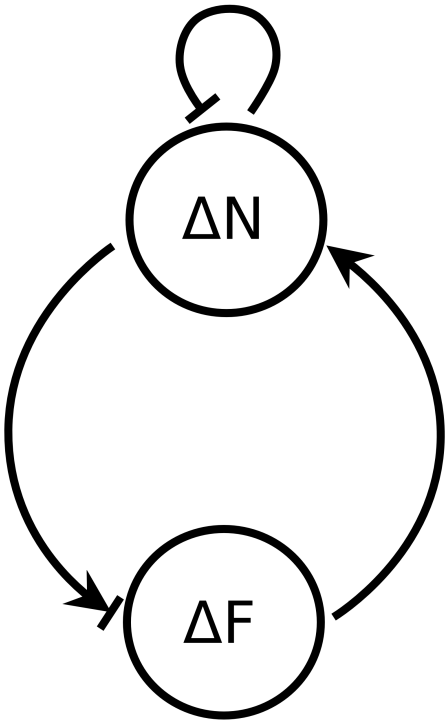

Figure 2.7: Schematic of essential feedback loop that leads to polarization.

2.6 Discussion

In the previous section, we identified the key feedback loop in our model that destabilizes a symmetric steady state and thus causes polarization. This loop is based on three physical mechanisms relating ΔF to ΔN. Here we explore the relevance of the results obtained in this highly simplified model to the behavior of real cells, and analyze the parameter dependence in more depth.

First we compare the model predictions with the key experimental findings and previous theory. In Ref. [6], the authors laser-severed the body of a polarized cell from the leading edge and a new leading edge grew out of the cell body. To simulate this experiment, we

cleaved a polarized cell in the model, cutting off the leading edge together with 70% of the original cell. Then the remaining cell body grew a new leading edge, consistent with Ref. [6]. We find that under this protocol, the new leading edge always is where the rear of the unsevered cell was previously. Of the two examples illustrated in Fig. 3 of Ref. [6] (one using laser severing and the other spontaneous severing), the leading edge in one case was at the old rear of the unsevered cell, and in the other case it was on the opposite side. If we use a different protocol, where the filaments in the cell "body" depolymerize after the cleavage, the new leading edge is randomly located, consistent with Ref. [6].

On the other hand, the model does not reproduce the phenomenology of Ref. [4], where imposition of force caused a transition from a symmetric state to a polarized state. In the model, initially symmetric cells always return to a symmetric state after imposition of force, as expected from the supercritical nature of the bifurcation. It may be that reproducing the observed behavior requires the inclusion of additional nonlinear mechanical terms as in Ref. [28].

As discussed in the **Introduction**, most previous theories of cell polarization have assumed a combination of diffusion and chemical reactions containing positive and negative feedbacks of proteins and lipds including Rac, PIP3, PTEN, and myosin. The model described here differs from these in that it does not assume explicit chemical feedback terms and requires no myosin activity. Rather, the positive-feedback terms that cause the polarization result from a combination of force generation by polymerization, the force sensitivity of polarization, and the effect of filament length on the filament decay rate. Of the models

currently in the literature, the present model is closest in spirit to that of Ref. [27]. However, it differs from that model in that it does not require autocatalytic actin filament nucleation.

The mechanochemical feedback loop described here has some points in common with that discussed in Ref. [60] for focal adhesions. In that work, force was taken to regulate assembly of focal adhesions via a mechanism in which tensile stress lowers the chemical potential of assembled subunits relative to unassembled ones, enhancing assembly. In the present mechanism, force enters the feedback loop of Fig. 2.7 mainly via the effect of ΔN on $\Delta\dot{F}$. The reduction in the force per filament at one end of the cell that results from an increased ΔN causes $\Delta\dot{F}$ to increase at that end as well. The main physics underyling this is the well-known Brownian-ratchet effect [21], in which compressive stress on the tip of a filament reduces the on-rate. We believe that this is a special case of the rigorous thermodynamic results described in Ref. [60].

Next we use our basic feedback loop to physically interpret the parameter dependences of polarization found in the simulation and rate-equation results. We found that polarization is favored by increased G_0 and k_P^- and reduced k_B^- and k_r. Eq. (2.29) shows that the key matrix element determining polarization is strongly dependent on T. Therefore, we based our analysis of the parameter dependence of polarization on T.

a) Increasing G_0 increases the net barbed-end polymerization rate and thus T, favoring polarization.

b) Increasing k_P^- increases G, which again increases T and favors polarization.

c) Decreasing k_B^- increases the net polymerization rate of barbed ends, which increases

T and thus favors polarization.

d) Decreasing k_r causes more actin to be polymerized into filaments, and less to be used up in nucleation events. Because nucleation events by assumption do not generate tension (see Eq. (2.8)), focusing more of the free actin into polymerization increases T. This favors polarization.

Although the model is very simplified, some of these predicted trends might apply to cells where mechanical feedbacks are important. For example, G_0 can be reduced by latrunculin treatment. Our finding that reduced G_0 impairs cell polarization is thus consistent with the finding that latrunculin prevents polarization of HL-60 cells induced by a uniform attractant concentration [61]. We do not see how to vary k_P^- and k_B^- individually in a cell. However, actin disassembly is accelerated by cofilin, which might preferentially accelerate disassembly at one filament end relative to the other. Decreasing k_r reduces the non-branching nucleation rate. Since formins are believed to cause non-branching nucleation, while Arp2/3 complex causes branching nucleation, downregulation of formin activity might correspond to reducing k_r.

Finally, we explore the extent to which the basic picture embodied by Fig. 2.7, and criteria i) - iv) given above, will persist in more complete treatments of cell polarization:

i) $\partial\Delta\dot{N}/\partial\Delta N < 0$. Since the decay rate $\dot{N}_1$ contains a term proportional to N_1, this inequality will hold unless the nucleation rate on the "1"-side increases, or k_d^1 decreases, with increasing N_1. An increase of the nucleation rate with N_1 could result from autocatalytic nucleation by filament branching [22, 54]. It is not certain whether autocatalytic branching

depends on N_1 or on F_1. *In vitro*, where actin nucleation factors are uniformly distributed in solution, branches occur along the length of the filament, suggesting a dependence on F_1. However, in cells, branches are formed only near the membrane, so the filament length may not be an important factor. In this case the autocatalytic branching rate would depend on N_1. If this causes $\partial\Delta\dot{N}/\partial\Delta N$ to make a transition from negative to positive, and $\mathcal{D} > 0$, then Eq. (2.32) shows that the eigenvalues will make a transition from having negative real part with a nonzero imaginary part to having a positive real part with a nonzero imaginary part (a Hopf bifurcation [25]). Eigenvalues with positive real part and nonzero imaginary part correspond to a polarization that oscillates over time, as was observed in Ref. [62].

A decrease in k_d^1 with increasing N_1 could occur with a different decay mechanism. Refs. [41] and [46] suggested a "crushing" mechanism where filaments at the rear of the cell are broken by large force. Such a mechanism would be expected by have a decay rate roughly of the form $k_d^1 \propto exp(const \times T/N_1)$, which decreases as a function of N_1. This could also lead to a Hopf bifurcation to an oscillating state, under appropriate circumstances.

ii) $\partial\Delta\dot{F}/\partial\Delta F = 0$. The main correction to this result would come from steric crowding of actin, which would suppress polymerization where F is large and make $\partial\Delta\dot{F}/\partial\Delta F$ negative. In this case, instability would still require a positive determinant for $\hat{a}$, but now the determinant includes an extra contribution from the product of the diagonal terms. This means that $\partial\Delta\dot{F}/\partial\Delta N$ would have to exceed a positive minimum critical value for polarization to occur.

iii) $\partial\Delta\dot{N}/\partial\Delta F > 0$. This should hold quite generally, since the filament lifetime should

increase with its length. As mentioned above, another positive contribution to $\partial\Delta\dot{N}/\partial\Delta F$ is present if side branching dominates. An additional possibility is the generation of new filaments by severing of existing filaments, which would provide a positive contribution provided that the severed fragments remain attached to the network [63, 64].

iv) $\partial\Delta\dot{F}/\partial\Delta N$ has two competing contributions, a positive one from the force dependence of the polymerization rate, and the second one from the shorter lifetime associated with shorter filaments. These factors should also be present in real cells. However, some studies [65] have indicated that the polymerization velocity can have a force-independent plateau, and the positive term would be absent in this regime, abolishing polarization unless other positive-feedback effects become prominent.

We emphasize that obtaining criterion iii) depends crucially on having a state-dependent filament decay rate. If the decay rate is taken to be constant, then $\partial\Delta\dot{N}/\partial\Delta F = 0$, and there is no polarization unless autocatalytic branching or severing come into play.

The actual matrix of interactions describing a real cell is larger than that considered here. At the linear level asymmetric variables like ΔN and ΔF are still decoupled from symmetric variables. But other asymmetric variables are present, including those describing the distributions of upstream signaling proteins. In addition, beyond the linear level cell polarization might occur by a discontinuous change in several variables. In this case, changes in the symmetric variables could be coupled to changes in the asymmetric variables. However, the present analysis based on ΔN and ΔF provides a starting point for understanding the mechanical interactions driving cell polarization.

The model studied here treats only two networks, one at the front and one at the back of the cell, interacting with rigid boundaries. Extending the analysis to more general cell shapes with multiple networks, and deformable boundaries, could reveal several new types of phenomemena. For example, in a circular cell shape the orientation of the wave could gradually shift over time, rather than being constrained to discrete jumps of 180°. This could lead to motion that over long times is like a correlated random walk. Including membrane flexibility might allow traveling waves of polymerized actin to form along the edge of the cell, although such waves probably would require additional negative feedback mechanisms [66]. Treating a circular cell shape could be accomplished by two modifications. First, the main system variables, F and N, could be transformed into continuously varying functions along the cell periphery. Similarly, the tension would be transformed into a force density varying continuously along the membrane. It is likely that some terms penalizing excessive variations along the periphery would be required, so that the system would be described by partial differential equations. Achieving more realistic cell shapes requires the inclusion of membrane flexibility. This has been a challenge for cell migration modelers, but a promising class of approaches is based on the "phase-field" method [47].

2.7 Conclusion

We have systematically derived a rate-equation model of force-dependent actin polymerization from known biochemical processes and their force dependence. The polarization predicted by steady state solution of the rate equations agrees with our stochastic-simulation results to within 5%. A modification of the model was shown to treat dynamic effects accu-

rately as well. The model results show that a polarized F-actin distribution can result from a a combination of force generated by polymerization, the slowing of polymerization by opposing force, and the dependence of the filament decay rate on the filament length. The feedback loop driving polarization results from reciprocal interactions between the asymmetry ΔN in the number of filaments between the two ends of the cell, and the corresponding asymmetry ΔF of the amount of polymerized actin. For appropriate parameter values, ΔN and ΔF grow synergistically, so that ΔN feeds the growth of ΔF, and vice versa. Polarization is favored by large values of the pointed-end off-rate and the free-monomer concentration, and small values of the barbed-end off-rate and random-nucleation rate. Obtaining correct polarization dynamics requires the use of information about the effect of the variance of the filament length on the filament decay rate. The improvements in rate-equation descriptions of actin polymerization described here should be useful in future efforts to model whole-cell structure and function, using methods such as the "Virtual Cell" approach [67].

2.8 Appendix A: Additional Figures

In this section, we show the schematic of the length distribution, mentioned in the **Model** section, see Fig. 2.8. We also show the time courses leading to polarized steady states, for variations in the three key parameters k_P^-, k_B^- and k_r. For each parameter, both the small l_0 and large l_0 cases are considered, see Figs. 2.9, 2.10 and 2.11.

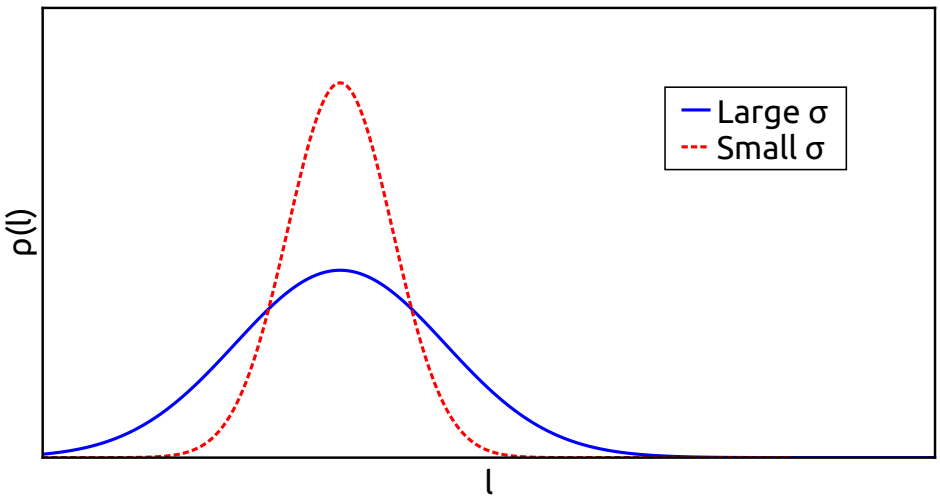

Figure 2.8: Schematic of two possible filament-length distributions, with the blue line having a larger standard deviation.

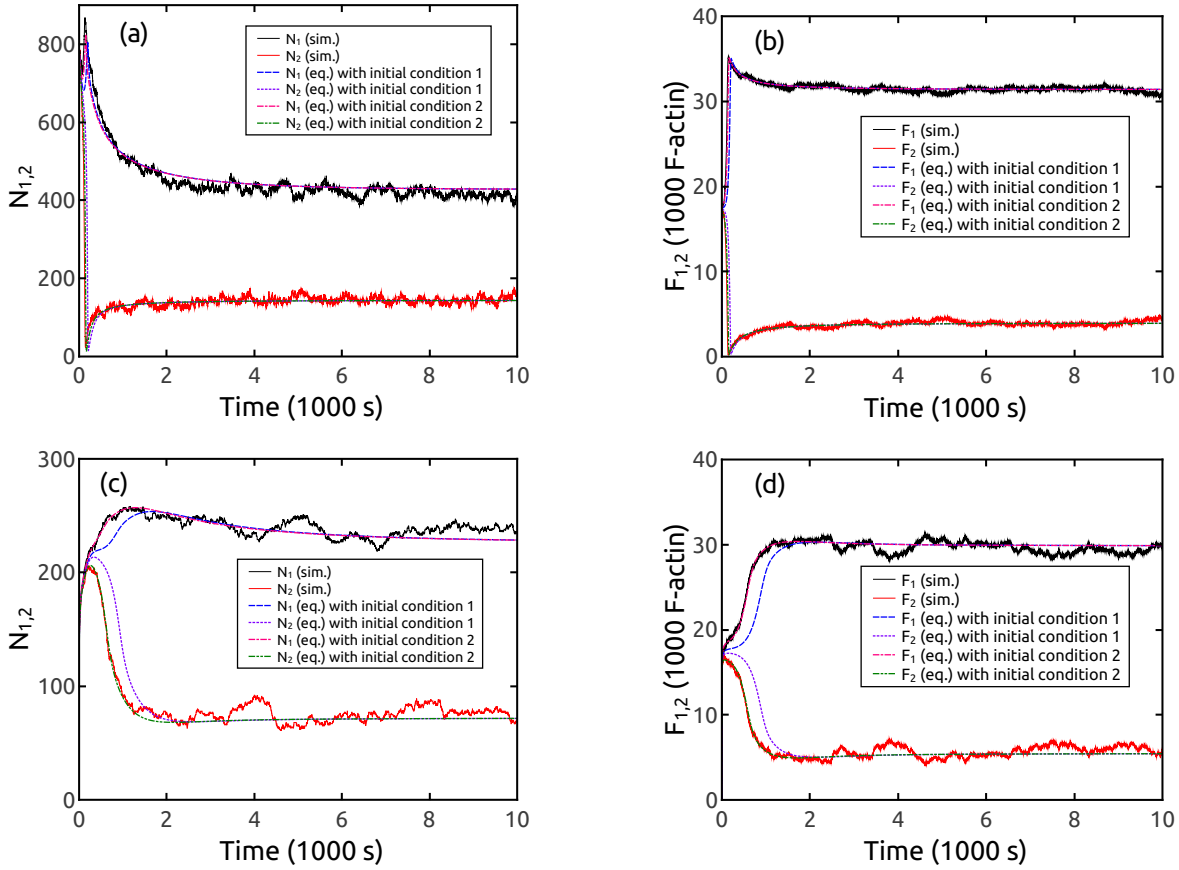

Figure 2.9: Approach to polarized steady state for $k_P^- = 1.5k_P^{-c}$ (see Table 2.2). Other parameters have the values given in Tables 2.1 and 2.2. Frames a) and b) are for small l_0, while frames c) and d) are for large l_0.

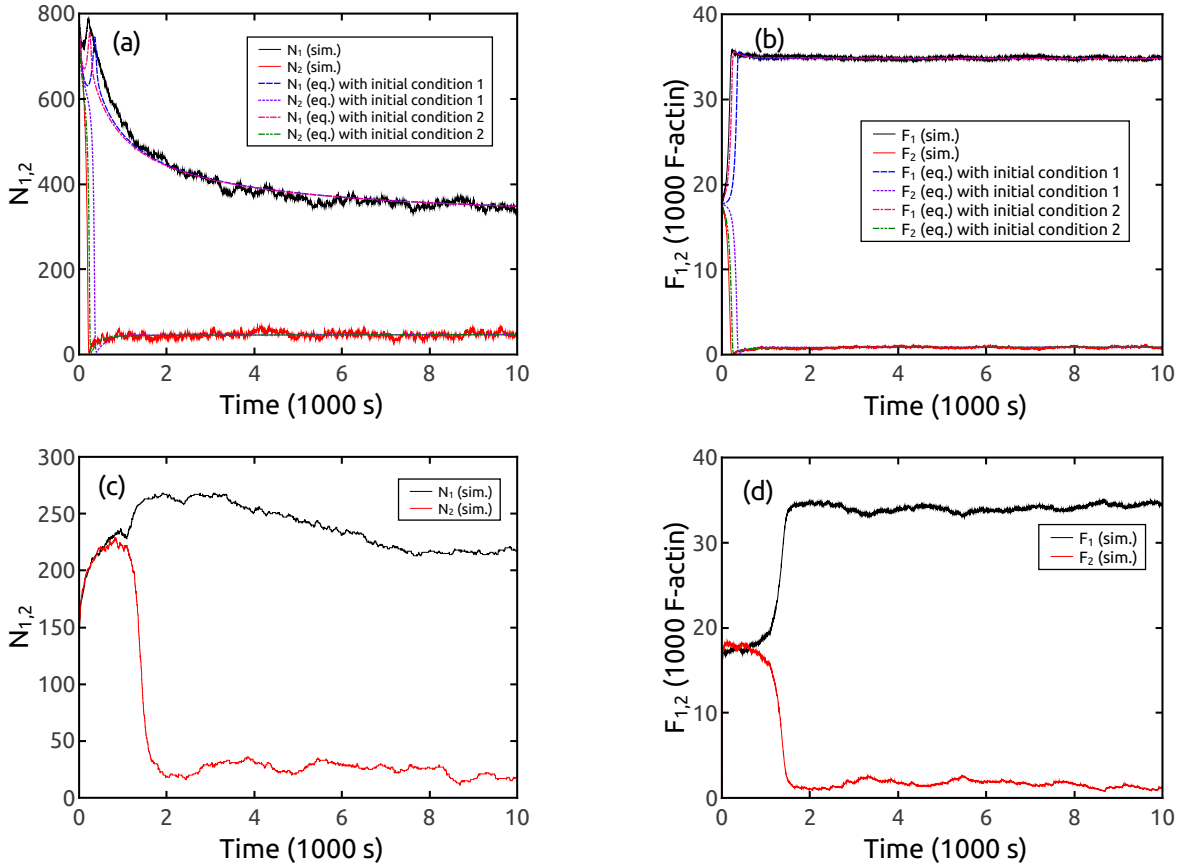

Figure 2.10: Approach to polarized steady state for $k_B^- = 0.5 k_B^{-c}$ (see Table 2.2). Other parameters have the values given in Tables 2.1 and 2.2. Frames a) and b) are for small l_0; frames c) and d) are for large l_0. We do not plot the rate-equation result for the large l_0 value, because in this case the average filament length in the rate equations becomes less than $0.5 l_0$ at one end of the cell, so Eq. 2.22 for the decay rate breaks down.

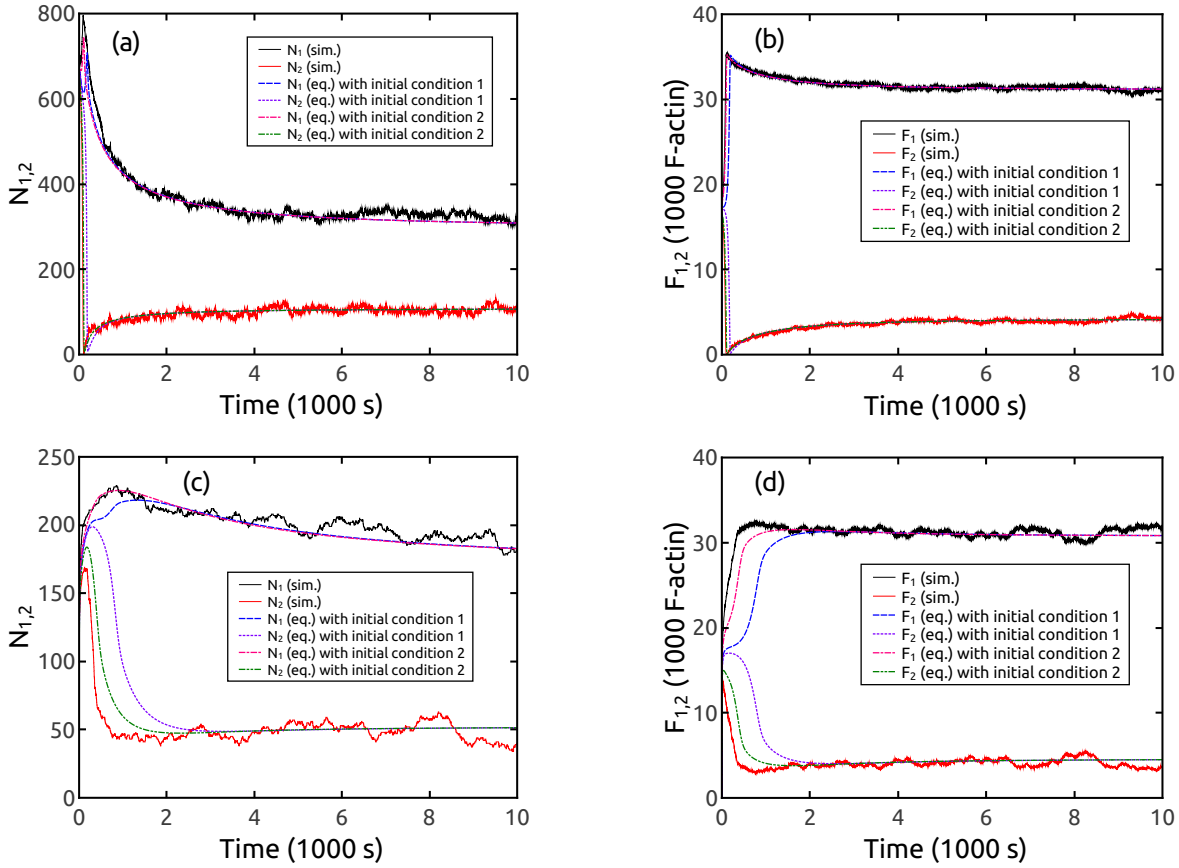

Figure 2.11: Approach to polarized steady state for $k_r = 0.5k_r^c$ (see Table 2.2). Other parameters have the values given in Tables 2.1 and 2.2. Frames a) and b) are for small l_0, while frames c) and d) are for large l_0.

2.9 Appendix B: Mathematical Derivations

Relation of polarization instability to the signs of the terms in $\hat{a}$ (Eq. 2.28) We note that the eigenvalues of $\hat{a}$ are determined [25] by the trace

$$\tau = \frac{\partial \Delta \dot{N}}{\partial \Delta N} + \frac{\partial \Delta \dot{F}}{\partial \Delta F} \tag{2.30}$$

and the determinant

$$\mathcal{D} = \frac{\partial \Delta \dot{N}}{\partial \Delta N}\frac{\partial \Delta \dot{F}}{\partial \Delta F} - \frac{\partial \Delta \dot{N}}{\partial \Delta F}\frac{\partial \Delta \dot{F}}{\partial \Delta N}, \tag{2.31}$$

as:

$$\lambda_{\pm} = \frac{\tau \pm \sqrt{\tau^2 - 4\mathcal{D}}}{2} \tag{2.32}$$

The fact that $\partial \Delta \dot{N}/\partial \Delta N < 0$ and $\partial \Delta \dot{F}/\partial \Delta F = 0$, as proved below and under **Discussion** respectively, imply that $\tau < 0$. Then Eq. (2.32) implies that $\hat{a}$ will have a positive eigenvalue, leading to instability, if and only if $\mathcal{D} < 0$, which occurs only if $\partial \Delta \dot{F}/\partial \Delta N > 0$, since $\partial \Delta \dot{N}/\partial \Delta N < 0$ and $\partial \Delta \dot{F}/\partial \Delta F = 0$.

Proof that $\partial \Delta \dot{N}/\partial \Delta N < 0$. This follows from inserting Eq. (2.22) into Eqs. (2.9) and (2.10). Differentiating Eq. (2.9) minus Eq. (2.10) with respect to ΔN gives

$$\frac{\partial \Delta \dot{N}}{\partial \Delta N} = -\frac{1}{2}\left(k_B^- + k_P^-\right)\frac{\partial}{\partial \Delta N}\left(k_1^d N_1 - k_2^d N_2\right). \tag{2.33}$$

Since $N_1 = N+\Delta N$ and $N_2 = N-\Delta N$, it is clear that $\partial N_1/\partial \Delta N > 0$ and $\partial N_2/\partial \Delta N < 0$. Also, when Eq. (2.22) is written in terms of N_1 and N_2,

$$\left.\frac{\partial \dot{k_1^d}\big|_{ss}}{\partial \Delta N}\right|_{\Delta N=0} = \frac{k_{on} G \beta T \delta}{2 l_0 N^2} e^{-\beta \frac{T\delta}{N}} \left(\frac{F_1}{N} - \frac{l_0}{2}\right)^{-1}$$
$$+\frac{F_1}{2l_0}\left(k_B^- + k_P^- + k_{on} G e^{-\beta \frac{T\delta}{N}}\right)\left(F_1 - \frac{l_0}{2}N\right)^{-2} > 0. \tag{2.34}$$

Similarly, $\partial \dot{k_2^d}\big|_{ss}/\partial \Delta N < 0$. Combining the above inequalities shows that $\partial \Delta \dot{N}/\partial \Delta N < 0$.

Chapter 3

ACTIN-REGULATOR FEEDBACK INTERACTIONS DURING ENDOCYTOSIS

3.1 Introduction

Endocytosis encompases a set of engulfment processes by which cells absorb molecules and materials from outside the cell [68]. The clathrin-mediated form of endocytosis (CME), in which membrane invaginations are surrounded by clathrin coats, is used by the cell for multiple purposes, including the regulation of plasma membrane activities and the ingestion of essential nutrients. In addition to its importance for cellular functions, CME provides an attractive system to study membrane deformation by actin and other cytoskeletal and membrane-associated proteins. Actin polymerization often plays an important role in CME. In yeast, CME requires actin polymerization [69, 70]. In mammalian cells, the role of actin polymerization depends on the physical conditions. When membrane tension is high, the requirement for actin polymerization is more stringent [71].

These findings motivate the study of actin polymerization dynamics during CME. Yeast is an attractive system for CME because of the ease of genetic manipulation, and the ability to perform live-cell imaging of fluorescent fusion proteins, expressed at endogenous levels. Actin polymerization and depolymerization during CME occur as part of the assembly and disassembly of a protein patch containing over sixty different proteins, arriving in a well

defined sequence [72, 10]. Initially cargo and adapter proteins assemble, followed by a coat including clathrin and other proteins. The coat recruits actin regulators, sometimes referred to as "nucleation promoting factors". The regulators, including Las17 (yeast WASP), Myo3, Myo5 (yeast class-1 myosins), and Pan1 (an Eps15-like protein) in budding yeast, recruit and activate the Arp2/3 complex to nucleate new actin filaments from the side of existing filaments. After actin polymerization begins, membrane bending occurs [18], and a tubule forms and it eventually pinches off into a vesicle, followed ultimately by dissolution of the protein coat.

Several studies have measured the effects of perturbations on the assembly of actin and its regulators in yeast. The actin inhibitor latrunculin [72] extended the lifetime of coat proteins, while the Arp2/3 inhibitor CK-666 [73] extended the actin lifetime and decreased the number of actin patches. Deletions of the gene encoding the endocytic coat protein Sla2 [29, 74] resulted in the formation of comet-shaped actin structures extending inwards from the cell cortex. We measured the effects of mutations affecting the budding yeast Arp2/3 regulators Las17, Myo3, Myo5, and Pan1, on the numbers of copies of actin and actin-binding proteins at the endocytic site [9]. These mutants had truncations of regulator acidic domains, which bind and activate Arp2/3 complex, so we expected less activation of Arp2/3 and decreased F-actin. However, the acidic-domain truncations did not significantly reduce the maximum F-actin count, and in some mutants it unexpectedly *increased*. A preliminary mathematical model suggested that a negative-feedback interaction between F-actin and the Arp2/3 regulators might contribute to this effect.

Two modeling studies in the literature have addressed the dynamics of F-actin in CME protein patches. One study, in budding yeast, treated a mechanism for protein pulse generation, based on indirect negative feedback interactions acting on the regulators, including the effects of membrane deformation and PIP2 hydrolysis [15]. This model explained several traits of endocytosis mutants. A second study, in fission yeast, treated a multistep model of actin filament nucleation, growth, and capping, based on an assumed time course for the active Arp2/3 regulator [16]. It provided important insights into the kinetics of cellular processes relative to those observed *in vitro*, and highlighted the role of severing in actin disassembly.

In this article, we seek to establish the main protein interactions that drive actin and regulator pulse dynamics in wild-type cells, and determine the effects of mutations and drug treatments on actin polymerization. To this end, we combine stochastic modeling studies of actin polymerization with a negative-feedback interaction between F-actin and the membrane. The model provides a more detailed treatment of the actin network than the models in the previous two studies [15, 16], because the network is explicitly grown in three dimensions. The effects of force on filament growth and branching are also included in a physically consistent fashion.

We find that our stochastic-growth/negative-feedback model explains key effects of the mutations and drug treatments discussed above. It also predicts an increase of regulator count under the conditions of reduced branching resulting from acidic-domain mutations of the regulators. This prediction is reinforced by results from a simple two-variable rate-

equation model of the regulator/actin dynamics. We test the prediction by measuring the regulator counts in mutated yeast cells using fluorescence microscopy, and the experiments confirm the prediction.

This chapter is based on an article published as Xinxin Wang, Brian J Galletta, John A Cooper, and Anders E Carlsson, "Actin-regulator feedback interactions during endocytosis", *Biophysical Journal*, 110(6): 1430-1443, 2016. The fluorescence videos were taken by Brian Galletta, while I performed the quantitative image analysis and the mathematical modeling.

3.2 Mathematical Models

The models treat the dynamics of actin polymerization and the regulator Las17, the yeast form of WASP (Wiskott-Aldrich Syndrome Protein). We focus on Las17 because *in vitro* experiments [14] suggest that it has the strongest nucleation activity. Furthermore, the other regulators with strong nucleation activity, class-1 myosins Myo3 and Myo5, have a motor activity that is beyond the present analysis. Treating Las17 by itself is certainly an approximation, but our data (**Fluorescence Imaging Experiments**) suggest that to some extent the regulators act independently of each other. We define L as the number of Las17 molecules in the endocytic protein patch.

The models extend our preliminary negative-feedback model [9]. They share the following main assumptions:

1. L grows by an autocatalytic self-assembly mechanism (see Box A of Fig. 3.1) from an initial fluctuation of magnitude L_0. In the absence of polymerized actin L approaches a plateau value at long times. Autocatalytic self-assembly would result from indirect or

direct attractive interactions between Las17 monomers. Such interactions have been demonstrated by *in vitro* experiments [75, 76] showing that WASP, in combination with adaptor proteins, self-assembles up to a certain limiting concentration.

We do not include actin-dependent terms in the assembly rate for two reasons: i) Las17 patches in budding and fission yeast assemble in the absence of polymerized actin [77, 29, 78, 79], and ii) Las17 assembles for a period of about 20 seconds before actin arrives at the patch. In fission yeast, treatment with latrunculin [78], which inhibits actin polymerization, and mutation of cofilin [79], which severs actin filaments, slow the accumulation of Wsp1. This suggests feedback of F-actin onto Wsp1 assembly. We are not aware of such an effect in budding yeast; furthermore, the rapid assembly of Wsp1 compared to Las17 suggests that the underlying biophysical mechanisms may be quite different. This is consistent with the large evolutionary distance between the organisms.

2. The disassembly of regulators is accelerated by actin polymerization, leading to a negative feedback effect. Negative feedback between actin and Arp2/3 regulators is suggested by several observations. First, the regulator time courses during endocytosis have the form of a pulse, and this pulse lifetime is extended by latrunculin, which inhibits actin polymerization [29, 80]. Second, in mammalian cells, latrunculin slows the membrane dynamics of WAVE complex, another Arp2/3 regulator [81, 82]. Finally, traveling waves of F-actin along the plasma membrane have been observed in several cell types, and theoretical models have found it necessary to assume negative feedback

effects to explain these phenomena (see Ref. [66] for a review). Without a negative-feedback term, none of our models are able to obtain the pulse behavior of the proteins. A similar negative-feedback effect between polymerized actin and coat proteins has been suggested previously [79, 15].

At least three physical mechanisms could mediate this negative-feedback effect (see Boxes B1-B3 in Fig. 3.1):

i) (Box B1) Newly nucleated filaments pull Las17 off the membrane, after which Las17 diffuses into the cytoplasm. The actin filament network moves away from the membrane, so this process could result from the binding of Las17 to Arp2/3 complex in the actin network, or to the actin network itself. The WH2 domain of the actin regulator N-WASP binds to actin [83]. Since Las17 also has a WH2 domain, it could bind F-actin.

We note that in Arp2/3 branching studies using a di-VCA WASP fragment, most di-VCA molecules detached from the mother filament before the new branch was generated [20]. If Las17 detaches in a similar fashion, the newly nucleated filament will not pull Las17 with it. However, the resolution of the experiment was such that the number of di-VCA molecules staying on filaments (Figure 2D of Ref. [20]) could be up to 40% of the number of filaments forming. Our stochastic model, which assumes that 10% of branching events cause Las17 detachments, is thus consistent with Ref. [20]. Furthermore, Las17 has a polyproline actin-binding domain [84] that is not present in di-VCA. This domain might allow new actin branches to drag Las17 off the membrane.

ii) (Box B2) Curvature or tension of the membrane, generated by actin polymerization, weakens the binding of Las17 or the underlying coat proteins to the membrane [15]. This mechanism is supported by studies revealing tension-dependent binding of clathrin [85] and the WASP-binding protein FBP17 [86] to membranes, and the curvature-dependent binding of the regulator WASP to vesicles [87].

iii) (Box B3) Membrane curvature, or proteins recruited by polymerized actin, hydrolyze PIP2, which in turn weakens the binding of the coat proteins and regulators to the membrane [15]. This hypothesis is supported by the finding that recruitment to actin patches of the synaptojanin Sjl2, which hydrolyzes PIP2 [88], is dependent on F-actin [89]. Furthermore, PIP2 hydrolysis depends on membrane curvature [90].

3. Actin filament nucleation is autocatalytic, so that preexisting actin filaments accelerate polymerization (see Box C in Fig. 3.1). This assumption is based on the branching nature of Arp2/3-induced actin filament nucleation, where Arp2/3 nucleates new filaments by binding to the sides of existing filaments [48, 8]. The applicability of a model treating spontaneous (non-branching) nucleation is discussed in the Appendix.

To enhance the robustness of our results, we perform two types of model calculations, stochastic-growth and rate-equation. The stochastic-growth calculations generate an explicit actin network in three dimensions. This network interacts with the actin regulators at the cell membrane, and its growth is slowed by opposing force. The rate-equation models capture the key features of the stochastic-growth calculations in a compact form.

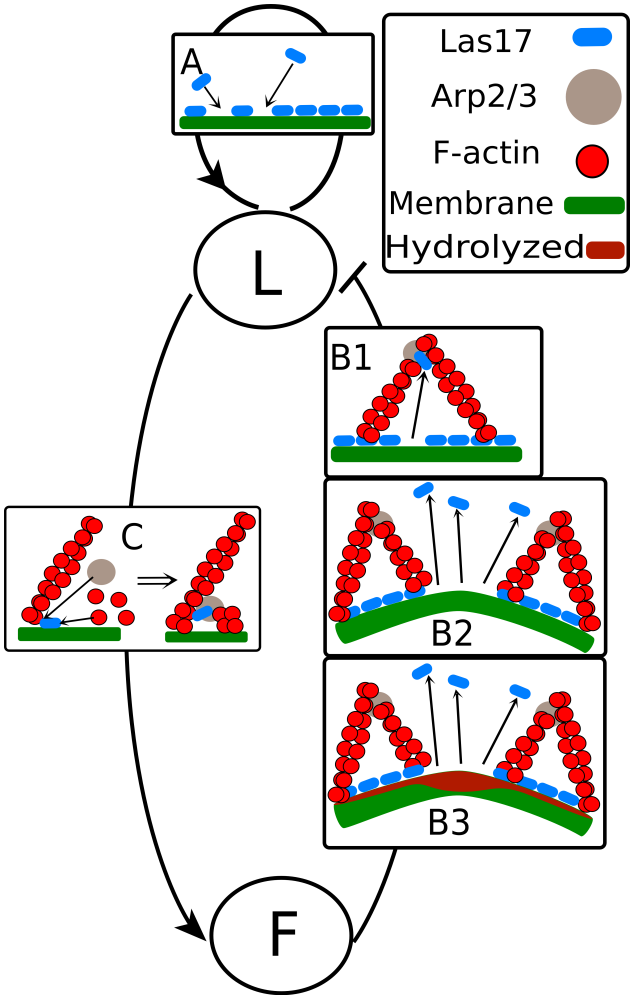

Figure 3.1: Schematic of modeled protein interactions. L is Las17 and F is F-actin. Blue ovals: Las17. Gray circles: Arp2/3 complex. Red circles: actin monomers. Membrane is green and region where PIP2 is hydrolyzed is dark red. Box A shows the self-recruitment of Las17. Boxes B1-B3 show possible mechanisms for the negative feedback of F-actin on Las17. Box C shows how Las17, Arp2/3 complex, and actin monomers enter the branching mechanism.

Stochastic-Growth Model

This model is similar to the model used by one of us to study F-actin waves in animal cells [91], and it shares general features with several other models of actin waves [81, 92, 93, 94].

It uses a Monte Carlo-type network-growth methodology as in Ref. [22]. Polymerization, branching, capping, and network disassembly are treated as stochastic events described by rate parameters k_{on}, k_{br}, k_{cap}, and k_{sev}. The network is assumed to be rigid, and it moves away from the membrane at a rate determined by the polymerization rate of the filaments in contact with the membrane. Network disassembly is assumed to occur by the disappearance of entire filaments, one at a time. We neglect the possibility of reattachment of filaments to the network. Previous work [16] has shown that actin dynamics in fission yeast is well described without including reattachment. Details are given in the Appendix.

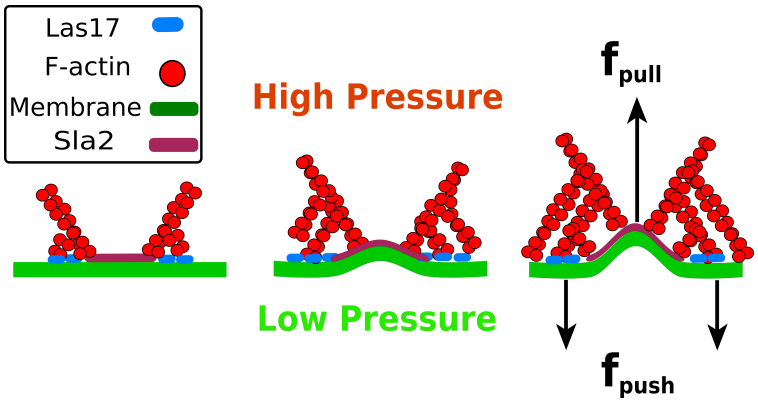

Figure 3.2: Schematic of the 3d geometry of the stochastic-growth model. Actin filaments polymerizing from a ring of Las17 push against the membrane, pulling other filaments attached to Sla2 at the membrane back with them. The osmotic pressure is higher in the interior (up), and the force of actin polymerization helps overcome this pressure difference. The turgor pressure is the difference between the interior and exterior osmotic pressures.

The geometry of the model and the forces (Fig. 3.2) is based on the explicit mechanical calculations of Ref. [95], and on theories [96, 97, 69] in which retrograde flow of actin drives invagination by pulling the region inwards. The regulators are uniformly distributed on the membrane on a ring with inner radius 25 nm and outer radius 75 nm (Fig. 3.3),

corresponding roughly to the radii of the invagination and the actin polymerization zone found in Ref. [18]. The assumed distribution is consistent with observed rings of the protein Sla1 [10], F-actin rings during CME in COS-7 cells [33], and with experimental observations of membrane localization of Las17 [29, 10, 98]. (We note, however, that a small ($<$ 100 nm) small inward motion of Las17 has been suggested [10].) We assume that the regulators redistribute rapidly in the Las17 region. This is plausible since the turnover times for the regulator N-WASP on viruses [99] and clathrin in mammalian cells [34] are only about 2 s [99]. Therefore we treat a uniform distribution of Las17 molecules rather than specifying individual coordinates. We base our description of regulator assembly on a simple reaction-rate theory. If the Las17 assembles by interaction of a molecule in solution with a pair of molecules bound to the membrane, and the concentration in solution is regarded as constant on the assumption that diffusion is rapid, then the assembly rate will be proportional to L^2 [100]. If the reaction occurs in a fixed region where each Las17 molecule takes up a certain area, the number of sites available for reaction will be reduced by a factor proportional to $L_2 - L$, where L_2 is the maximum number of molecules that can fit. Combining these dependences, we obtain an assembly rate proportional to $L^2(L_2 - L)$, and we use this in the bulk of the calculations. Interactions of different orders correspond to different powers in this expression. We have found that assembly rates proportional to $L(L_2 - L)$ and $L^3(L_2 - L)$ preserve the basic predictions of the model. However, an assembly rate proportional to $(L_2 - L)$, which does not contain an autocatalytic term, gives poor results for both wild-type and mutant cells (see Appendix). We thus use an average rate of $k_0 L^2 (L_2 - L)$, where k_0 is

a rate parameter. The process is treated stochastically.

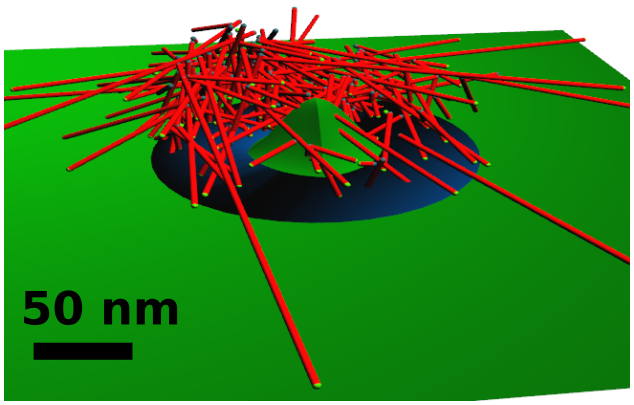

Figure 3.3: Oblique snapshot of the stochastic simulation geometry, after 23 s of a wild-type simulation run. Actin filaments are red cylinders, with barbed ends in light green spheres; the membrane is green. The blue disk around the center represents the Las17 region where actin filament branches form. The membrane profile is not explicitly treated by the model but we include an approximation to it to clarify the physical picture. We assumed that the membrane deformation at the center is the average distance from the actin filament pointed ends to the membrane, provided that the number of filaments and the F-actin count exceed the threshold value for force generation (see text). The width of the deformation corresponds roughly to known invagination widths [18].

The polymerization rate is $k_{on}G$, where G is the free-actin concentration, and the branching rate per subunit is $k_{br}L$. Branching is assumed to occur only in a "donut"-shaped region above the regulator ring, within a branching width $W = 20$ subunits $= 54\ nm$ of the membrane. We implement the negative feedback of F-actin on Las17 by assuming that a Las17 molecule can leave the membrane (and become inactive), with probability α, when a branching nucleation event occurs. This corresponds to mechanism B1 in Fig. 3.1. The Las17 molecules are assumed to detach from the actin network when they leave the membrane, since Las17 moves inward much less than the actin network [29, 10].

The main model does not treat membrane deformation explicitly, for reasons of computational practicality. We still feel that the results are meaningful, because the main actin regulators remain near the membrane during invagination [29, 10, 98]. In the Appendix we describe a model in which regulator detachment is driven by membrane deformation rather than by branching dynamics, corresponding to mechanisms B2 and B3 in Fig. 3.1. We were unable to obtain physically reasonable results with this model.

We treat the forces opposing actin network growth in a simplified fashion (Fig. 3.2). Because the viscous drag on the actin network is extremely small, we assume a balance of forces on the network leading to zero net force. In the outer region of the network, defined by the Las17 ring, the filaments push against the membrane, and thus experience a force opposing their growth. The inner region of the network pulls on the membrane via linker proteins such as Sla2. The magnitude of the pushing force opposing actin polymerization in the ring is equal to the magnitude of the pulling force.

The dominant opposing force that must be overcome in the pulling region likely results from turgor pressure [95, 101]. Estimates of the turgor pressure in budding yeast vary widely, from 0.05 MPa [102] to roughly 0.6 MPa [103]; in fission yeast a higher value of 0.85 MPa has been measured [104]. If one assumes a radius of 25 nm [18] for the pulling region, the total estimated force for budding yeast then ranges from 100 pN to 1200 pN. We define f_a as the portion of the total force that needs to be overcome by actin polymerization, and we assume that the remaining force is supplied by curvature-generating proteins such as clathrin and BAR-domain proteins. The value of f_a is highly uncertain. We used that a value of

415 pN, about a third of the highest value of the total force. The results were insensitive to the value of f_a (see Appendix).

We treat the slowing of actin polymerization by f_a by assuming that a critical minimum number of filaments and subunits (taken to be 20 and 200 respectively) is required to form a continuous network that can exert a pulling force on the membrane. When these critical numbers are not reached, there is no opposing force. When the critical numbers are reached, then the network experiences the force f_a. We take the on-rate for the free filaments touching the membrane to have the familiar "Brownian-ratchet" form [21]

$$k_{on}^{touch} = k_{on} exp(-f_a \delta / N_{touch} k_B T). \tag{3.1}$$

where N_{touch} is defined as the number of filaments with two subunits of the membrane. In principle, the on-rate in Eq. 3.1 should include cosine factors depending on the filament orientation. We found that the inclusion of such factors gives results similar to lowering f_a, so we decided to use the simpler form of Eq. 3.1. The retrograde velocity of the actin network is then given by $k_{on}^{touch} \delta \langle cos\theta \rangle$, where $\delta = 2.7\ nm$ is the length added per subunit, θ is the orientation angle of a filament, and the average is taken over the touching filaments.

We parameterize the model for budding yeast. The model's potential relevance to fission yeast is described in the **Discussion**. The key parameters in the model are $k_{on}G$, k_{br}, k_{cap}, k_{sev}, k_0, and α, whose values and definitions are given in Table 1. Because error minimization with the stochastic-growth code is computationally demanding, we obtained an initial parameter set using a faster four-variable rate-equation code (see Appendix), and performed

Model	Stochastic	Rate-Equation
Parameters		
$k_{on}G$, barbed-end on-rate (s^{-1})	32	-
k_{br}, subunit branching rate ($10^{-3}s^{-1}$)	2.17	0.957
k_{cap}, capping rate (s^{-1})	0.667	-
k_{sev}, severing rate (s^{-1})	0.300	0.427
W, branching layer thickness (nm)	54	-
f_a, total actin-membrane force (pN)	415	-
k_0, Las17 assembly rate constant ($10^{-5}s^{-1}$)	3.5	3.93
α, Las17 detachment probability	0.100	0.136
$\bar{l}$, average filament length in subunits	-	30
L_2, maximum Las17 count	101	101
k_{nuc}, filament nucleation rate ($10^{-2}s^{-1}$)	2	-
Initial Values		
L_0, Las17 count	20	18
N_0, number of filaments	5	-
F_0, F-actin count	100	1

Table 3.1: Parameters and initial values for stochastic and rate-equation models.

further optimization using the stochastic code. The optimization with the stochastic code was accelerated by the use of a Graphical Processing Unit together with the CUDA programming language [105]. To avoid overfitting, we do not vary all of these parameters, but rather assign a k_{cap} a fixed value, from the four-variable model. The remaining five parameters $k_{on}G$, k_{br}, k_{sev}, k_0, and α, were obtained by a least-squares fit to the following six properties of the time courses: the peak heights of L and F, the full widths at half-maximum of the time courses of L and F, and the peak counts of capping protein and Arp2/3 complex taken from our previous work [9] . Note that the fitted value of α is small, suggesting that most Las17 molecules remain on the membrane during branching events.

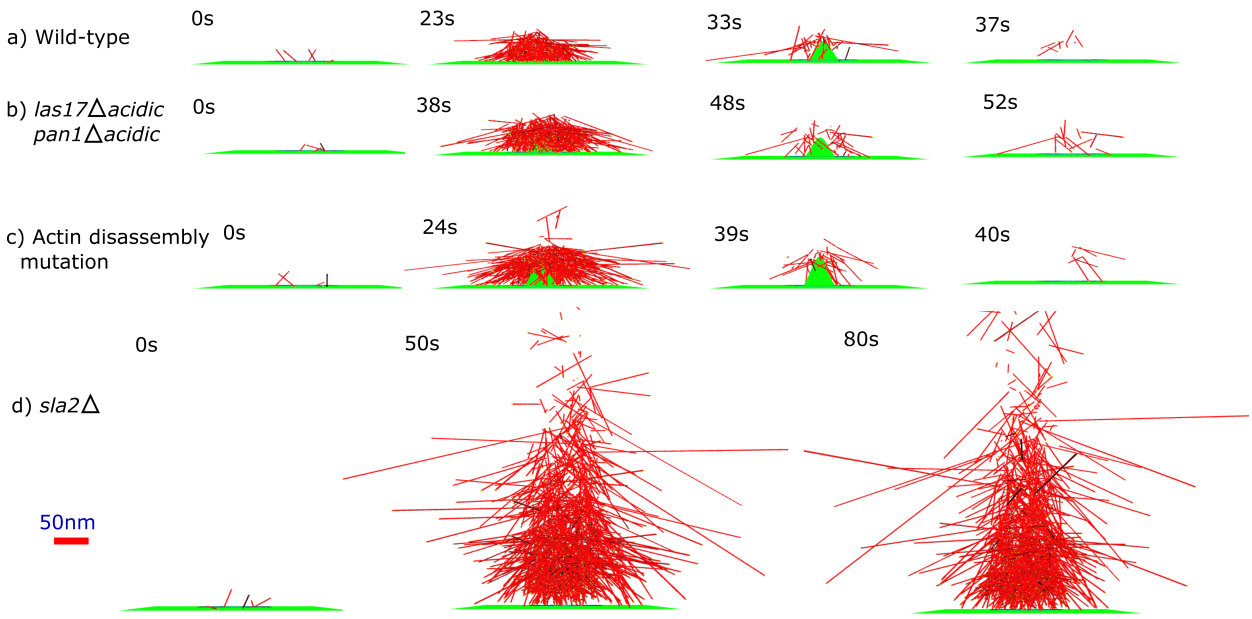

Figure 3.4: Side view snapshots of stochastic simulations for different interventions. Color conventions are as in Fig. 3.3. Each of rows a)-c) shows the initiation of the simulation, the F-actin peak, disassembly, and near disappearance. Row d) shows the initial phase and later time points where the F-actin count reaches a steady state. The membrane profile is approximated as in Fig. 3.3, except that in row d) we assumed that the actin gel was unable to pull on the membrane.

The simulation begins with 5 primer actin filaments [106] placed with random positions and orientations in the Las17 disk, and a starting value of $L_0 = 20$ Las17 molecules. L_0 was chosen with two considerations in mind: i) the critical nucleus is probably relatively large, to prevent very rapid nucleation of patches, and ii) L_0 should be much smaller than L_2. Primer filaments are also produced at a low continuing rate of 0.02 s^{-1}. The simulations were run 2000 times for each parameter set to obtain meaningful averages. Because several of the parameters and functional dependences are uncertain, we varied parameters and assumptions to see the effects on the model predictions (see Appendix).

The actin patch life cycle illustrated in the representative snapshots of Fig. 3.4a has the following three steps: initiation from primer filaments, rapid polymerization via branching nucleation, and finally depolymerization as regulators are removed and inactivated. Fig. 3.5a compares the predicted wild-type time courses with our experimental data (more complete data is given under **Fluorescence Imaging Experiments**). The predicted time courses are similar to the experimental ones, and also to previously published ones [14, 10]. Since we do not have a direct measurement of the F-actin count, we estimate the measured F in this and following figures as 8.9 times the measured Abp1 count. This results from assuming a value of 6000 for the wild-type peak value of F [8]; dividing this by our measured peak wild-type value of 674 (see **Fluorescence Imaging Experiments**) for Abp1 gives the factor of 8.9. Because we did not perform two-color experiments, we could not measure the delay between the Las17 peak and the actin polymerization peak. Therefore in presenting our data and corresponding model results, we do not show the delay, but rather align all of the time courses at their maxima. The delay in our model results is a few seconds, consistent with previous results using two-color imaging [14, 10]. Because several of the processes treated in the model are stochastic, a substantial degree of asymmetry is often seen in the actin patches (see Fig. 3.3), reminiscent of the asymmetry seen in electron micrographs of CME in mammalian cells [107].

Modeling effects of mutations and drug treatments on cells. To further explore the relevance of this model to the experimental system, we have studied four interventions *in silico*, whose effects on cells have been measured *in vivo*:

Mutations of the acidic Arp2/3-binding regions of Las17. The acidic "A" regions of the regulators are believed to be important for nucleation because they bind Arp2/3 complex. *In vitro* studies [108] have also shown that these domains, as well as the combination of these domains with WH2 domains, called "WA", can activate Arp2/3 complex. We thus model the A-region mutations by reducing k_{br}. We do not know how large the reduction is. *In vitro* data [109] for WASP suggest that the A region mutation renders Las17 completely inactive ($k_{br} = 0$). However, our previous observation [9] of a substantial F-actin count even in cells containing A-region mutations of the three nucleators believed to be the strongest, Las17, Myo3, and Myo5, suggests that k_{br} is not driven to zero by these mutations. A nonzero value of k_{br} could be caused by i) intrinsic activity of Arp2/3 complex (requiring recruitment but not activation) [110], ii) branching activity of other nucleators, or iii) nucleation activity of Las17 not requiring the A region [8].

In the absence of a negative-feedback interaction, acidic-domain mutations would cause a large reduction in the F-actin peak count F_{max}, roughly proportional to the reduction in k_{br}. Our simulations including negative feedback show a qualitatively different behavior. When k_{br} is reduced by fractions up to 70%, F_{max} increases rather than dropping proportionally to k_{br}. When k_{br} is reduced by more than 70%, F_{max} is reduced, and F_{max} equals the initial F value when $k_{br} = 0$. Figs. 3.4b and 3.5a show model results for a 40% reduction in k_{br}, along with the corresponding experimental data. The simulations predict a 40% increase in F_{max}, consistent with the data, and our previous experimental findings [9] for cells with single acidic-domain mutations of Las17 and cells with acidic-domain mutations of both Las17 and

Pan1. The magnitude of the predicted effect, for this value of k_{br}, is comparable to the measured one for the double mutant, and we label the figure frames accordingly.

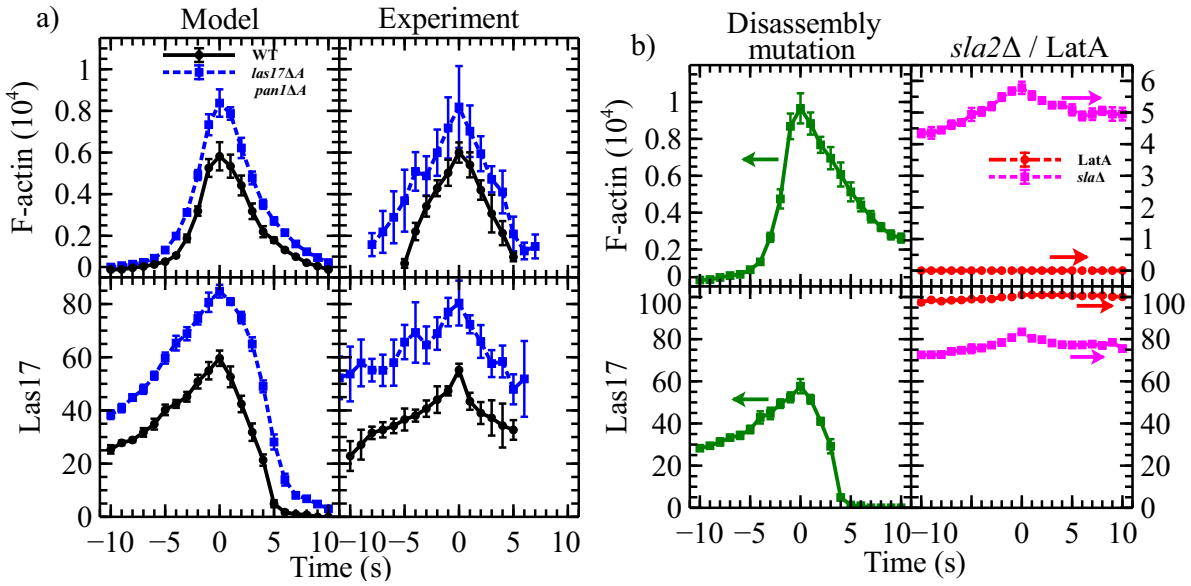

Figure 3.5: Time courses of L and F from stochastic simulations and experiments (described in detail under **Fluorescence Imaging Experiments**). a) Wild type and *las17*Δ*acidic pan1*Δ*acidic* mutant, b) disassembly mutant, c) *sla*2Δ mutant, and d) LatA treated cells. F-actin count is measured Abp1 count multiplied by a conversion factor of 8.9 (see text). Model results obtained from 2000 simulation runs, displayed in the same way as the experimental data (see Appendix): Plotted points correspond to mode values; error bars are the standard deviation of a distribution of 1000 mode values obtained by bootstrapping. The time courses in this and subsequent figures are aligned with their peaks at time t=0. Arrows in frame (b) indicate which vertical scale to read.

The simulations also predict an increase in the peak Las17 count L_{max}, of about 40%, which is confirmed by our data (Fig. 3.5a). The increase occurs in the model because the reduced branching rate leads to less Las17 being pulled off the membrane. The increase in L_{max} in turn causes the increase in F_{max}, which is determined by a competition between the increased amount of Las17 present and the reduced k_{br}. The prediction of increased L_{max} is

very robust: L_{max} always increases when k_{br} is decreased, and the increase is a monotonic function of k_{br}.

Disassembly mutations. We model mutations that slow actin disassembly by reducing k_{sev}. Actin disassembly is believed to be delayed relative to actin assembly because it follows hydrolysis of ATP on F-actin. This belief is supported by the observations that assembly of cofilin, which accelerates actin disassembly, is delayed relative to F-actin [111, 79]. Therefore, we model actin disassembly mutations as a decrease in k_{sev} that occurs after a delay. For computational convenience, the delay is described in terms of a minimum number of filaments (100) that must be reached before k_{sev} is decreased. Actin disassembly mutants that have been studied in budding yeast include the actin *act1-159* mutation [112], which delays disassembly because a conformational change is prevented, and the *cof1-22* cofilin mutation [113, 114, 111]. We do not know how large the reduction in k_{sev} is for a given mutation, and we show results for a reduction of 50% in Figs. 3.4c and 3.5b. The model predicts that F_{max} is increased by about 60%, the F-actin lifetime is greatly increased, and the regulator count is decreased by cofilin mutation. The predictions for F-actin are qualitatively consistent with the findings that actin patches in budding yeast are 25% brighter in *act1-159* mutant cells [112], and that their disassembly is delayed in both the *act1-159* and *cof1-22* mutants [113, 114, 111].

sla2 deletion. Sla2 couples actin polymerization to membrane deformation [115]. Reduction of this coupling by *sla2* deletion should have two effects. First, it should reduce the force opposing actin polymerization. Second, it should lead to less deformation and tension

in the membrane. As discussed above (mechanisms B2 and B3 in Fig. 3.1) regulator detachment may be accelerated by tension, Therefore *sla2* deletion could reduce detachment of regulators from the membrane, leading to a reduction in α. We reduce f_a by 90% (a nonzero force is needed to keep the actin gel near the membrane), and reduce α by varying amounts. Reductions less than 30% give actin pulses. Reductions greater than 30% cause persistent and increased actin accumulation (see Figs. 3.4d and 3.5b for a reduction of 90%). This reproduces the finding of persistent comet-shaped accumulations of actin in the *sla2* mutant [29, 74]. The fact that the reduction in α is needed to reproduce the actin comets suggests that the negative-feedback interaction is tension dependent.

Latrunculin treatment. We model latrunculin treatment by setting $k_{on} = k_{br} = 0$, which equates to no actin polymerization. The regulator time course in Fig. 3.5b shows that the regulator count goes to its maximal value and remains there. This is consistent with the observation that latrunculin greatly lengthens the lifetime of coat proteins and regulators [29].

Rate-Equation Models

Mathematical Form. The rate-equation models abstract the essential ingredients of the more complex simulations, allow us to ascertain the robustness of the predictions, and facilitate more complete fitting of the models to the data. They treat the variables F (F-actin) and L (regulator Las17). For simplicity, we treat actin polymerization as a one-step process where a nucleator produces an actin filament that grows instantaneously to its final length. This approximation will be valid if the time it takes to grow a filament is shorter than

the time scale of the endocytic dynamics. To estimate the filament growth time, we note that the free actin concentration is at the micromolar level [8]. Assuming a value of $2\mu M$, and taking the actin polymerization rate to be 11.6 subunits $s^{-1}\mu M^{-1}$ [59], we find that a typical actin filament of $\sim$40 subunits [8] takes about two seconds to grow to its final length. By comparison, the actin lifetime in the patch is about 10s. Therefore, regarding filament growth as instantaneous appears to be a reasonably good approximation. We have confirmed this by studying a four-variable model in which filament nucleation and growth are treated separately (see Appendix). We find that the two-variable and four-variable models agree well, provided that the detachment rate parameter α in the four-variable model is reduced by about 10% relative to the two-variable model.

We implement our assumptions as follows:

$$\frac{dL}{dt} = k_0 L^2 (L_2 - L) - \alpha k_{br} L F, \tag{3.2}$$

$$\frac{dF}{dt} = k_{br} \bar{l} L F - k_{sev} F, \tag{3.3}$$

where k_{br} is the branching rate per subunit, $\bar{l}$ is the average filament length, α is the detachment probability for L per branching event, and k_{sev} is the disassembly rate of F. The first term in dL/dt is the same as the average assembly rate in the stochastic simulations. In this model the number of filaments N is $F/\bar{l}$. The second term is a nucleation rate of $k_{br}LF$, corresponding to autocatalytic branching. The first term in dF/dt combines the nucleation rate of $k_{br}LF$ with our assumption that filaments grow rapidly to length $\bar{l}$. Finally, the last term describes a simple first-order decay of F.

This model is similar to the classic Fitzhugh-Nagumo (FN) model [3, 26], in that it has a nonlinear positive-feedback term driving assembly of the activator L, and an inhibitor F whose buildup drives the activator down (to be precise $-F$ corresponds to the inhibitor in the FN model). However, the mathematical forms differ in three ways: i) The buildup at small L is quadratic in L rather than linear as in the FN model, to reproduce the slow initial buildup of L [14, 10]; ii) the second term in dL/dt contains an added factor of L to prevent L from going negative; and iii) the first term of dF/dt contains an extra factor of F to account for autocatalytic branching.

Fitting and Predictions of Two-Variable Model. The four adjustable parameters (k_0, k_{pol}, k_{sev} and α) are optimized to fit data for wildtype cells, while $\bar{l}$ was given a plausible value of 30 (any change in $\bar{l}$ could be compensated by making appropriate changes in α and k_{br}). We use a least squares objective function to minimize the difference between the time courses given by the model and those obtained from experiment (see Appendix). L_2 is chosen to be the same as in the stochastic simulations. We choose $F = 1$ at the beginning of the simulation, as a starting point for autocatalytic growth. We find that our results are not sensitive to the value of L_0, and as in the stochastic simulations we used a value that is much smaller than L_2, but guarantees a large critical nucleus. The fit parameters are given in Table 1. Note that k_{br} is smaller than in the stochastic simulations because in this model all subunits are implicitly allowed to branch, while in the stochastic simulations only those near the membrane can branch. As seen in Fig. 3.6, the model matches the data reasonably well. The peak heights and full widths at half maximum of both F and L are reproduced

Phenotype	F_{max}	L_{max}
Wild-type	6133	50
las17Δ*acidic pan1*Δ*acidic*	9602	84
Actin disassembly mutation	8549	50
latrunculin treatment	0	101

Table 3.2: Summary of predictions of rate-equation model.

well, as well as the slow buildup of L.

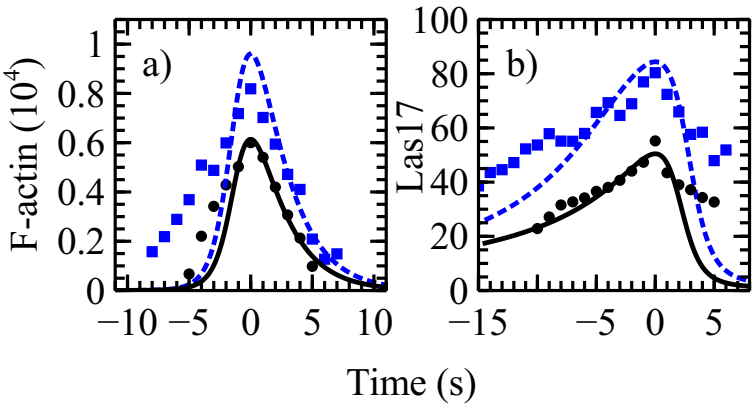

Figure 3.6: Rate-equation model with branching nucleation. Predicted time courses (solid and dashed lines) of a) F and b) L for wild-type (black) and *las17*Δ*acidic pan1*Δ*acidic* (blue) cells compared with experimental time courses (dots). F is the measured Abp1 count multiplied by a conversion factor of 8.9 (see text). For clarity, the error bars for the experimental data are not indicated here, but they are given in Fig. 3.5a.

We have predicted the effects of the same interventions, except for the *sla2* mutation, treated above by the stochastic-growth models. We used the same percent changes in the parameter values. We were unable to model the *sla2* deletion mutation in a physically reasonable fashion because the rate-equation model does not include opposing force.

The results (Fig. 3.6 and Table 2) are generally similar to the stochastic-growth model

predictions. Under acidic-domain and actin disassembly mutations, both F_{max} and L_{max} increase substantially. Under latrunculin treatment, $F_{max} = 0$ but L climbs to an asymptotic value of L_2.

These results are fairly insensitive to the values of the unknown parameters L_0 and L_2. Reducing L_0 by 50% has no effect on the quality of fit in the wild-type case; increasing it by 50% increases the root-mean-square (rms) error by 10%. The sign of the phenotypic predictions made above is preserved, although their magnitude changes. Doubling L_2 increases the rms error of fit by 30%, but again leaves the qualitative predictions of the model unchanged.

3.3 Fluorescence Imaging Experiments

To test the predictions of the theoretical models, we measured the effects of acidic-domain mutations on the regulator counts. We extended our previous measurements of Abp1, capping protein and Arp2/3 complex [9] to measure the counts of the four regulators Las17, Pan1, Myo3, and Myo5 in wild type cells and the following mutants: *las17*Δ*acidic*; *pan1*Δ*acidic*; *myo5*Δ*acidic*; *myo3*Δ*acidic myo5*Δ*acidic*; *las17*Δ*acidic pan1*Δ*acidic*; and *myo3*Δ*acidic myo5*Δ*acidic pan1*Δ*acidic*. We also reanalyzed our Abp1 data [9], which had previously been analyzed using different software. These measurements allow us to test our predictions of the effects of mutations on regulator counts, and provide a database for fitting the models. Our measurements of the cross-effects of mutation of one regulator on assembly of another regulator also allow us to ascertain the effects of interactions between regulators on their assembly. Our methods for generating yeast strains, as well as the microscopy and image analysis, are similar to those in Ref. [9]. We give more information about these methods,

and the protein counting methods, in the Appendix.

The data are given in Fig. 3.7. The time courses are aligned with each one having its maximum at time $t = 0$. They are truncated in time because the fractional error at smaller protein counts becomes large. The time courses of Abp1, Las17, and Myo5 reproduce the general features of those given in Ref. [14] and [10], including the slow buildup of Las17. Our wild-type peak values for Las17 and Myo5 (55 and 130), are similar to the values (43 and 130) measured for budding yeast in Ref. [10]. They are, however, much smaller than the counts of the corresponding proteins Wsp1 and Myo1 (230 and 400) measured for fission yeast actin patches in Ref. [13].

Abp1 Count Depends Counterintuitively upon Acidic-Domain Mutations. Fig. 3.7(b) shows time courses of Abp1, our F-actin surrogate, in wild type and various Δ*acidic* mutants. The results are reasonably consistent with our previous ones [9], with the wild-type count being about 15% below the previous count and that for the *las17*Δ*acidic pan1*Δ*acidic* mutant being about 30% lower. The Abp1 counts in the *las17*Δ*acidic pan1*Δ*acidic* and *las17*Δ*acidic* mutants are larger than in the wild type cells, by 37% and 20% respectively, an effect similar to that found in our previous work. This is consistent with the predictions of both the stochastic (Fig. 3.5a) and rate-equation (Fig. 3.6a) models. On the other hand, the Abp1 count in the *myo3*Δ*acidic myo5*Δ*acidic pan1*Δ*acidic* and *myo3*Δ*acidic myo5*Δ*acidic* mutants is nearly equal to that in wild type cells. The Δ*acidic* mutants that include the *pan1*Δ*acidic* mutation affect the Abp1 count more than those without the Pan1 mutation, but *pan1*Δ*acidic* itself has an almost negligible effect.

Acidic-Domain Mutation of Las17 Increases Las17 Count. Fig. 3.7(c) shows that the Las17 count increases as a result of *las17*Δ*acidic* mutation. This is consistent with the predictions of both of the mathematical models (Figs. 3.5a and 3.6b). The peak height is increased by 55% in the *las17*Δ*acidic* mutant, and 60% in the *las17*Δ*acidic pan1*Δ*acidic* mutant. Thus the effect of the additional Pan1 mutation is small. The Las17 lifetime is increased in both these mutants. On the other hand, the Las17 count is essentially unaffected by mutations of Myo3 and Myo5, even when they are combined with mutations of Pan1.

Acidic-Domain Mutation of Myo5 Increases Myo5 Count. For Myo5, the largest effect is seen in the *myo3*Δ*acidic myo5*Δ*acidic pan1*Δ*acidic* mutant (see Fig. 3.7(d)). The Myo5 peak height is increased by 120% in the mutant cells. Our models do not treat Myo5 explicitly, but the negative-feedback effect seen in Figs. 3.5a and 3.6b may also contribute to the effect seen here. The effect requires the *pan1*Δ*acidic* mutation; the peak height is essentially unchanged in the *myo3*Δ*acidic myo5*Δ*acidic* mutant. The requirement for the *pan1*Δ*acidic* mutation in the case of Myo5 might result from the binding of Pan1 to Myo5 [116], but we do not know precisely how this binding would affect the Myo5 count. The lifetime is also increased in the *myo3*Δ*acidic myo5*Δ*acidic pan1*Δ*acidic* and *myo3*Δ*acidic myo5*Δ*acidic* mutants. The Myo5 count is affected much less by mutations in Las17 and Pan1. The Myo3 count is generally less sensitive to mutations than the Myo5 count. We do not know the reason for this difference. However, we are not aware of *in vitro* measurements of the nucleation activity of Myo3, so it is possible that Myo3 is a weaker nucleator than Myo5.

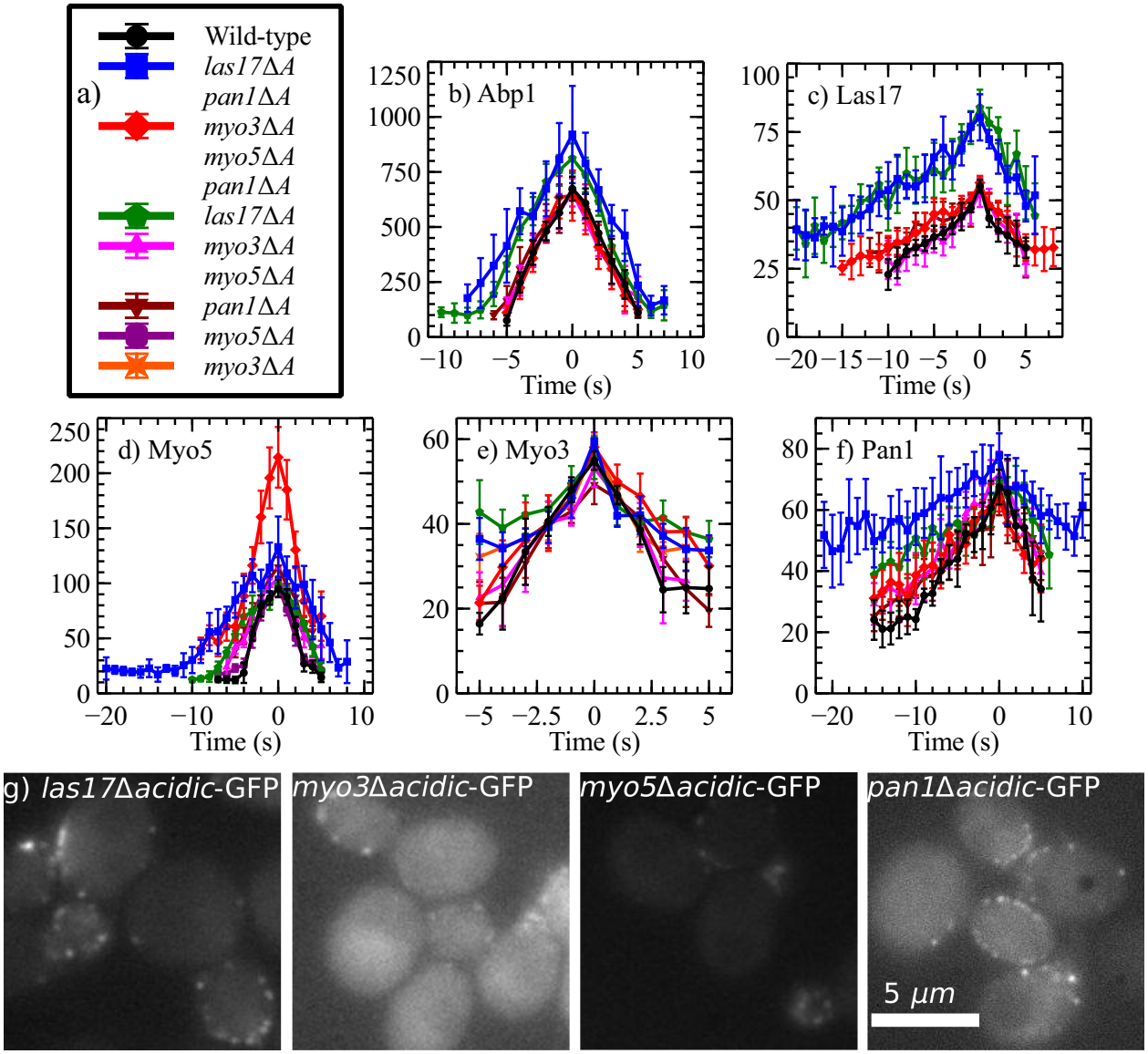

Figure 3.7: Measured time courses of Abp1, Las17, Myo5, Myo3, and Pan1 for wild-type cells and several mutants. ΔA in the legend means $\Delta acidic$. Numbers of patches measured (N) in Abp1-GFP are $N = 184, 132, 148, 274, 64, 331$, for wild-type, *las17*$\Delta A$ *pan1*ΔA, *myo3*ΔA *myo5*ΔA *pan1*ΔA, *las17*ΔA, *myo3*ΔA *myo5*ΔA and *pan1*ΔA respectively. Following the same order, in Las17-GFP, $N = 197, 202, 181, 151, 88, 202$. In Myo5-GFP, $N = 279, 90, 677, 366, 517, 491$. In Myo3-GFP, $N = 307, 437, 601, 161, 159, 187, 627$. In Pan1-GFP, $N = 206, 263, 183, 347, 151, 96$. In addition, for Myo5-GFP *myo5*ΔA, $N = 1070$. Plotted points correspond to mode values; error bars are the standard deviation of a distribution of mode values obtained by bootstrapping (see Appendix). Frame (g) shows representative fluorescence images of GFP-labeled regulators.

Acidic-Domain Mutation of Pan1 Extends Pan1 Lifetime. For Pan1, the peak height is not significantly changed by any of the mutations. However, its lifetime is dramatically increased in the *las17*Δ*acidic pan1*Δ*acidic* mutant. Treating this effect within our theoretical framework would require the inclusion of multiple regulators, which is beyond the scope of the present paper.

3.4 Discussion

We have tested a negative-feedback mechanism for protein dynamics at endocytic actin patches in budding yeast, using both stochastic-growth simulations and rate-equation models. Both of these models reproduce the pulse nature of the protein time courses. In addition, they predict (Figs. 3.5a and 3.6b) that the maximum counts of Arp2/3 regulators will be increased by mutations that reduce the regulators' activity. We tested the robustness of the prediction by varying key assumptions (see Appendix) and found the prediction to be robust to these variations.

The physical mechanism is the following: branching and concomitant actin polymerization increase the probability for Arp2/3 regulators to leave the membrane, either by being directly pulled off with the nascent branch or via mechanical effects. Therefore reducing branching/actin polymerization increases the fraction of regulators left on the membrane. The prediction was confirmed *in vivo* by analyzing movies of CME in live cells to evaluate the time courses of the regulators, in wild-type cells and cells with mutated Arp2/3-binding domains. Large increases in the counts were seen for Las17 and Myo5, the regulators having the strongest branching activity (Figs. 3.7(c) and 3.7(d)).

Another mechanism that might explain the increased Arp2/3 regulator counts is that the mutations reduce the strength of the binding between Arp2/3 complex and the regulators. This corresponds to reducing the parameter α in our models, which determines the rate of regulator detachment. We have implemented this hypothesis, and find that it can match the increase in Arp2/3 regulator peak height, but it greatly overestimates the increase in the F-actin peak height. Therefore we feel that the negative-feedback mechanism based on the branching rate is a more likely explanation.

The negative-feedback models can also explain the increased F-actin peak height caused by some acidic-domain mutations (Fig. 3.7(b)). What other mechanisms might explain this observation?

a) If actin assembly at endocytic actin patches were diffusion-limited, i. e. every actin monomer that contacts the patch region is polymerized, then reducing k_{br} would not decrease F_{max}. However, this assumption is not likely to hold. If one considers the actin patch as a spherical perfect absorber of radius $R = 100\ nm$ [18], assumes a diffusion coefficient of $D = 5\mu m^2$ for monomeric actin [50], and takes a monomeric actin concentration of $C = 2\ \mu M$, one obtains a diffusion-limited monomer flux [117] of $4\pi DCR = 7500$ monomers/s. This is considerably greater than our maximum measured actin assembly rate of 900 monomers/s obtained by multiplying the maximum slope of Fig 3.7(b) by a conversion factor of 8.9 to obtain the F-actin assembly rate. In addition, the diffusion-limiting hypothesis does not explain our measured increase of both F-actin and regulator peak height.

b) Weakened regulator-Arp2/3 binding caused by acidic-domain mutations could enhance

Arp2/3 release from the regulators bound to the membrane. This could explain the F-actin results in two ways. First, release of Arp2/3 complex from regulators has been shown to accelerate branch formation [20]. Second, enhanced Arp2/3 release could accelerate polymerization by reducing the force opposing actin polymerization. Finally, as mentioned above, weakening of the regulator-Arp2/3 binding could cause fewer regulators to detach from the membrane. We again treated this effect by reducing α. As mentioned above, the predictions fit the data poorly.

Thus we feel that the negative-feedback hypothesis is the most likely explanation of this observation. Since the model with negative feedback driven entirely by membrane tension (mechanisms B2 and B3 in Fig. 3.1, Appendix) did not fit the data, the negative feedback interaction must depend to some extent on branching (mechanism B1). Another observation supporting mechanism B1 is that the regulators assemble almost independently. Figs. 3.7(c) and 3.7(d) show that acidic-domain mutation of one particular regulator affects that same regulator most strongly, with relatively weak effects on the other regulators. This argues against mechanisms B2 and B3 being dominant. These mechanisms would predict that mutation of Las17 would affect Las17 and Myo3/5 roughly equally, since they are both at the base of the invagination [10]. Only mechanism B1, where individual branching events lead to regulator detachment, would lead to the observed independent assembly of the regulators. On the other hand, we found that reproducing the actin comets in *sla2* deletion mutants required a mechanical coupling in the negative feedback term. A likely explanation of these findings is that detachment of regulators from the membrane is driven by branch formation,

with a rate depending on force. This could be included by generalizing our model to have a deformation-dependent α. Such a model would have additional fitting parameters, and in the absence of more detailed information about the mechanochemical couplings, we did not pursue this approach.

Another key assumption of our model is that of autocatalytic Las17 assembly, independent of F-actin. An alternate hypothesis is that Las17 assembly passively follows the assembly of an upstream factor in the endocytic patch. Ref. [72] showed that mutation of clathrin, which acts upstream of Las17, reduces the Las17 lifetime. This suggests that clathrin aids Las17 assembly. But the very different time courses of Las17 and clathrin argue against Las17 following clathrin passively. Clathrin may rather act as a platform for autocatalytic Las17 assembly. Bzz1 has also been found to activate the fission yeast Las17 analog Wsp1 [118]. Our assembly dynamics could describe this system provided that Wsp1 is assumed to assemble in a background containing Bzz1. The autocatalytic Las17 assembly hypothesis could be tested by measuring the effects of more upstream proteins, such as Bzz1, on Las17 assembly.

Despite the large evolutionary distance between budding yeast and fission yeast, the need to overcome a large turgor pressure in both organisms may have led to some commonality in their endocytic machineries. Thus the basic mechanisms studied here for budding yeast may also be relevant to fission yeast. A major difference between the two systems is the larger counts of most of the patch constituents in fission yeast [13, 79] vs budding yeast [113, 9, 10]. In our model, a multiplication of all time courses by, for example, a factor of two could be

obtained by the following adjustments: i) doubling L_0, L_2, f_a, and the starting number of actin filaments, and ii) reducing k_{br} by 50% and k_0 by 75%. This system would generate twice as much force. Thus the higher protein counts in fission yeast may help overcome the higher turgor pressure in this system relative to budding yeast.

Another difference between budding yeast and fission yeast is the larger inward motion of Wsp1 in fission yeast [13] (nearly 300 nm). This suggests that a substantial fraction of the Wsp1 i) incorporates into the actin network, or ii) moves up the sides of the tubule. If i) holds, and Wsp1 in the network continues to activate Arp2/3 complex, the negative-feedback mechanism treated here could be weaker. If ii) holds, actin polymerization will exert forces perpendicular to the sides of the tubule, which will compress it, and thus aid the scission process. However, less force would be available for pulling the invagination into the cytoplasm. Finally, the time course of Wsp1 [13] has a faster assembly period than that for Las17.

We do not know how modifying the model to treat fission yeast would change the results. However, the negative-feedback interaction explored here may be relevant to several finding regarding fission yeast: i) Treatment with CK-666, which inhibits Arp2/3-based branching, was found to give nearly unchanged F_{max} values [73]. In a model without negative feedback, a large drop in F_{max} would have occurred. ii) Mutation of cofilin gave actin patches that were brighter by 10% to 70% [73, 79], similar to our predictions for budding yeast (Fig. 3.5b).

Could the model predictions made here be reproduced by previous models in the literature? Ref. [16] treated a feedforward model of endocytosis in fission yeast using a pulse

of active WASP (corresponding to L in our calculations) with a fixed magnitude and time dependence. This model treats branching using several steps, but our k_{br} would correspond most closely to the activation rate of Arp2/3 bound to a filament. Reducing this rate by 40% would cause a large reduction in F_{max}, unlike the increase seen in our data and models. Furthermore, L_{max} would be unchanged, since a fixed pulse height and shape were assumed. Therefore the model of Ref. [16] would require substantial modification to reproduce our predictions and experimental findings.

Ref. [16] also reported a number of uncapped filaments $N_u \simeq 8$. In contrast, we find that $N_u \simeq 140$. We believe the discrepancy arises because Ref. [16] did not treat the effects of opposing force on the growing filaments. If we multiply the on-rate assumed in [16] by a factor of $exp(-f_a\delta/N_u k_B T)$, the value of N_u required to match the maximum polymerization rate of 2000 s^{-1} [16] increases. For $f_a = 415\ pN$, as above, this approach gives $N_u = 101$.

The model of Ref. [15] for budding yeast includes the following chain of feedback interactions of polymerized actin onto membrane-bound agents that act upstream of actin nucleation: $F \rightarrow$ *membrane bending* $\rightarrow$ *coat protein turnover*, as well as another chain including PIP2 hydrolysis. The net result of each of these chains is that F feeds back negatively on the coat proteins C. The model did not treat actin regulators explicitly. However, if the regulators were taken be included in C, and k_{br} were to be identified with the rate constant k_7 (Eq. (4) of Ref. [15]) coupling C to actin assembly, a reduction in k_7 could lead to an increase in C_{max}, paralleling the increase in L_{max} that we have predicted and observed. It is not clear whether this could lead to an increase in F_{max}, because this requires the increase

in C_{max} to overcome the direct effect of decreasing k_7.

A major difference between the present model and that of Ref. [15] is in the assumed distribution of actin polymerization. Ref. [15] assumes actin polymerization focused on the invagination, while we take it to be focused in a disk-like region around the invagination. Our assumption is based on explicit mechanical calculations [95] showing that a disk-like distribution can lead to a density of pulling force much greater than the polymerization stall stress. We are not aware of calculations showing that polymerization in the bud region can produce pulling forces. The merits of the differing assumptions about the distribution of actin polymerization could be directly evaluated via superresolution measurements of the distribution of regulators.

The mathematical similarity between our models and those used previously to treat F-actin waves in mammalian cells (reviewed in Ref. [66]) suggests similarities between endocytosis and F-actin waves. They are, indeed, parallel in several aspects. As in the case of endocytosis, actin regulators (WAVE complex) and Type-1 myosins (Myosin 1B) in actin waves precede F-actin [119, 120]. In both processes, phosphoinositides enhance actin polymerization [121]. Finally, Cdc42 waves, which should correspond to F-actin waves, are closely coupled to clathrin waves [122], which could drive waves of endocytosis. Thus these two phenomena may be variants of the same process.

The negative-feedback interaction studied here may be a generic component of the circuits by which the cell controls actin dynamics at the membrane. It provides a natural mechanism for generating a burst of actin polymerization where needed. It also prevents excessive local

F-actin buildup that could otherwise result from autocatalytic branching polymerization. Finally, it could act as a homeostatic mechanism protecting actin assembly against perturbations. A robust finding of our models is that large changes in key rates, such as those of branching and severing, have surprisingly modest effects on the peak F-actin count.

3.5 Appendix

3.5.1 Robustness of stochastic-grown results to variations in parameters and assumptions

We have varied several key parameters and assumptions in the stochastic model and calculated the corresponding changes in the predictions. In all cases where we could fit the wild-type data, we found that reductions in k_{br} caused substantial increases in L_{max} and F_{max}, a persistent patch phenotype was found under *sla2* mutation, and latrunculin treatment gave persistent Las17 patches. We refit the models in those cases where the initial variations of doubling or halving a parameter predicted more than a 25% change in the peak protein counts. In these cases, we performed an approximate refit by varying just k_{br}, except as indicated below.

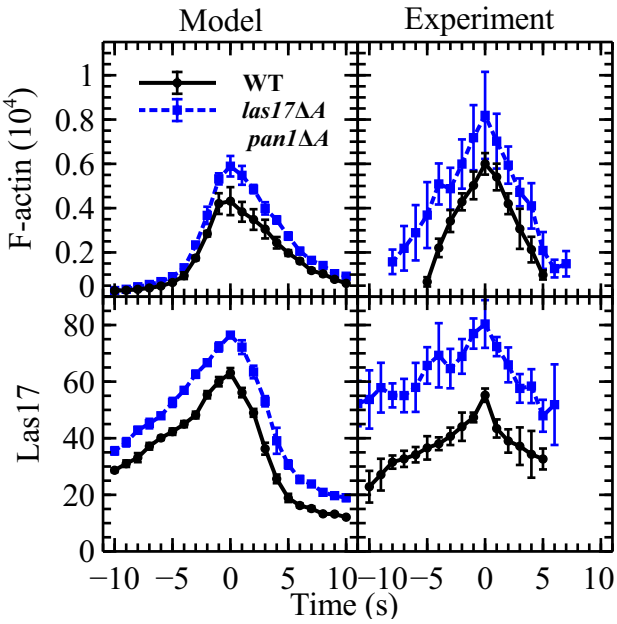

Figure 3.8: Time course of stochastic-growth model with branching rate proportional to L^2, compared with experimental data.

1. The branching width W, with baseline value 20 subunit sizes (54nm), was varied from 10 subunits to 40 subunits. Reducing it to 10 subunits increased F_{max} by 11% and increased L_{max} by 7% wild-type cells, with corresponding changes of -2% and 5% for Increasing W to 40 subunits reduced the wild-type F_{max} by 7% and increased the wild-type L_{max} by 3%, with corresponding changes of -20% and 5% for the acidic-domain mutant.

2. The primer filament length l_0, with baseline value 20, (in subunits) was varied from 10 to 30. For $l_0 = 10$, F_{max} was reduced by 9% and L_{max} by 5%, with corresponding changes of 7% and 0 for the acidic-domain mutation. For $l_0 = 30$, F_{max} was decreased by 20% while L_{max} was decreased by 8%. with corresponding changes of 7% and 0 for the acidic-domain mutation.

3. The initial filament number N_0, with baseline value 5, was varied from 0 to 10. For $N_0 = 0$, F_{max} decreased by 11% and L_{max} by 3%, with corresponding changes of -2% and 0 for the acidic-domain mutation. For $N_0 = 10$ (refit), the wildtype F_{max} and L_{max} values increased by 6% and 3% respectively, with corresponding changes of 2% and 10% for the acidic-domain mutation. The primer nucleation rate k_{nuc}, with baseline value 0.02 s^{-1}, was also varied from 0.01 s^{-1} to 0.03 s^{-1}. For $k_{nuc} = 0.01s^{-1}$, F_{max} and L_{max} were increased by 11% and 7% respectively, with corresponding changes of 5% and 10% for the acidic-domain mutation. For $k_{nuc} = 0.03s^{-1}$ (refit), the wildtype F_{max} and L_{max} values dropped by 6% and increased by 7% respectively, with corresponding

changes of -12% and -4% for the acidic-domain mutation.

4. The initial Las17 number L_0, with baseline value 20, was varied from 10 to 30. For $L_0 =$ 10 (refit) , the wildtype F_{max} and L_{max} values increased by 7% and 2% respectively, with corresponding changes of -2% and 2% for the acidic-domain mutation. For $L_0 = 30$ (refit), The wildtype F_{max} and L_{max} values increased by 9% and 5% respectively, with corresponding changes of 1% and 2% for the acidic-domain mutation.

5. The total force opposing invagination, f_a, with baseline value 415 pN, was varied from 208 pN to 830 pN. For $f_a = 208$ pN, F_{max} increased by 22% and L_{max} decreased by 10%, with corresponding changes of 11% and -1% for the acidic-domain mutation. For $f_a =$ 830 pN (refit by varying $k_{on}G$), the wildtype F_{max} and L_{max} values increased by 7% and 14% respectively, with corresponding changes of -3% and 6% for the acidic-domain mutation.

6. An alternative branching term, with the branching rate per subunit proportional to $k_{br}L^2$, was refitted by varying k_{br}. This form reflects the possibility of cooperative activation by Arp2/3 regulators, and was used in Ref. [91]. F_{max} for wild-type was 25% lower than baseline, and L_{max} was 7% higher, with corresponding changes of -30% and -10% for the acidic-domain mutation. The resulting time courses for wild-type and acidic-domain mutants (Fig. 3.8) were similar to those for the baseline parameters.

7. Three alternative mathematical forms for the assembly of L were tested. For these we performed a more complete refitting procedure. i) $L\,(L_2 - L)$. F_{max} for wild-type

was 6% higher than baseline, and L_{max} was unchanged, with corresponding changes of +11% and -7% for the acidic-domain mutation. ii) $L^3\,(L_2 - L)$. F_{max} for wild-type was 28% higher than baseline and L_{max} was 19% higher, with corresponding changes of +11% and +11% for the acidic-domain mutation. iii) $(L_2 - L)$ (no autocatalytic assembly). In this case no pulse behavior was seen, rather both F and L approached finite values in steady state. Thus fitting either wild-type or mutant data requires an autocatalytic assembly term.

8. We implemented and fitted a model in which negative feedback was taken to be proportional to the extent of membrane bending, which in turn was taken proportional to the average position of the actin filament pointed ends. This model gave poor results: i) only a very small fraction of the runs gave pulses; ii) under acidic-domain mutations, F_{max} decreased rather than increasing; iii) the fluctuations in patch brightness were larger than in the experimental data.

3.5.2 Fitting of models

In fitting the stochastic-growth model, we began with the results from the four-variable model and by hand increased $k_{on}G$ to account for opposing force, increased k_{br} to account for the finite branching region, and adjusted k_{sev} to get roughly correct peak heights. Then we randomly sampled parameter space by taking trial steps in random directions with Gaussian-sampled amplitudes. The trial steps were accepted if the value of the following objective function was reduced:

$$\mathcal{O} = \frac{1}{6}\Bigg[\frac{\left(L_{exp}^{max} - L_{mod}^{max}\right)^2}{L_{exp}^{max(2)}} + \frac{\left(F_{exp}^{max} - F_{mod}^{max}\right)^2}{F_{exp}^{max(2)}} + \frac{\left(N_{exp}^{max} - N_{mod}^{max}\right)^2}{N_{exp}^{max(2)}} + \frac{\left(C_{exp}^{max} - C_{mod}^{max}\right)^2}{C_{exp}^{max(2)}} + \frac{\left(\tau_{exp}^{L} - \tau_{mod}^{L}\right)^2}{\tau_{exp}^{L(2)}} + \frac{\left(\tau_{exp}^{F} - \tau_{mod}^{F}\right)^2}{\tau_{exp}^{F(2)}}\Bigg],$$

where N^{max} is the maximum number of filaments (experimental number obtained as the Arp2/3 count from Ref. [9]), C^{max} is the maximum capping protein count [9], and τ^F and τ^L are the full widths at half-maximum of the F and L time courses.

For the rate-equation models, we used the following objective functions, where the subscripts "exp" and "mod" denote the experimental data and the model predictions:

For the branching nucleation model,

$$\mathcal{O} = \frac{1}{11}\sum_{i=-9}^{1}\frac{\left(L_{exp,i} - L_{mod,i}\right)^2}{L_{exp,i}^2} + \frac{1}{9}\sum_{i=-4}^{4}\frac{\left(F_{exp,i} - F_{mod,i}\right)^2}{F_{exp,i}^2}, \tag{3.4}$$

where at each time point $t = 1s \times i$. The cutoffs in the sums were chosen so as to focus on the regions with higher counts, where there is less fractional error.

For the spontaneous nucleation model,

$$\mathcal{O} = \frac{1}{8}\sum_{i=-5}^{2}\frac{\left(L_{exp,i} - L_{mod,i}\right)^2}{L_{exp,i}^2} + \frac{1}{7}\sum_{i=-3}^{3}\frac{\left(F_{exp,i} - F_{mod,i}\right)^2}{F_{exp,i}^2} \tag{3.5}$$

The parameter values minimizing the objective functions were found by searching over

a multidimensional rectangular grid of parameter values, with a mesh size roughly equal to 0.01 times the lowest value treated.

3.5.3 Two-variable rate-equation model based on spontaneous nucleation of actin filaments

We use the following equations:

$$\frac{dL}{dt} = k_0 L\,(L - L_1)\,(L_2 - L) - k_{det} L F, \tag{3.6}$$

$$\frac{dF}{dt} = k_{sp} \bar{l} L - k_{sev} F, \tag{3.7}$$

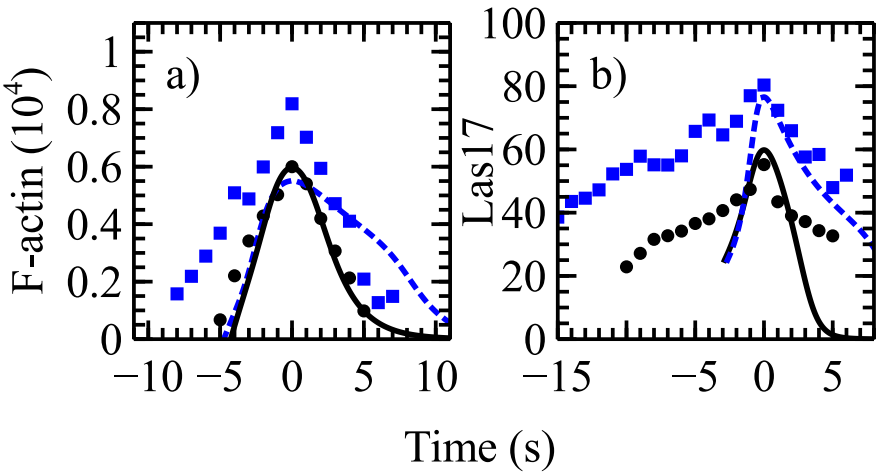

Figure 3.9: Time courses from spontaneous-nucleation rate-equation model. Parameters are $k_{sp} = 2.35 s^{-1}$, $k_{sev} = 0.555 s^{-1}$, $k_0 = 5.98 \times 10^{-4} s^{-1}$, $\bar{l} = 30$, $L_1 = 17$, and $L_2 = 101$. Initial values are $L_0 = 25$ and $F_0 = 1$. Black denotes wild-type and blue denotes *las17*Δ*acidic pan1*Δ*acidic* cells. Solid and dashed curves are model predictions; dots are experimental data. For clarity, the error bars for the data are not indicated here, but they are given in Fig. 5a. F-actin is obtained as measured Abp1 count multiplied by a conversion factor 8.9 (see text).

They differ from the branching nucleation model in two ways: i) In the first term of dL/dt a factor of L is replaced by $L - L_1$, where L_1 is an additional parameter that acts as a threshold for regulator assembly. We were unable to obtain reasonable fits of the time courses of L and F without this term. ii) The first term in dF/dt is independent of F, since the model assumes that preexisting actin filaments are not required for nucleation of new filaments.

The data shown in Fig. 3.9 reveal a less accurate fit than was obtained by the branching nucleation model (Fig. 6). The model does not capture the slow assembly of L, although it fits the Abp1 time course slightly better than the main model. The spontaneous nucleation model also does not describe the mutant phenotypes as well. Small decreases in k_{sp} lead to decreases in F_{max}, while larger decreases lead to the formation of permanent patches. However, the prediction of increased L_{max} is obtained in this model, as in the branching nucleation model. The cofilin and latrunculin phenotypes are handled roughly as well as by the branching nucleation model.

Figure 3.10 compares the branching and spontaneous nucleation models to the experimental data.

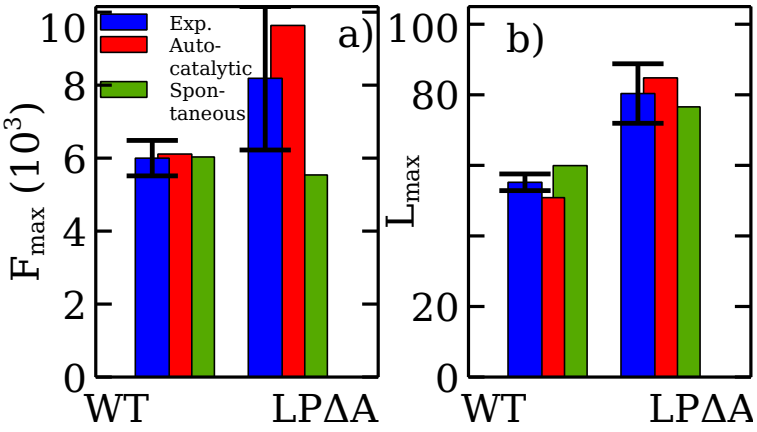

Figure 3.10: Bar graphs comparing autocatalytic branching with spontaneous nucleation model. The autocatalytic model predicts a increase in F_{max} for the *las17*Δ*acidic pan1*Δ*acidic* mutant (LPΔA), consistent with the experiments, while the spontaneous nucleation model predicts a small decrease. Both models predict an increase in L_{max} in the LPΔA mutant. The autocatalytic model prediction is, however, closer to the experimentally measured increase.

3.5.4 Four-variable rate-equation model

This model extends the two-variable autocatalytic model, by treating separate nucleation and polymerization processes, for capped and uncapped filaments. It has the following equations:

$$\frac{dL}{dt} = k_0 (L_2 - L) L^2 - \alpha k_{br} L F, \tag{3.8}$$

$$\frac{dN_u}{dt} = k_{br} L F - k_{cap} N_u, \tag{3.9}$$

$$\frac{dN_c}{dt} = k_{cap} N_u - k_{sev} N_c, \tag{3.10}$$

$$\frac{dF}{dt} = k_{on} G N_u - k_{sev} F, \tag{3.11}$$

where N_c and N_u are the numbers of capped and uncapped filaments, k_{br} is the branching rate, and $k_{on}G$ is the polymerization rate. The parameters are given in Table 3.3. We take $k_{on}G = 20s^{-1}$ on the basis of the roughly micromolar actin concentration G [8] and $k_{on} = 11.6\mu M^{-1}s^{-1}$ [59]. We also take $k_{cap} = k_{on}G/\bar{l}$, where the average filament length $\bar{l} = 30$ as in the two-variable model. For the remaining parameter values, we began with the values from the two-variable model. We found that a good fit to the data was obtained provided that α was reduced by 10%. The two- and four-variable models are compared in Fig. 3.11, revealing close agreement between the models for the wild-type case. The predictions for the effects of mutations are also similar to those of the two-variable model, with a 40% reduction of k_{br} leading to a 60% increase in L_{max} and a 40% increase in F_{max}. This supports our treatment of actin polymerization as a single-step process.

3.5.5 Patch Tracking and Protein Counting

The movies were first cropped to separate GFP-Cse4 tagged cells from those with tagged endocytic proteins. Endocytic patches were tracked using the *TrackMate* plugin (N. Perry, J.-Y. Tinevez, and J. Schindelin, http://fiji.sc/TrackMate) of ImageJ (Wayne Rasband, NIH, Bethesda, MD, http://imagej.nih.gov/ij/). The X-Y positions of the patch centroids in each movie time frame, obtained from TrackMate, were read into a custom C++ code that processed the track data and used it to obtain the intensity numbers from the movie frames. As in [123], we took the intensity I_P of each patch in a time frame as the total intensity in a square region of 9×9 pixels around the center of the patch, minus a background intensity

I_B. I_B is the average intensity of a region ranging from 10×10 to 13×13 pixels around the center.

The tracks were then filtered by the C code so that only relatively isolated and distinguishable patches were left. The criteria were that i) the closest distance from any filtered track to any other track should be larger than 13 pixels, and ii) the contrast of a given track, defined as

$$C = \frac{\sum I_P}{\sum I_B}, \tag{3.12}$$

should exceed a chosen threshold value C_{min}, where the summation is over all frames in which the track appears. Because the different tagged protein have different counts, it is necessary to set C_{min} differently for different proteins. For each one, we ordered all the originally selected wild-type tracks based on their time-averaged contrast C values, in a composite image. Then we obtained C_{min} by visually determining at what value the tracks seemed sufficiently clear. C_{min} was taken the same for all of the mutants having a given tagged protein. The final tracks left after the filtering based on the criteria i) and ii) were used for further analysis.

The GFP-Cse4 patches were analyzed in the same way. To convert intensity to protein count, we assumed that each GFP-Cse4 patch has 109 molecules of Cse4 [9]. The intensities of the endocytic protein patches and the Cse4 patches were found to decrease systematically over the 60 second period of the experiments, probably because of photobleaching. To correct

for photobleaching, we fit the time dependence of the Cse4 patch intensity to an exponential form, using a linear regression on a logarithmic plot. This gave a time course of Cse4 patch intensity. Then the count of each endocytic protein was obtained by dividing I_P by the time-dependent Cse4 patch intensity, and then multiplying by 109.

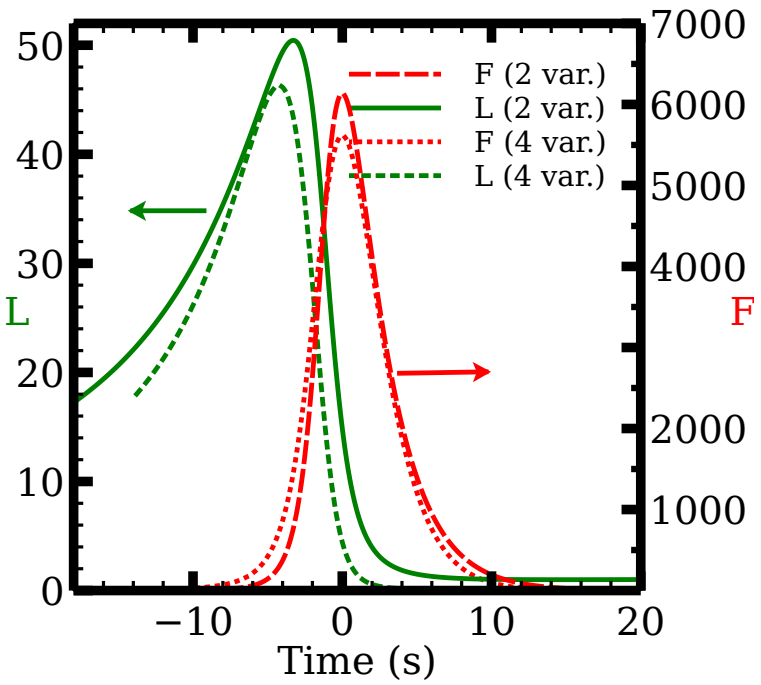

Figure 3.11: Four-variable rate-equation model compared to two-variable model. F is measured Abp1 count multiplied by a conversion factor of 8.9 (see text) to approximate the F-actin count. Arrows indicate which vertical scale to read.

For statistical analysis, we aligned the tracks at their maximum intensity points (t=0), and binned the intensities at each time. The track data for Abp1 is illustrated in Fig. 3.12, in which the distribution of patch intensities at a given time is indicated by the gray-scaled bins.

Parameters	
$k_{on}G$ (s^{-1})	20.0
k_{cap} (s^{-1})	0.667
k_{br} $(10^{-3}s^{-1})$	0.957
k_{sev} (s^{-1})	0.427
k_0 $(10^{-5}s^{-1})$	3.93
α	0.122
L_2	101
Initial Conditions	
L_0	18
$N_{u,0}$	1
$N_{c,0}$	0
F_0	1

Table 3.3: Four-variable model parameters and initial conditions

To obtain a meaningful plot of intensity as a single function of time, we followed the procedure of Ref. [9] and estimated the mode of the intensity distribution at each time point. The *modeest* package (P. Poncet, http://cran.r-project.org/web/packages/modeest/index.html) in R (D. Bates *et al.*, http://www.r-project.org/) was used to implement the mode value estimation method developed in [124]. This was used to generate the protein time courses that we plot. To generate the error bars, we generated a distribution of 1000 mode values by bootstrapping; the error bars correspond to the standard deviation of this distribution.

3.5.6 Yeast strains

The strains used in this study are listed in Table 3.4. All strains are derived from YJC6494, an isogenic strain generated by diploidizing BY4741. Green fluorescent protein (GFP) fusion constructs were generated at the endogenous loci as described [125, 126]. Mutations

were generated in an isogenic background as described [127]. Mutations were confirmed by PCR and DNA sequencing. The proper localization of the mutant proteins to patches was confirmed by fluorescence microscopy imaging of GFP in the cells (Fig. 7g).

3.5.7 Microscopy and image analysis

Strains were grown overnight in liquid YPD at 30 $^{\circ}C$ to an optical density of $\sim$ 0.1 - 0.5. Cells were collected by centrifugation (82 $\times$ g, 5 min) and suspended in SD-complete medium or in a simplified nonfluorescent synthetic medium [128]. To quantitate GFP fusion protein levels, we mixed cells expressing Cse4-GFP with cells expressing the fusion of interest and placed them onto a 1% agarose pad, made with the same nonfluorescent medium and covered with a # 1 coverslip. Wide-field fluorescence movies were collected with an inverted microscope (IX81, Olympus) using a 1.35 NA 100X oil immersion objective, and an EM-CCD camera (Hamamatsu). A 1.5X magnifier was placed in front of the camera, and a 1.6X magnifier was placed in the light path in the body of the microscope. GFP was excited with laser illumination at 488 nm. Images were collected from a single, equatorial focal plane with 900 ms exposures at 1 frame/s. For all experiments, at least 60 consecutive frames were collected. The temperature was maintained at 30 $^{\circ}C$ for all observations. Integrated GFP fluorescence intensity was converted to absolute numbers of molecules using the fluorescence of Cse4, as in Ref. [9]. Because we use wide-field microscopy, 3D motion causes smaller intensity changes than would occur in confocal microscopy. Ref. [129] showed that even being out of focus by several microns does not change the integrated patch fluorescence significantly.

The in-plane motion of Las17 before disassembly is less than 100 nm, and most of the Abp1 has disassembled by the time it has moved 200-300 nm. We see no reason why 3D motion should be larger than in-plane motion. In addition, the quality control criterion in the patch tracking method (see below) tends to eliminate tracks in which the patches move out of focus before disassembling.

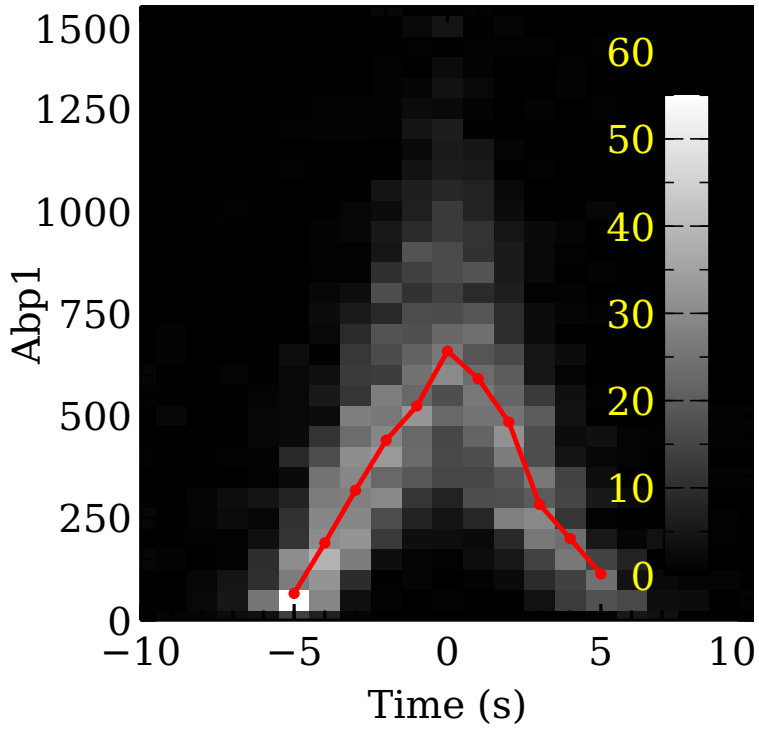

Figure 3.12: Protein count distribution for Abp1. The gray scale indicates the relative probability of measuring a given number of Abp1 molecules (vertical axis) at any given time. The mode value of the distribution is plotted in red.

Table 3.4: Yeast strains used.

Strain	Genotype	Source
BY4741	*MATa his3Δ1 leu2Δ0 met15Δ0 ura3Δ0*	[125]
YJC6494	*MATα/MATa his3Δ1/his3Δ1 leu2Δ0/leu2Δ0 met15Δ0/met15Δ0 ura3Δ0/ura3Δ0*	[9]
YJC6718	*MATa Abp1-GFP-SpHIS5 his3Δ1 leu2Δ0 met15Δ0 ura3Δ0*	[9]
YJC6719	*MATα Abp1-GFP-SpHIS5 his3Δ1 leu2Δ0 met15Δ0 ura3Δ0*	[9]
YJC6720	*MATa Abp1-GFP-SpHIS5 his3Δ1 leu2Δ0 met15Δ0 ura3Δ0*	[9]
YJC6721	*MATα Abp1-GFP-SpHIS5 his3Δ1 las17Δacidic-CaURA3MX4 leu2Δ0 met15Δ0 ura3Δ0*	[9]
YJC6722	*MATα Abp1-GFP-SpHIS5 his3Δ1 las17Δacidic-CaURA3MX4 leu2Δ0 met15Δ0 ura3Δ0*	[9]
YJC6723	*MATa Abp1-GFP-SpHIS5 his3Δ1 las17Δacidic-CaURA3MX4 leu2Δ0 met15Δ0 ura3Δ0*	[9]
YJC6725	*MATa Cse4-GFP-SpHIS5 his3Δ1 leu2Δ0 met15Δ0 ura3Δ0*	[9]
YJC6726	*MATα Cse4-GFP-SpHIS5 his3Δ1 leu2Δ0 met15Δ0 ura3Δ0*	[9]
YJC6797	*MATα Myo5-GFP-SpHIS5 his3Δ1 leu2Δ0 met15Δ0 ura3Δ0*	This study
YJC6798	*MATa Myo5-GFP-SpHIS5 his3Δ1 leu2Δ0 met15Δ0 ura3Δ0*	This study
YJC6799	*MATa Myo5-GFP-SpHIS5 his3Δ1 leu2Δ0 met15Δ0 ura3Δ0*	This study
YJC6800	*MATa Myo5-GFP-SpHIS5 his3Δ1 las17Δacidic-CaURA3MX4 leu2Δ0 met15Δ0 ura3Δ0*	This study
YJC6801	*MATa Myo5-GFP-SpHIS5 his3Δ1 las17Δacidic-CaURA3MX4 leu2Δ0 met15Δ0 ura3Δ0*	This study
YJC6802	*MATα Myo5-GFP-SpHIS5 his3Δ1 las17Δacidic-CaURA3MX4 leu2Δ0 met15Δ0 ura3Δ0*	This study
YJC6910	*MATα Myo3-GFP-SpHIS5 his3Δ1 leu2Δ0 met15Δ0 ura3Δ0*	This study
YJC6911	*MATa Myo3-GFP-SpHIS5 his3Δ1 leu2Δ0 met15Δ0 ura3Δ0*	This study
YJC6912	*MATa Myo3-GFP-SpHIS5 his3Δ1 leu2Δ0 met15Δ0 ura3Δ0*	This study
YJC6913	*MATa Myo3-GFP-SpHIS5 his3Δ1 las17Δacidic-CaURA3MX4 leu2Δ0 met15Δ0 ura3Δ0*	This study
YJC6914	*MATa Myo3-GFP-SpHIS5 his3Δ1 las17Δacidic-CaURA3MX4 leu2Δ0 met15Δ0 ura3Δ0*	This study
YJC6915	*MATα Myo3-GFP-SpHIS5 his3Δ1 las17Δacidic-CaURA3MX4 leu2Δ0 met15Δ0 ura3Δ0*	This study
YJC6931	*MATa Pan1-GFP-SpHIS5 his3Δ1 leu2Δ0 met15Δ0 ura3Δ0*	This study
YJC6932	*MATa Pan1-GFP-SpHIS5 his3Δ1 leu2Δ0 met15Δ0 ura3Δ0*	This study
YJC6933	*MATα Pan1-GFP-SpHIS5 his3Δ1 leu2Δ0 met15Δ0 ura3Δ0*	This study
YJC6934	*MATa Pan1-GFP-SpHIS5 his3Δ1 las17Δacidic-CaURA3MX4 leu2Δ0 met15Δ0 ura3Δ0*	This study
YJC6935	*MATa Pan1-GFP-SpHIS5 his3Δ1 las17Δacidic-CaURA3MX4 leu2Δ0 met15Δ0 ura3Δ0*	This study
YJC6936	*MATα Pan1-GFP-SpHIS5 his3Δ1 las17Δacidic-CaURA3MX4 leu2Δ0 met15Δ0 ura3Δ0*	This study
YJC6958	*MATa Abp1-GFP-SpHIS5 his3Δ1 leu2Δ0 met15Δ0 pan1Δacidic-kanMX6 ura3Δ0*	[9]
YJC6959	*MATa Abp1-GFP-SpHIS5 his3Δ1 leu2Δ0 met15Δ0 pan1Δacidic-kanMX6 ura3Δ0*	[9]
YJC6960	*MATα Abp1-GFP-SpHIS5 his3Δ1 leu2Δ0 met15Δ0 pan1Δacidic-kanMX6 ura3Δ0*	[9]
YJC6961	*MATa Abp1-GFP-SpHIS5 his3Δ1 las17Δacidic-CaURA3MX4 leu2Δ0 met15Δ0 pan1Δacidic-kanMX6 ura3Δ0*	[9]

Continued on next page

Table 3.4 – *Continued from previous page*

Strain	Genotype	Source
YJC6962	*MATa Abp1-GFP-SpHIS5 his3Δ1 las17Δacidic-CaURA3MX4 leu2Δ0 met15Δ0 pan1Δacidic-kanMX6 ura3Δ0*	[9]
YJC6963	*MATα Abp1-GFP-SpHIS5 his3Δ1 las17Δacidic-CaURA3MX4 leu2Δ0 met15Δ0 pan1Δacidic-kanMX6 ura3Δ0*	[9]
YJC7148	*MATa Abp1-GFP-SpHIS5 his3Δ1 leu2Δ0 met15Δ0 myo3Δacidic-hphMX4 myo5Δacidic-kanMX6 ura3Δ0*	[9]
YJC7149	*MATα Abp1-GFP-SpHIS5 his3Δ1 leu2Δ0 met15Δ0 myo3Δacidic-hphMX4 myo5Δacidic-kanMX6 ura3Δ0*	[9]
YJC7150	*MATα Abp1-GFP-SpHIS5 his3Δ1 leu2Δ0 met15Δ0 myo3Δacidic-hphMX4 myo5Δacidic-kanMX6 ura3Δ0*	[9]
YJC7151	*MATα Abp1-GFP-SpHIS5 his3Δ1 las17Δacidic-CaURA3MX4 leu2Δ0 met15Δ0 myo3Δacidic-hphMX4 myo5Δacidic-kanMX6 ura3Δ0*	[9]
YJC7152	*MATα Abp1-GFP-SpHIS5 his3Δ1 las17Δacidic-CaURA3MX4 leu2Δ0 met15Δ0 myo3Δacidic-hphMX4 myo5Δacidic-kanMX6 ura3Δ0*	[9]
YJC7153	*MATα Abp1-GFP-SpHIS5 his3Δ1 las17Δacidic-CaURA3MX4 leu2Δ0 met15Δ0 myo3Δacidic-hphMX4 myo5Δacidic-kanMX6 ura3Δ0*	[9]
YJC7310	*MATa Abp1-GFP-SpHIS5 his3Δ1 leu2Δ0 met15Δ0 myo3Δacidic-hphMX4 myo5Δacidic-natMX4 pan1Δacidic-kanMX6 ura3Δ0*	[9]
YJC7311	*MATa Abp1-GFP-SpHIS5 his3Δ1 leu2Δ0 met15Δ0 myo3Δacidic-hphMX4 myo5Δacidic-natMX4 pan1Δacidic-kanMX6 ura3Δ0*	[9]
YJC7312	*MATα Abp1-GFP-SpHIS5 his3Δ1 leu2Δ0 met15Δ0 myo3Δacidic-hphMX4 myo5Δacidic-natMX4 pan1Δacidic-kanMX6 ura3Δ0*	[9]
YJC7361	*MATα Myo3-GFP-SpHIS5 his3Δ1 leu2Δ0 met15Δ0 pan1Δacidic-kanMX6 ura3Δ0*	This study
YJC7362	*MATα Myo3-GFP-SpHIS5 his3Δ1 leu2Δ0 met15Δ0 pan1Δacidic-kanMX6 ura3Δ0*	This study
YJC7363	*MATa Myo3-GFP-SpHIS5 his3Δ1 leu2Δ0 met15Δ0 pan1Δacidic-kanMX6 ura3Δ0*	This study
YJC7364	*MATα Myo3-GFP-SpHIS5 his3Δ1 las17Δacidic-CaURA3MX4 leu2Δ0 met15Δ0 pan1Δacidic-kanMX6 ura3Δ0*	This study
YJC7365	*MATa Myo3-GFP-SpHIS5 his3Δ1 las17Δacidic-CaURA3MX4 leu2Δ0 met15Δ0 pan1Δacidic-kanMX6 ura3Δ0*	This study
YJC7366	*MATa Myo3-GFP-SpHIS5 his3Δ1 las17Δacidic-CaURA3MX4 leu2Δ0 met15Δ0 pan1Δacidic-kanMX6 ura3Δ0*	This study
YJC7369	*MATa Pan1-GFP-SpHIS5 his3Δ1 leu2Δ0 myo3Δacidic-hphMX6 myo5Δacidic-kanMX4 met15Δ0 ura3Δ0*	This study
YJC7370	*MATα Pan1-GFP-SpHIS5 his3Δ1 leu2Δ0 myo3Δacidic-hphMX6 myo5Δacidic-kanMX4 met15Δ0 ura3Δ0*	This study
YJC7371	*MATα Pan1-GFP-SpHIS5 his3Δ1 leu2Δ0 myo3Δacidic-hphMX6 myo5Δacidic-kanMX4 met15Δ0 ura3Δ0*	This study
YJC7372	*MATa Pan1-GFP-SpHIS5 his3Δ1 las17Δacidic-CaURA3MX4 leu2Δ0 myo3Δacidic-hphMX6 myo5Δacidic-kanMX4 met15Δ0 ura3Δ0*	This study

Continued on next page

Table 3.4 – *Continued from previous page*

Strain	Genotype	Source
YJC7373	*MATα Pan1-GFP-SpHIS5 his3Δ1 las17Δacidic-CaURA3MX4 leu2Δ0 myo3Δacidic-hphMX6 myo5Δacidic-kanMX4 met15Δ0 ura3Δ0*	This study
YJC7374	*MATα Pan1-GFP-SpHIS5 his3Δ1 las17Δacidic-CaURA3MX4 leu2Δ0 myo3Δacidic-hphMX6 myo5Δacidic-kanMX4 met15Δ0 ura3Δ0*	This study
YJC7376	*MATα Las17-GFP-SpHIS5 his3Δ1 leu2Δ0 met15Δ0 ura3Δ0*	This study
YJC7377	*MATa Las17-GFP-SpHIS5 his3Δ1 leu2Δ0 met15Δ0 ura3Δ0*	This study
YJC7395	*MATα Myo5-GFP-SpHIS5 his3Δ1 leu2Δ0 met15Δ0 pan1Δacidic-kanMX6 ura3Δ0*	This study
YJC7396	*MATa Myo5-GFP-SpHIS5 his3Δ1 leu2Δ0 met15Δ0 pan1Δacidic-kanMX6 ura3Δ0*	This study
YJC7397	*MATα Myo5-GFP-SpHIS5 his3Δ1 leu2Δ0 met15Δ0 pan1Δacidic-kanMX6 ura3Δ0*	This study
YJC7398	*MATa Myo5-GFP-SpHIS5 his3Δ1 las17Δacidic-CaURA3MX4 leu2Δ0 met15Δ0 pan1Δacidic-kanMX6 ura3Δ0*	This study
YJC7399	*MATa Myo5-GFP-SpHIS5 his3Δ1 las17Δacidic-CaURA3MX4 leu2Δ0 met15Δ0 pan1Δacidic-kanMX6 ura3Δ0*	This study
YJC7400	*MATα Myo5-GFP-SpHIS5 his3Δ1 las17Δacidic-CaURA3MX4 leu2Δ0 met15Δ0 pan1Δacidic-kanMX6 ura3Δ0*	This study
YJC7402	*MATa Las17-GFP-SpHIS5 his3Δ1 leu2Δ0 met15Δ0 ura3Δ0*	This study
YJC7403	*MATa Las17-GFP-SpHIS5 his3Δ1 leu2Δ0 met15Δ0 myo3Δacidic-hphMX6 myo5Δacidic-natMX4 pan1Δacidic-kanMX6 ura3Δ0*	This study
YJC7404	*MATα Las17-GFP-SpHIS5 his3Δ1 leu2Δ0 met15Δ0 myo3Δacidic-hphMX6 myo5Δacidic-natMX4 pan1Δacidic-kanMX6 ura3Δ0*	This study
YJC7405	*MATα Las17-GFP-SpHIS5 his3Δ1 leu2Δ0 met15Δ0 myo3Δacidic-hphMX6 myo5Δacidic-natMX4 pan1Δacidic-kanMX6 ura3Δ0*	This study
YJC7406	*MATa Las17-GFP-SpHIS5 his3Δ1 leu2Δ0 met15Δ0 myo3Δacidic-hphMX6 myo5Δacidic-natMX4 ura3Δ0*	This study
YJC7407	*MATα Las17-GFP-SpHIS5 his3Δ1 leu2Δ0 met15Δ0 myo3Δacidic-hphMX6 myo5Δacidic-natMX4 ura3Δ0*	This study
YJC7408	*MATa Las17-GFP-SpHIS5 his3Δ1 leu2Δ0 met15Δ0 myo3Δacidic-hphMX6 myo5Δacidic-natMX4 ura3Δ0*	This study
YJC7409	*MATa Las17-GFP-SpHIS5 his3Δ1 leu2Δ0 met15Δ0 pan1Δacidic-kanMX6 ura3Δ0*	This study
YJC7410	*MATα Las17-GFP-SpHIS5 his3Δ1 leu2Δ0 met15Δ0 pan1Δacidic-kanMX6 ura3Δ0*	This study
YJC7411	*MATa Las17-GFP-SpHIS5 his3Δ1 leu2Δ0 met15Δ0 pan1Δacidic-kanMX6 ura3Δ0*	This study
YJC7430	*MATα pan1Δacidic-GFP-SpHIS5 his3Δ1 leu2Δ0 met15Δ0 ura3Δ0*	This study
YJC7431	*MATa pan1Δacidic-GFP-SpHIS5 his3Δ1 leu2Δ0 met15Δ0 ura3Δ0*	This study
YJC7432	*MATα pan1Δacidic-GFP-SpHIS5 his3Δ1 leu2Δ0 met15Δ0 ura3Δ0*	This study
YJC7433	*MATa pan1Δacidic-GFP-SpHIS5 his3Δ1 leu2Δ0 met15Δ0 myo3Δacidic-hphMX6 myo5Δacidic-kanMX4 ura3Δ0*	This study
YJC7434	*MATa pan1Δacidic-GFP-SpHIS5 his3Δ1 leu2Δ0 met15Δ0 myo3Δacidic-hphMX6 myo5Δacidic-kanMX4 ura3Δ0*	This study

Continued on next page

Table 3.4 – *Continued from previous page*

Strain	Genotype	Source
YJC7435	*MATa pan1Δacidic-GFP-SpHIS5 his3Δ1 leu2Δ0 met15Δ0 myo3Δacidic-hphMX6 myo5Δacidic-kanMX4 ura3Δ0*	This study
YJC7436	*MATa pan1Δacidic-GFP-SpHIS5 his3Δ1 las17Δacidic-CaURA3MX4 leu2Δ0 met15Δ0 ura3Δ0*	This study
YJC7437	*MATa pan1Δacidic-GFP-SpHIS5 his3Δ1 las17Δacidic-CaURA3MX4 leu2Δ0 met15Δ0 ura3Δ0*	This study
YJC7438	*MATa pan1Δacidic-GFP-SpHIS5 his3Δ1 las17Δacidic-CaURA3MX4 leu2Δ0 met15Δ0 ura3Δ0*	This study
YJC7439	*MATα las17Δacidic-GFP-SpHIS5 his3Δ1 leu2Δ0 met15Δ0 ura3Δ0*	This study
YJC7440	*MATα las17Δacidic-GFP-SpHIS5 his3Δ1 leu2Δ0 met15Δ0 ura3Δ0*	This study
YJC7441	*MATa las17Δacidic-GFP-SpHIS5 his3Δ1 leu2Δ0 met15Δ0 ura3Δ0*	This study
YJC7442	*MATα las17Δacidic-GFP-SpHIS5 his3Δ1 leu2Δ0 met15Δ0 myo3Δacidic-hphMX6 myo5Δacidic-kanMX4 ura3Δ0*	This study
YJC7443	*MATa las17Δacidic-GFP-SpHIS5 his3Δ1 leu2Δ0 met15Δ0 myo3Δacidic-hphMX6 myo5Δacidic-kanMX4 ura3Δ0*	This study
YJC7444	*MATa las17Δacidic-GFP-SpHIS5 his3Δ1 leu2Δ0 met15Δ0 myo3Δacidic-hphMX6 myo5Δacidic-kanMX4 ura3Δ0*	This study
YJC7445	*MATa las17Δacidic-GFP-SpHIS5 his3Δ1 leu2Δ0 met15Δ0 pan1Δacidic-kanMX6 ura3Δ0*	This study
YJC7446	*MATα las17Δacidic-GFP-SpHIS5 his3Δ1 leu2Δ0 met15Δ0 pan1Δacidic-kanMX6 ura3Δ0*	This study
YJC7447	*MATa las17Δacidic-GFP-SpHIS5 his3Δ1 leu2Δ0 met15Δ0 pan1Δacidic-kanMX6 ura3Δ0*	This study
YJC7448	*MATα myo3Δacidic-GFP-SpHIS5 his3Δ1 leu2Δ0 met15Δ0 myo5Δacidic-kanMX4 ura3Δ0*	This study
YJC7449	*MATa myo3Δacidic-GFP-SpHIS5 his3Δ1 las17Δacidic-CaURA3MX4 leu2Δ0 met15Δ0 myo5Δacidic-kanMX4 ura3Δ0*	This study
YJC7450	*MATa myo3Δacidic-GFP-SpHIS5 his3Δ1 las17Δacidic-CaURA3MX4 leu2Δ0 met15Δ0 myo5Δacidic-kanMX4 ura3Δ0*	This study
YJC7451	*MATa myo3Δacidic-GFP-SpHIS5 his3Δ1 las17Δacidic-CaURA3MX4 leu2Δ0 met15Δ0 myo5Δacidic-kanMX4 ura3Δ0*	This study
YJC7452	*MATa myo3Δacidic-GFP-SpHIS5 his3Δ1 leu2Δ0 met15Δ0 ura3Δ0*	This study
YJC7453	*MATa myo3Δacidic-GFP-SpHIS5 his3Δ1 leu2Δ0 met15Δ0 ura3Δ0*	This study
YJC7454	*MATα myo3Δacidic-GFP-SpHIS5 his3Δ1 leu2Δ0 met15Δ0 myo5Δacidic-natMX4 pan1Δacidic-kanMX6 ura3Δ0*	This study
YJC7455	*MATα myo3Δacidic-GFP-SpHIS5 his3Δ1 leu2Δ0 met15Δ0 myo5Δacidic-natMX4 pan1Δacidic-kanMX6 ura3Δ0*	This study
YJC7456	*MATa myo3Δacidic-GFP-SpHIS5 his3Δ1 leu2Δ0 met15Δ0 myo5Δacidic-natMX4 pan1Δacidic-kanMX6 ura3Δ0*	This study
YJC7457	*MATα myo5Δacidic-GFP-SpHIS5 his3Δ1 leu2Δ0 met15Δ0 myo3Δacidic-kanMX4 ura3Δ0*	This study
YJC7458	*MATα myo5Δacidic-GFP-SpHIS5 his3Δ1 leu2Δ0 met15Δ0 ura3Δ0*	This study
YJC7459	*MATa myo5Δacidic-GFP-SpHIS5 his3Δ1 leu2Δ0 met15Δ0 ura3Δ0*	This study

Continued on next page

Table 3.4 – *Continued from previous page*

Strain	Genotype	Source
YJC7460	*MATα myo5Δacidic-GFP-SpHIS5 his3Δ1 las17Δacidic-CaURA3MX4 leu2Δ0 met15Δ0 myo3Δacidic-kanMX4 ura3Δ0*	This study
YJC7461	*MATα myo5Δacidic-GFP-SpHIS5 his3Δ1 las17Δacidic-CaURA3MX4 leu2Δ0 met15Δ0 myo3Δacidic-kanMX4 ura3Δ0*	This study
YJC7462	*MATα myo5Δacidic-GFP-SpHIS5 his3Δ1 las17Δacidic-CaURA3MX4 leu2Δ0 met15Δ0 myo3Δacidic-kanMX4 ura3Δ0*	This study
YJC7463	*MATa myo5Δacidic-GFP-SpHIS5 his3Δ1 leu2Δ0 met15Δ0 myo3Δacidic-kanMX4 ura3Δ0*	This study
YJC7464	*MATα myo5Δacidic-GFP-SpHIS5 his3Δ1 leu2Δ0 met15Δ0 myo3Δacidic-kanMX4 ura3Δ0*	This study
YJC7465	*MATa myo5Δacidic-GFP-SpHIS5 his3Δ1 leu2Δ0 met15Δ0 myo3Δacidic-kanMX4 pan1Δacidic-kanMX6 ura3Δ0*	This study
YJC7466	*MATa myo5Δacidic-GFP-SpHIS5 his3Δ1 leu2Δ0 met15Δ0 myo3Δacidic-kanMX4 pan1Δacidic-kanMX6 ura3Δ0*	This study
YJC7467	*MATa myo5Δacidic-GFP-SpHIS5 his3Δ1 leu2Δ0 met15Δ0 myo3Δacidic-kanMX4 pan1Δacidic-kanMX6 ura3Δ0*	This study
YJC7468	*MATa myo3Δacidic-GFP-SpHIS5 his3Δ1 leu2Δ0 met15Δ0 myo5Δacidic-kanMX4 ura3Δ0*	This study
YJC7469	*MATα myo3Δacidic-GFP-SpHIS5 his3Δ1 leu2Δ0 met15Δ0 myo5Δacidic-kanMX4 ura3Δ0*	This study

Chapter 4

PARTIAL DIFFERENTIAL EQUATION MODEL OF ACTIN NETWORK

4.1 Introduction

Partial differential equation (PDE) approaches can well describe biological networks that have spatially non-uniform concentrations varying over time. For intracellular actin networks, we develop a PDE model that includes important processes such as branching, polymerization, capping and severing. A key advantage of this approach is that many additional physical assumptions can be implemented and tested in this model. These assumptions are difficult or impossible to implement in the ordinary differential equation (ODE) models in the previous two chapters. The most important assumption is that branching can only happen in a branching layer near the cell membrane. This is because the actin regulator Las17 only activates the Arp2/3 complex when it binds the coat protein Bzz1, which is attached to the membrane. Thus, there are rarely branching events in the bulk of the network. It is hard to separate the branching layer from the bulk using ODEs because the variables in the ODEs represent the total counts of the proteins. However, PDE models can conveniently incorporate the branching layer because they treat the probability distribution function (PDF) of the network, i.e. the density of F-actin at varying distances from the membrane. The total rate of branching is obtained as an integral over a thin region of space corresponding to the

branching layer. Therefore, the PDE model is much more accurate than the ODE model to describe branching, a surface effect. In addition, the Brownian ratchet effect and the force exerted on the network can be implemented in our PDE model but are difficult to include in the ODE models.

Another advantage of the PDE model is that we can obtain the geometry of the actin network. For example, in the cell, the actin network may be distributed in a ring region near the membrane. The ring-like distribution can be obtained from the PDE if it is set up using an appropriate coordinate system. This type of information is difficult to include in ODEs. Also, in three dimensions an endocytic patch of F-actin is probably a hemisphere like structure. The PDE model can describe this structure as well, while the ODE models cannot. Overall, the PDE is a more complete approach to modeling the actin network. The only trade off is that the PDE requires much more computation time than the ODEs. But solving PDEs can be greatly accelerated using GPU algorithms. Also, because the PDE model is deterministic, there is no need to obtain ensemble averages over many copies of the same calculation, like the stochastic simulation in Chapter 3. Therefore, it is much faster to calculate within the PDE model, making the PDE approach a balanced one in terms of accuracy and computation load. Table 4.1 summarizes the three models to reveal their advantages and disadvantages.

In this chapter, the PDE model is introduced and discussed. The general PDE has two spatial dimensions. A simplified version of the PDE, with one spatial dimension, is derived and applied to model endocytosis. The details of the calculation are discussed and the results

	ODE	PDE	Stochastic
Protein Number	**Yes**	**Yes**	**Yes**
Geometry	**No**	**Yes**	**Yes**
Brownian Ratchet	**No**	**Yes**	**Yes**
Spatial Concentration	**No**	**Yes**	**Yes**
Computational Load	Low	Medium	High
Ensemble Average	**No**	**No**	**Yes**

Table 4.1: Different aspects of the three models.

are presented. We find that the PDE model not only matches the experimental data and the stochastic model well, but also makes a rich set of predictions for experimental conditions that have not yet been studied. The PDE model predicts several types of dynamic behaviors, including single transient pulses, repeating pulses and permanent patches, depending on the parameter values.

4.2 General Theory

The general model we propose is a two dimensional PDE written as

$$\begin{aligned}\frac{\partial \rho(x,y,t)}{\partial t} &= \sum_{i=1}^{l(y,t)} \frac{k_{br}(y+i)}{2}\rho(x-i,y+i,t) \\ &+ \sum_{i=1}^{l(y,t)} \frac{k_{br}(y+i)}{2}\rho(x+i,y+i,t) - k_{sev}\rho(x,y,t), \end{aligned} \tag{4.1}$$

where x and y are position variables in the membrane and perpendicular to it, k_{br} is a spatially dependent branching rate, l is a space- and time-dependent filament length, and $\rho(x,y)$, representing the number of subunits at (x,y), is the non-normalized distribution function of the subunits in the network. The rate parameters are the same as those in

Chapter 3. The PDE is constructed in a discrete coordinate system, in which the smallest unit of the coordinate in both x and y directions is one subunit. The subunit coordinate can be converted to a length coordinate considering that each subunit is $2.7nm$ long, and that the filaments have either a $45°$ or $-45°$ angle with respect to the y axis, see Fig. 4.1.

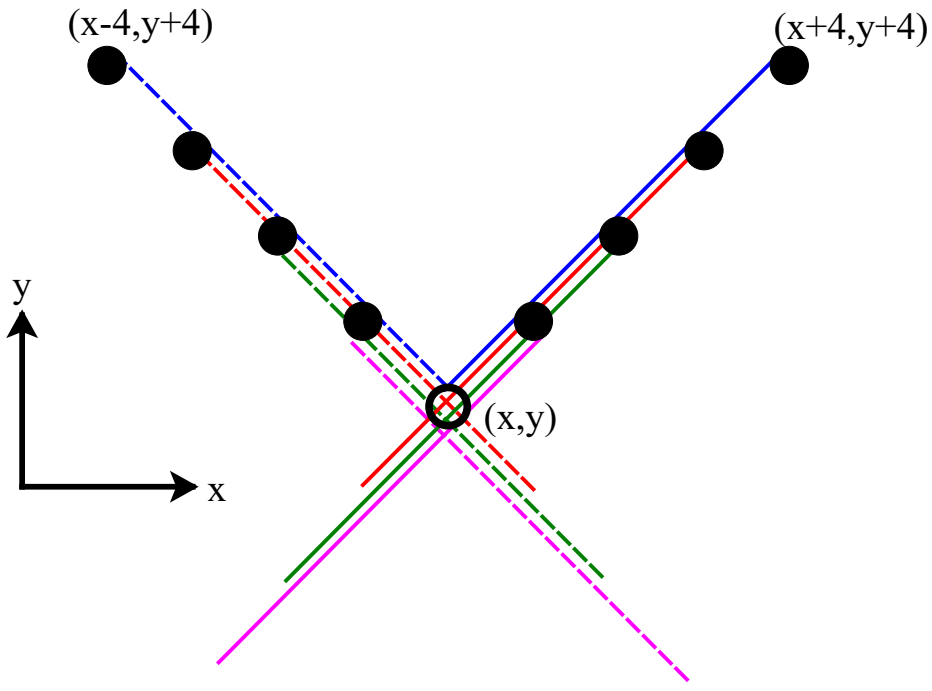

Figure 4.1: In this case, $l = 4$. Four branches from the left (dashed lines) and four branches from the right (solid lines) can give one more subunit at (x, y) (circle). All the possible starting points are shown in solid dots. x axis is lateral and y axis is vertical.

Fig. 4.1 explains the geometry treated by Eq. 4.1, and the coordinates, for the case of $l = 4$. There are in total eight possible locations from where a new branch can reach a point

(x, y), four on the left and the other four on the right. For each new branch reaching (x, y), $\rho(x, y)$ is increased by 1. The branching process from the left four locations is described by the first term in Eq. 4.1, while branching from the right four locations is from the second term. The third term in Eq. 4.1 represents the main actin disassembly mechanism, which we take to be severing. There are thus a total of eight filaments that can increase the subunit number at (x, y) by one. These filaments are plotted in Fig. 4.1 in different colors. The filaments branching from the left are dashed lines and the filaments from the right are solid lines. For a given value of the filament length l, Eq. 4.1 describes all the possible branching events. In more general cases, l is not a constant, but determined by polymerization and capping. The calculation of l will be discussed in the next section.

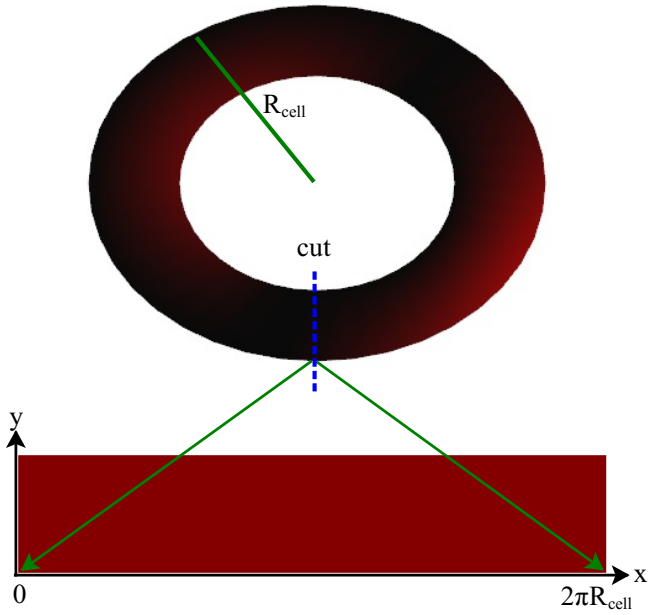

Figure 4.2: A flat network can approximately describe the actin cortex around the cell.

Using the PDE 4.1, the actin network in different shapes and configurations can be well

described. For cell migration, the actin network is distributed near the inner side of the membrane, and constitutes the actin cortex, shown in Fig. 4.2. Because the circumference of the cell, $2\pi R_{cell}$, is much larger than the depth of the network, it is convenient to assume a flat network with periodic boundary conditions, so that $\rho\left(x = 2\pi R_{cell}, y, t\right) = \rho\left(x = 0, y, t\right)$.

During endocytosis, some models assume that actin network looks like a pudding which is hollow in the middle whereas in others, it is believed to be a hemisphere [95]. This complicated hollow-pudding shape can be described by treating only the cross-section if azimuthal symmetry is assumed. The cross-section reduces the dimension of the network from three to two. After calculating the actin distribution in the cross-section using the PDE method, a rotation about the y axis gives the three dimensional network back.

From the above examples, we see that Eq. 4.1 can describe phenomena as diverse as cell migration and endocytosis, when certain approximations or symmetry are assumed. The equation is generally applicable to actin dynamics in various contexts. In the next section, an even simpler version of Eq. 4.1 is derived, and its application to endocytosis is discussed.

4.3 Simplified Model

The general equation 4.1 provides a detailed description of actin network in a rather simple form. However, it is even simpler if we ignore one more dimension. In the case of endocytosis, the y dimension is more important than x because the force is dependent only on y. Also, the branching layer depends on y. Although the Las17 ring depends on x, we can make an approximation that the actin network is not much wider than the ring. We thus assume that branching is independent of x and do not treat the Las17 ring explicitly. By integrating

both sides of 4.1 with respect of x, we obtain

$$\frac{\partial \rho\left(y,t\right)}{\partial t}=\sum_{i=1}^{l(y,t)}k_{br}\left(y+i\right)\rho\left(y+i,t\right)-k_{sev}\rho\left(y,t\right). \tag{4.2}$$

The implementation of Eq. 4.2 depends on various assumptions.

1. **Branching Function**. The branching is determined by the Las17 number L, the branching layer thickness y_{branch}, and the maximum branching rate k_{br}^{max},

$$k_{br}\left(y\right)=k_{br}^{max}Le^{-\frac{y-y_{mem}}{y_{branch}}}. \tag{4.3}$$

   The branching function monotonically decreases as the branching point gets away from the membrane, mimicking the branching layer.

2. **Las17**. The Las17 dynamics is the same as in the ODE model of Chapter 3, except that the F-actin pulling off the Las17 is not the total F-actin but rather the branching rate determined by the branching layer. The rate equation for L is

$$\frac{dL}{dt}=k_0L^2\left(L_2-L\right)-\alpha F_{br} \tag{4.4}$$

$$F_{br}\left(t\right)=\int_{y_{min}}^{y_{max}}k_{br}\left(y\right)\rho\left(y,t\right)dy, \tag{4.5}$$

   where y_{min} and y_{max} are shown in Fig. 4.3.

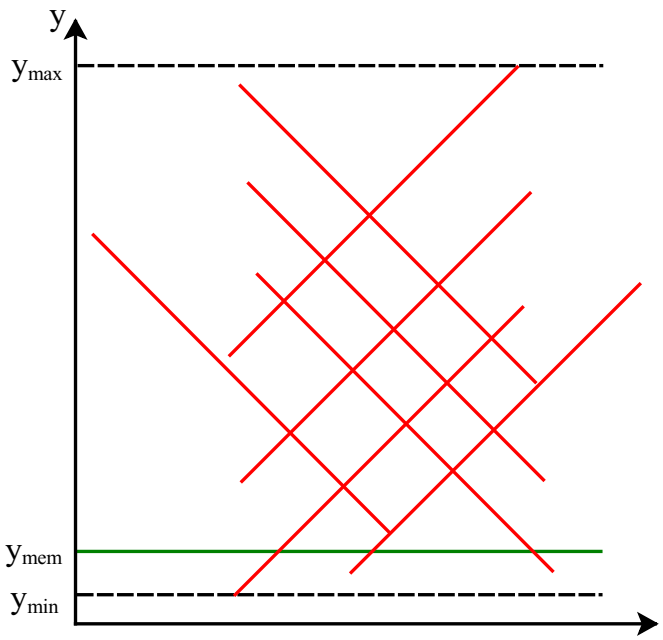

Figure 4.3: A schematic of the actin network and variables.

3. **Membrane Dynamics**. The membrane near the endocytic site is assumed to move according to the dynamics of actin network. We assume that the central region of the membrane is attached to the Sla2 cap, thus being fixed to a characteristic position in the actin network, such as the average position of all of the subunits. In this chapter, we ignore the force caused by membrane bending because it is much smaller than the force caused by the turgor pressure. The peripheral region of the membrane undergoes Brownian motion, characterized by the Langevin equation

$$\frac{dy_{mem}}{dt} = \frac{1}{\gamma} f\left(t\right) + \frac{1}{\gamma} f_{rand}, \tag{4.6}$$

where $f(t)$ and f_{rand} are deterministic and random forces, and γ is a drag coefficient. The inertia is ignored considering that the membrane moves in over-damped environment.

4. **Force Balance**. The forces exerted on the membrane are from the turgor pressure (f_{tp}) and actin polymerization (f_{act}). We assume that the actin network can exert force on the membrane and thus be subject to forces from the membrane, only when there is enough F-actin to exert a pulling force on the endocytic coat. Otherwise, the polymerization is not subject to any forces. The actin force depends on how deep the network is embedded into the membrane. The two forces and the total force are

$$f_{tp}(t) = \begin{cases} 200 \quad \text{pN} \quad \text{when } F(t) > 400 \\ 0 \qquad\qquad\qquad \text{otherwise} \end{cases} \tag{4.7}$$

$$f_{act}(t) = \int_{y_{min}}^{y_{mem}} [y - y_{mem}(t)]\, \rho(y,t)\, dy \tag{4.8}$$

$$f(t) = f_{tp}(t) + f_{act}(t). \tag{4.9}$$

5. **Filament Length** l. The length of a new branch l growing to a point y is determined by how many subunits can be polymerized before the filament is capped. Also, l is reduced when force is exerted, based on a factor from the Brownian ratchet mechanism slowing of polymerization:

$$B(t) = e^{-\frac{f(t)a}{N_{att}(t)k_BT}}, \tag{4.10}$$

where

$$N_{att}(t) = \rho\left(y_{mem} + 1\right). \tag{4.11}$$

Thus

$$l(y,t) = \begin{cases} l_{max} = \frac{k_{on}G}{k_{cap}} & \text{when } y - y_{mem}(t) \geq 0 \\ l_{max}B(t) & \text{when } \left[y_{mem}(t) - y\right] \geq l_{max}B(t), \\ \left[y_{mem}(t) - y\right]\left[1 - 1/B(t)\right] + l_{max} & \text{else} \end{cases} \tag{4.12}$$

in which the three possible lengths are illustrated in Fig. 4.4. In the third case, the part affected by the Brownian ratchet (embedded in the membrane) is deducted from l_{max}. The embedded part is then added back, and multiplied by the Brownian ratchet factor Eq. 4.10.

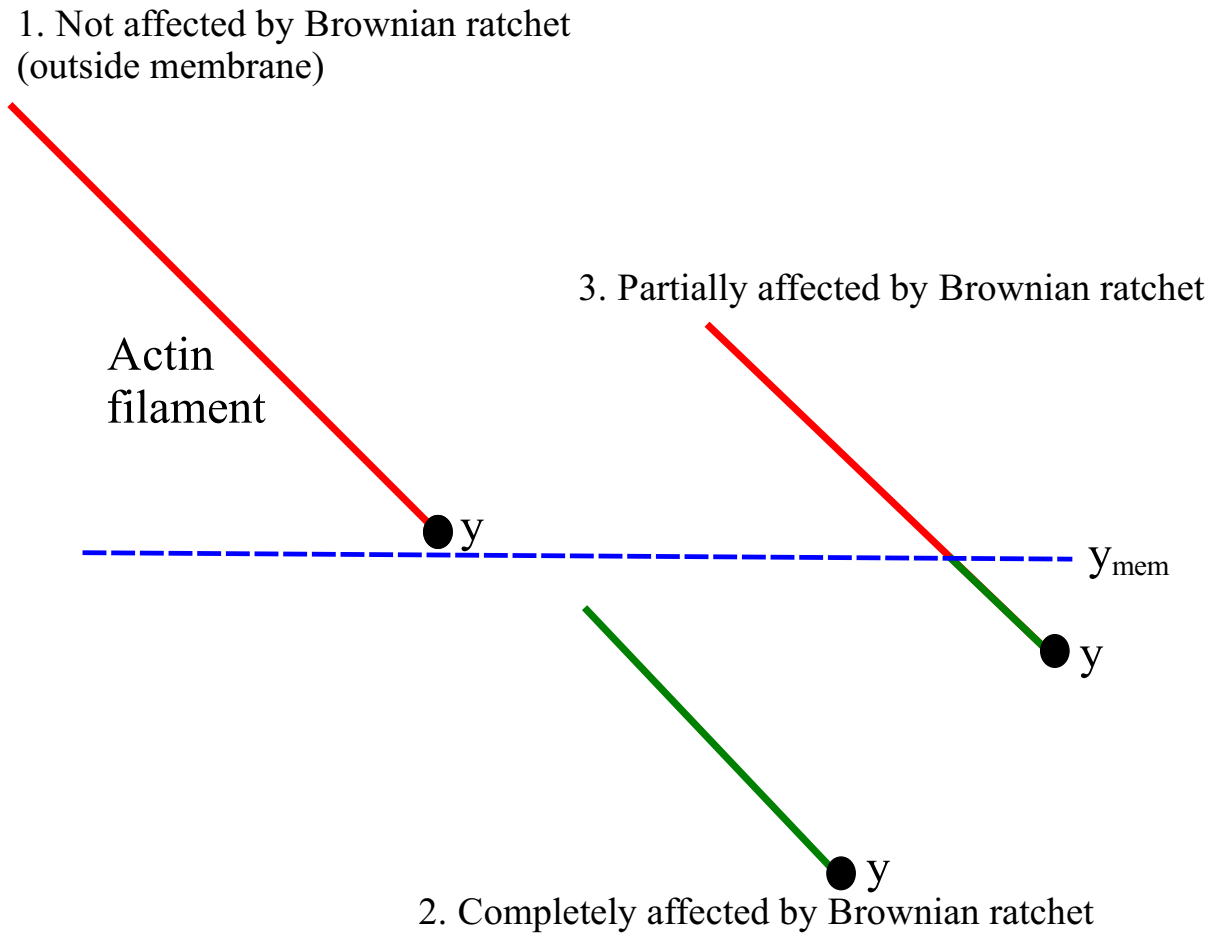

Figure 4.4: A schematic of possible filament lengths l. 1. When the new branched filament (red) is completely outside of the membrane, l is not affected by the Brownian ratchet, corresponding to the first equation in Eq. 4.12. 2. When the new branched filament (green) is completely embedded in the membrane, l is completely affected by the Brownian ratchet, corresponding to the second equation in Eq. 4.12. 3. When the new branched filament (partially green and partially red) is partially embedded in the membrane, l is partially affected by the Brownian ratchet effect, corresponding to the third equation in Eq. 4.12.

Below is the table of summarizing the defined variables, functions and parameters.

Variable/Function	Physical Meaning
x	lateral direction of the network
y	vertical direction of the network
t	time
l	length of branched filament in subunit number
$\rho(x,y,t)$	number of subunit at (x,y,t)
k_{br}	branching function
F_{br}	total F-actin pulling Las17
L	Las17
y_{mem}	position of the membrane
y_{min}	lowest subunit in the network
y_{max}	highest subunit in the network
f	total force
f_{tp}	turgor pressure force
f_{act}	actin force
N_{att}	attaching filament number
Parameter	Physical Meaning
γ	damping coefficient
y_{branch}	characteristic width of the branching layer
l_{max}	longest filament length

Table 4.2: The table of variables, functions and parameters defined in this chapter.

4.4 Results: PDE v.s. Experiment

The PDE model can match the wild-type experimental data well. In Fig. 4.5, the time courses of F and L from the PDE model, in solid lines, match the experimental data points very well. F from the PDE model is calculated as

$$F(t) = \int_{y_{min}}^{y_{max}} \rho(y,t)\, dy. \tag{4.13}$$

The parameters are optimized using the same method as in Chapter 3. A clear pulse behavior is present in the PDE model, just as in the ODE and the stochastic models. Also, the slow

assembly of the Las17 is reproduced. However, comparing the PDE model to the other two models, its advantages are prominent.

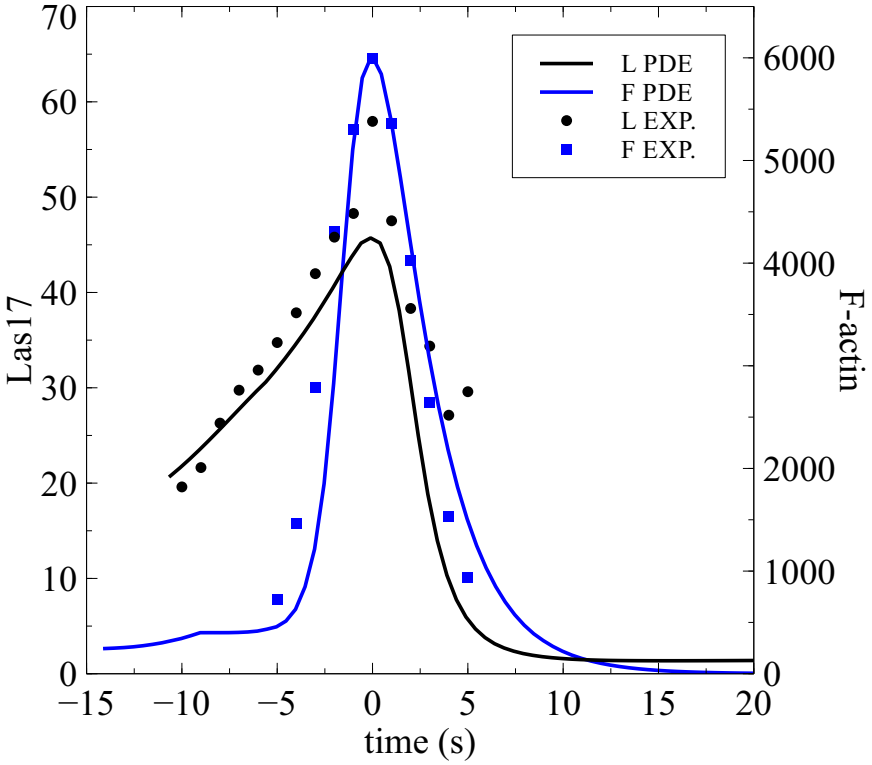

Figure 4.5: PDE result matches experiment for WT.

First, the PDE model is much more complete than the ODE model in representing the actin network. The PDE model incorporates the branching layer, Eq. 4.3, and the Brownian ratchet, Eq. 4.10. Second, the PDE model results agree better with the stochastic model results for the same choice of parameters. Third, the computational load for the PDE is considerably lower than the stochastic model. Optimizing the PDE model to match the experimental data is feasible, unlike optimizing the stochastic model. We ignore the random force in the PDE model for simplicity. Thus there is no need for calculating ensemble average

of the PDE model because it is deterministic. This also obviates the calculation of random numbers in each time step, which is computationally intensive.

In short, the PDE model is overall a complete and computationally friendly model. Studying this model is fast and convenient.

4.5 Results: PDE v.s. ODE

The additional physical properties entering the PDE model affect the calculated properties strongly. We use the same parameters as in the previous section, in the ODE model from Chapter 3. The result of the ODE is very different from that of the PDE, see Fig. 4.6. From the PDE model, a F-actin pulse appears after a Las17 pulse. Both pulses last for normal time periods and reach normal peak heights as in the experiments. However, from the ODE model, the F-actin pulse arrives much earlier and the Las17 pulse does not appear. Also, the F-actin peak height is considerably higher. This difference is hard to reconcile due to the nonuniform actin distribution seen in Fig. 4.6 on the right. Starting with a truncated uniform distribution of F-actin (red curve), the distribution becomes neither uniform nor Gaussian after seconds of simulation. We can not directly add a branching layer or force layer to the ODE model without knowing the distribution. Therefore, the ODE can only serve as a qualitative guide for the stochastic model to match experiments. It can not help to avoid the very time-consuming parameter optimization in the stochastic model. However, the PDE model not only represents the experiments well, but also agrees with the stochastic model to a large extent. We believe the PDE model agrees with the stochastic model (the most realistic model) because the PDE incorporates the branching layer and the force layer.

We present the comparison between the two models in the next section.

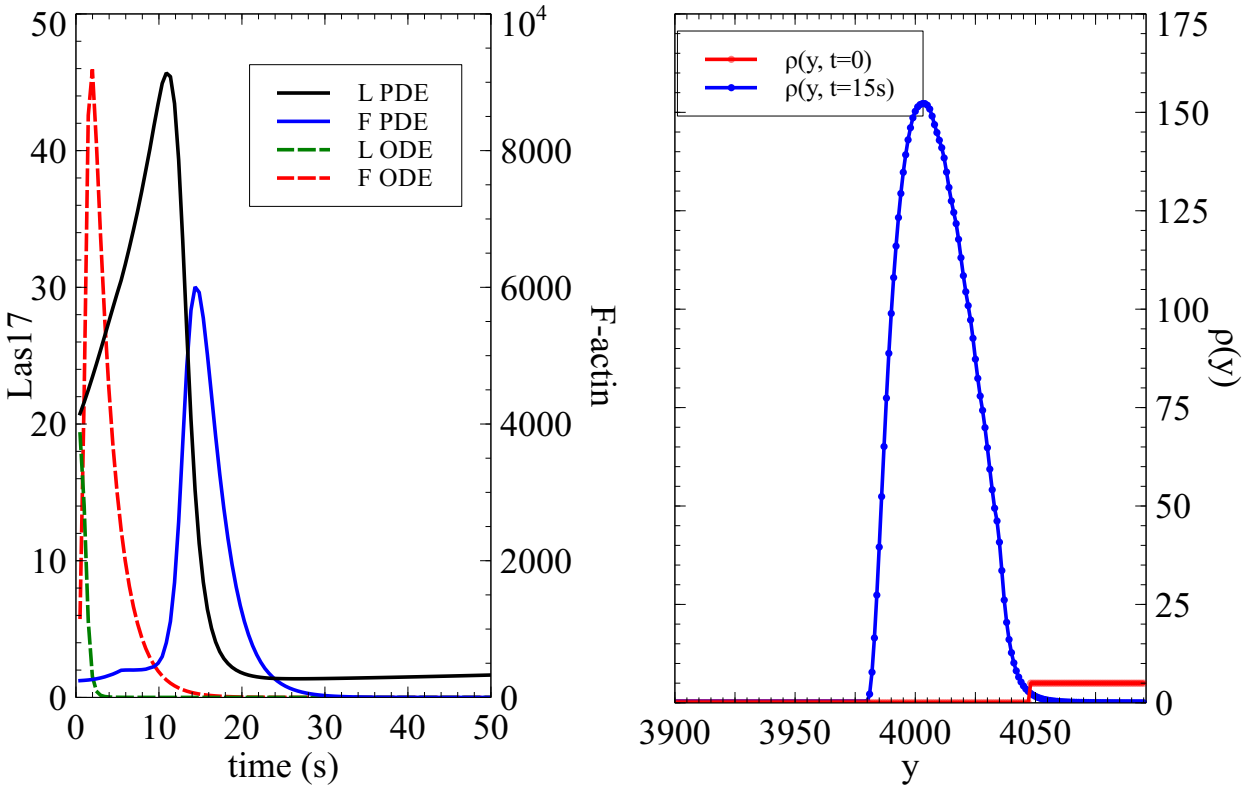

Figure 4.6: PDE and ODE do not agree when given the same parameters. PDE also predicts the spatial distribution of F-actin.

4.6 Results: PDE v.s. Stochastic Model

The PDE model generally agrees well with the stochastic model. Fig. 4.7 shows typical comparison results. Using the same optimized parameters, and some minor modifications to the stochastic model, we see a good match between the two models. The stochastic model then serves to generate a vivid representation of the PDE model. We can use the same three dimensional graphics as in Chapter 3. On the other hand, the PDE model serves as a great tool to search the parameter space for the stochastic model. First, the PDE model can

assist the stochastic model to match the experiment. Second, the PDE model can search the parameter space widely to explore possible behaviors. Not only is the PDE model faster than the stochastic model in doing these things, the fact that it is deterministic is helpful in some cases. For example, it is sometimes hard to tell whether there is an oscillation in a stochastic time course or just a random fluctuation near a steady state. But it is clearly seen in the PDE model. In the next section, there are a couple of concrete examples of searching the parameter space.

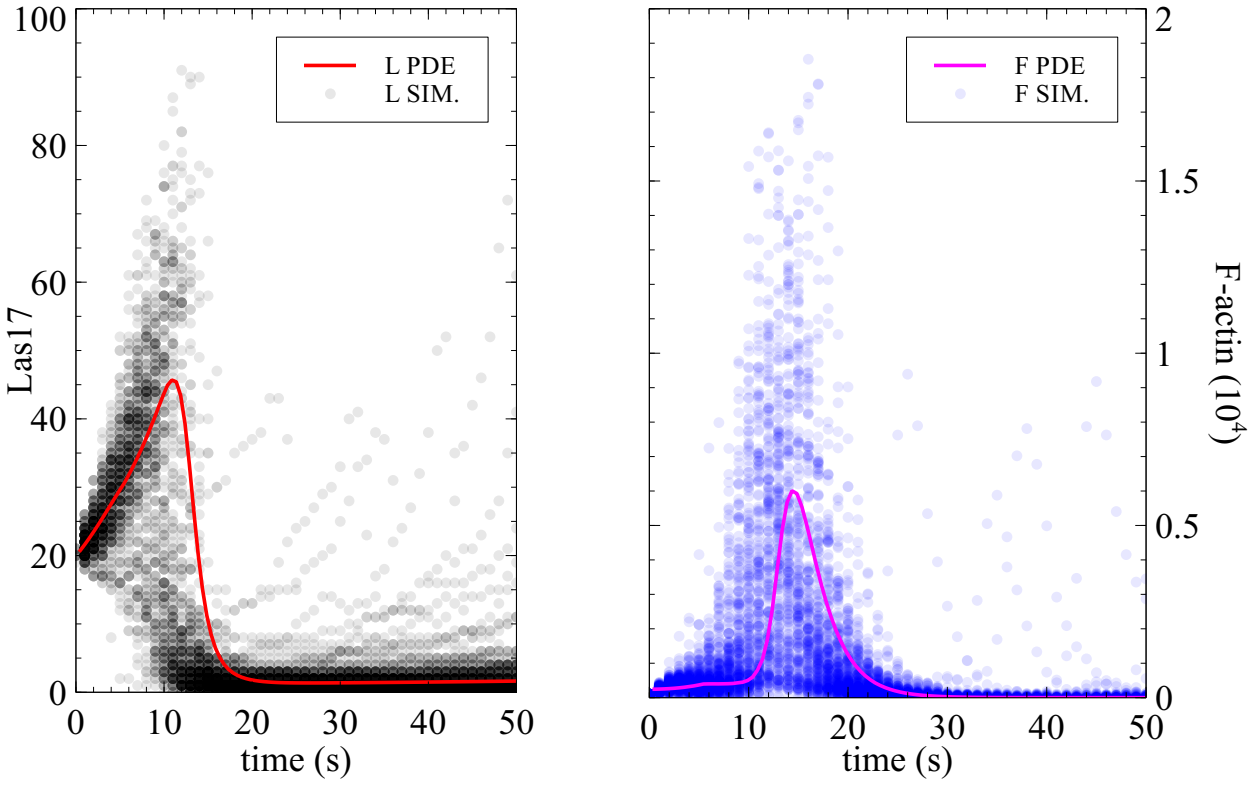

Figure 4.7: PDE model agrees with the stochastic model of Chapter 3.

4.7 Results: PDE Phase Diagram

In this section, we explore the behaviors of the PDE model by varying two parameters at a time. Then, four characteristic properties are calculated, RF, F_{max}, RL and L_{max}. F_{max} and L_{max} are the maximum values of F-actin and Las17 during a given time course. RF is the ratio of the area under the $F(t)$ time course and the product $F_{max} \times t_{tot}$, where t_{tot} is the total time of the time course. RL is defined in the same way for L. RF and RL can be written as

$$RF = \frac{\int_0^{t_{tot}} F(t)\, dt}{F_{max} \times t_{tot}}, \tag{4.14}$$

$$LF = \frac{\int_0^{t_{tot}} L(t)\, dt}{L_{max} \times t_{tot}}. \tag{4.15}$$

Then RF and LF near 1 correspond to persistent patches, values near 0 correspond to transient pulses, and intermediate values correspond to oscillations.

In exploring the possible range of behaviors of the model, we first vary the first two parameters k_{br} and k_0. The results are plotted in Fig. 4.8. In the first row of the RF heat map, we can see a clear transition from single pulse to oscillation, then to permanent patch, as k_{br} decreases. We need to ignore the left two boxes in the top row because F_{max} is too small to obtain a meaningful value of RF (see the F_{max} cold map for reference). In these two cases, the F-actin can not reach the 400 threshold to initiate the turgor pressure force in Eq. 4.7. For the rest of the boxes in the first row, the phase transition is represented by three time courses shown in the figure.

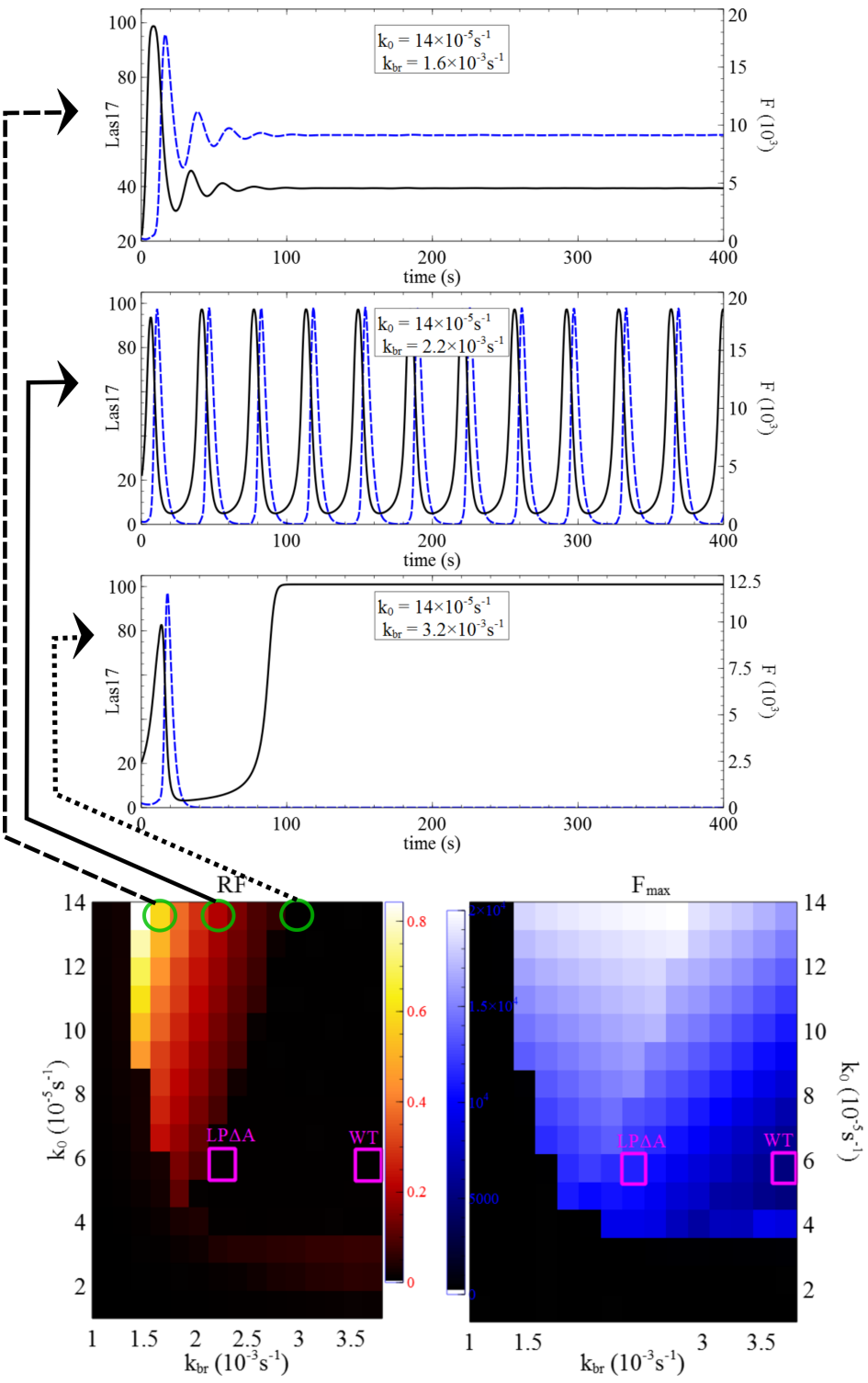

Figure 4.8: hem,eThe phase diagram of F-actin with three characteristic time courses corresponding to three green circle. Two magenta squares mark the wild-type and the *las17*Δ*acidic pan1*Δ*acidic* mutant. $t_{tot} = 1000s$ is used in the calculation. For the time courses, only $400s$ is plotted.

In the top time course, both F and L reach their non-zero steady state. RF is large because the area below the time course is large. In the second time course, both F and L oscillate. RF is medium because F is small for most of the time, despite having repeating spikes. In the third time course, F has a single peak then vanishes, while L also has a single peak but reaches L_2 eventually. RF is low because F is near zero for most of the time except the single peak. L approaches L_2 instead of 0 because of vanishing F, which is the only negative feedback on L. In this chapter, we ignore the spontaneous F-actin nucleation term contained in the stochastic model of Chapter 3, for simplicity. In more realistic cases, F will reappear by spontaneous nucleation. Then L will decrease due to the negative feedback from F. The F_{max} cold map in Fig. 4.8 shows the transition from low to high then to low F_{max} when decreasing k_{br}. Thus the maximum F_{max} is obtained for intermediate k_{br}.

We mark both the wild-type point and the *las17*Δ*acidic pan1*Δ*acidic* mutant point in the heat and cold maps . We see that F_{max} is larger in the *las17*Δ*acidic pan1*Δ*acidic* box than in the wild-type box, which agrees with the result in Chapter 3. A comparable difference is not seen in RL or the L_{max} map (Fig. 4.9) because L eventually reaches L_2 in both cases. However, the single peak of L is higher in the *las17*Δ*acidic pan1*Δ*acidic* mutant than the wild-type. Interestingly, the heat map of RL is opposite to the heat map of RF. But the phase transition is similarly clear. However, we note that the high asymptotic value of L may be an artifact of our simplifications.

Varying the two parameters α and f_{tp} also gives a phase transition. The results for F are shown in Fig. 4.10. We mark the wild-type point and a point corresponding to the *sla2*Δ

mutant on the heat maps. We see that both RF and F_{max} are larger at the *sla2*Δ point, which agrees with Chapter 3 in that the *sla2*Δ mutant gives a large and permanent patch of F-actin.

Overall, we see a phase transition of the PDE model that resembles the Hopf bifurcation, in the sense of a transition from static to oscillating behavior. Various results from the PDE model match the previous ones in Chapter 3. The PDE model provides a powerful tool to explore the possible behaviors of the system.

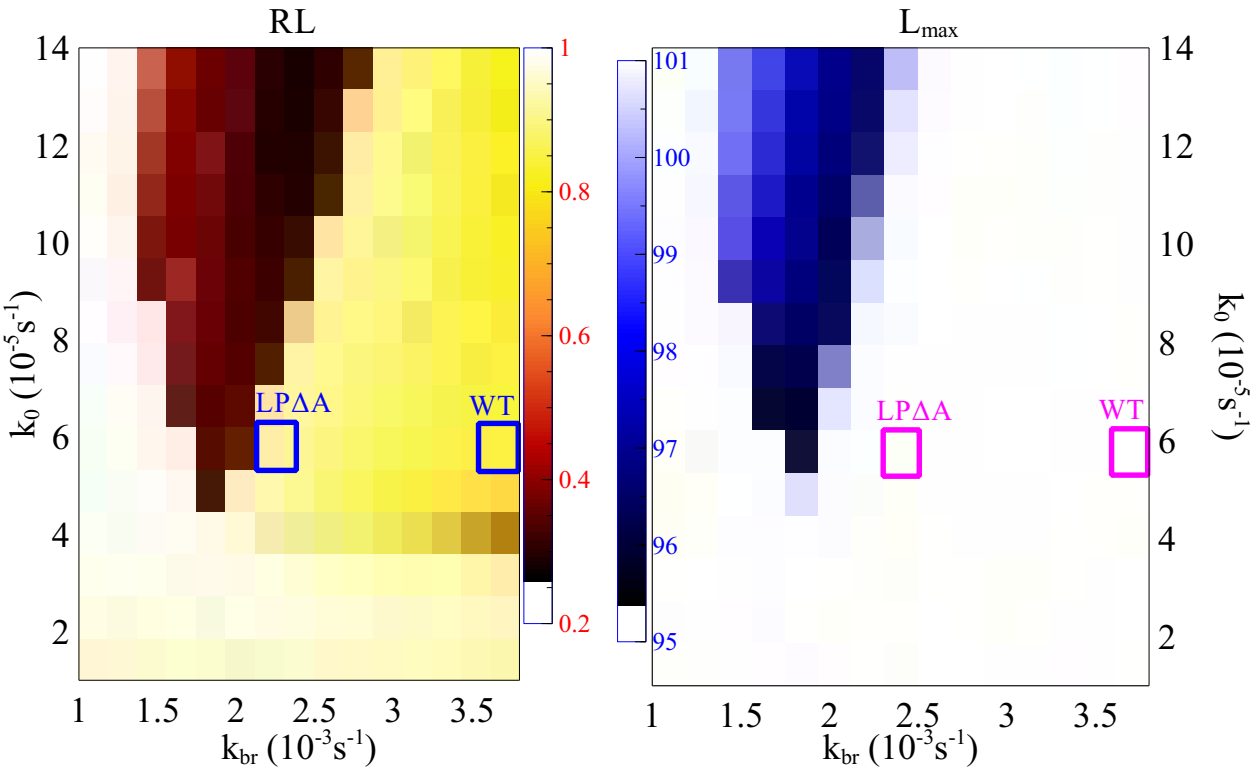

Figure 4.9: Phase diagram of Las17 with varying k_{br} and k_0. Symbols are as in Fig. 4.8.

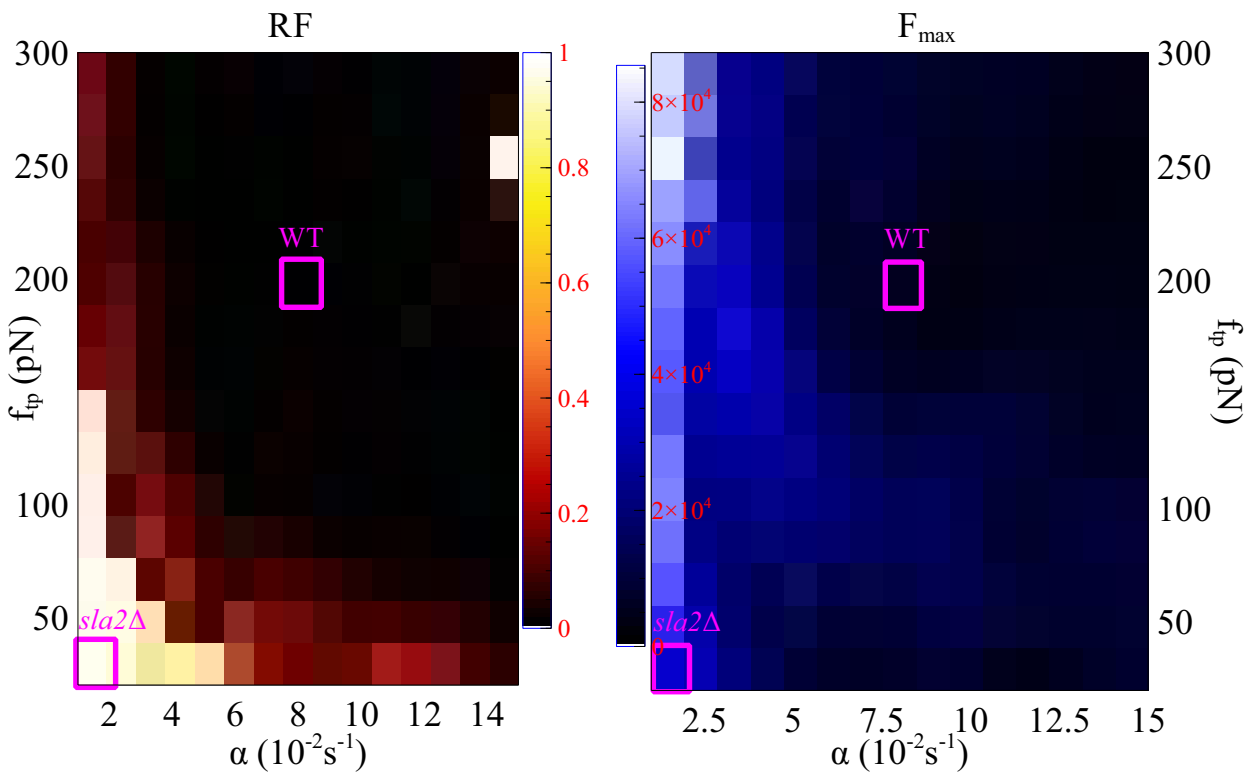

Figure 4.10: Phase diagram of F-actin with varying α and f_{tp}. Two magenta squares mark the wild-type, and the *sla2*Δ mutant.

4.8 Conclusion

In this chapter, we have developed a model of the actin network based on partial differential equations. The PDE model is more realistic than the ODE model in Chapter 3 because the PDE model includes the branching layer, the force layer and the Brownian ratchet effect. On the other hand, the PDE model is much easier to solve than the stochastic model in Chapter 3. There is no need for calculating the ensemble average to get meaningful results. In addition, the PDE is more precise than the stochastic one when exploring the parameter space. Because the PDE is deterministic, it can precisely differentiate steady states from

oscillations, while the stochastic one has difficulties in making this distinction due to its random nature.

In short, the PDE model is a well balanced model between realism and computational load. The new behavior predicted by the PDE model is of high interest for predicting results of experiments yet to be performed.

Chapter 5

CONCLUSIONS AND FUTURE WORK

5.1 Conclusions

Actin plays central roles in cell migration and endocytosis. First, actin functions like a motion switch in cell migration. When subject to a fast global inhibitor, such as membrane tension, the symmetry of actin network can be spontaneously broken. In this case, more actin network assembles at the leading edge than at the trailing edge. The cell thus moves following the leading edge. The cell can change direction by switching the majority of the actin network from the leading edge to the trailing edge when large fluctuations or extracellular cues occur. Second, actin functions like a pulse during endocytosis. Actin network assembles at endocytic sites where actin regulators have previously arrived. The feedback interactions among the actin, actin regulators and cell membrane lead to a transient burst of actin network, which disappears after tens of seconds when cargo carried by the vesicle is ready to be released. The pulse behavior is sensitive to various interventions. The actin pulse can be delayed, or even vanish, when the regulators or other important endocytic proteins are mutated.

The origins of the switch function and pulse functions of actin are studied throughly in this thesis. For cell migration, the symmetric distribution of actin network at two ends of a cell is destabilized by small fluctuations when there is large enough membrane tension. Any small difference in filament numbers at the two ends (ΔN) leads to a larger difference in

subunit numbers at the two ends (ΔF). This is because the leading edge has more filaments, thus experiencing smaller force per each filament, while the trailing edge experiences a larger force per filament. According to the Brownian ratchet effect [21], the filaments at the leading edge can polymerize faster to assemble more actin subunits, increasing ΔF. In turn, ΔF causes a larger ΔN because the filaments at the leading edge are longer, and therefore disassemble slower than those filaments at the trailing edge. These two mechanisms behave like the activator-activator switch from Chapter 1.

However, when the membrane tension is not large enough, the asymmetric states vanish and the symmetric state becomes stable again. Because of the small tension, the Brownian ratchet effect is also small. A depolymerization effect dominates the Brownian ratchet effect. The depolymerization effect is based on the fact that the leading edge has more filaments, and thus more barbed ends and pointed ends. The depolymerization happens at those ends. The total depolymerization from all the filaments is thus faster at the leading edge. The depolymerization then diminishes the excessive filaments at the leading edge ΔN by reducing ΔF. The Brownian ratchet effect and the depolymerization effect compete. If the Brownian ratchet effect dominates, then the stationary state is unstable, otherwise the stationary state is stable. The membrane tension enhances the Brownian ratchet effect, and is thus the key to the switch function of the actin network.

For endocytosis, the actin network assembles and then disassembles, during a period of time of about 30 seconds. Regulators that activate the actin network assembly also behave like pulses. Here, actin and its regulators are modeled as an excitable feedback system,

similar to the FitzHugh-Nagumo model [3, 26]. Not only do actin and its regulators behave like pulses, they also have a counter-intuitive behavior. When the regulators are mutated, causing a lower branching rate, even more actin assembles at each endocytic site. Studying this counter-intuitive phenotype, we found that a negative feedback from F-actin on its regulator Las17 is required. The negative feedback is most likely driven by a process in which actin filaments can pull Las17 molecules off the membrane, which then leave the endocytic site. The mechanism behind the phenotype is a combination of two opposing effects. First, when the branching rate is reduced, fewer actin filaments are branched via each Las17 molecule. Second, each Las17 molecule is less likely to be pulled off the membrane by the actin filaments. Overall, for some branching rates, somewhat smaller than the wild-type branching rate, a larger number of "weaker" mutant Las17 molecules help branch more F-actin than the "stronger" but fewer wild-type Las17 molecules. Another feature of the actin and regulator pulses is that the regulator pulse builds up much more slowly than the actin pulse. We found that this feature is fulfilled in our model when actin network assembles autocatalytically. The keys to the correct pulse function of the actin network are thus the negative feedback mechanism that F-actin can pull Las17 off, and the autocatalytic branching of F-actin.

Studying the models for cell migration and endocytosis is challenging because of the complexity of the processes. The stochastic simulation is the most realistic approach. However, it is also the most computationally intense approach. It is thus hard to explore all possible behaviors or fit the stochastic model to experimental data. On the other hand, the ordi-

nary equation (ODE) approach is the most convenient one to calculate. It is easy to fit the ODE model to experiments. However, it is not easy to incorporate all physical or chemical processes, particularly those depending on the spatial distribution of actin. Therefore, the ODE model is sometimes not realistic enough to reveal all possible mechanisms of the actin network.

To overcome these challenges, we developed a partial differential equation (PDE) model that balances computational load and realism. The PDE model is capable of including important mechanisms that are difficult to include in the ODE model, such as the Brownian ratchet effect, the branching layer, and the force layer. On the other hand, the PDE model is much easier to calculate than the stochastic model. Also, there is no need to calculate ensemble averages to obtain meaningful results from the PDE model. The PDE model can also be more accurate than the stochastic model for exploring possible behaviors, such as defining oscillations and stationary states, because the key features are more readily visible. Therefore, the relatively realistic and computationally efficient PDE model opens many opportunities for the studying actin network in various biological processes.

We simplified the PDE model to study endocytosis in Chapter 4. The simplified PDE model has only one spatial dimension, but it matches the experimental data and even the stochastic simulations of Chapter 3 very well. The PDE model also predicts a rich spectrum of possible behaviors like oscillations and steady states of actin and its regulator. The results from the PDE model suggest several possible experiments for verifying the model predictions.

5.2 Future Work

The continuation of the work in this thesis has several possible directions. First, the feedback mechanism between actin and its regulators in Chapter 3/4 could be included in the cell migration model. We used an F-actin-independent nucleation mechanism and constant nucleator count in the model of Chapter 2. However, the autocatalytic branching of F-actin and the negative effect of F-actin on nucleators could be important in cell migration. It will be interesting to explore the spectrum of behaviors in this extended model by varying the branching rate and the membrane tension. In Chapter 2, we saw a second order phase transition when varying the membrane tension coefficient. The symmetric state is stable for small tension coefficient and unstable for large tension coefficient. However, the transition in cell migration could be first order, which means for some parameter values, both the symmetric state and the asymmetric state are stable. In these cases, the cell needs a large excitation to jump from the stable symmetric state to the stable asymmetric state, in order to start migration. Using a similar PDE model as in Chapter 4, this first order transition might be discovered. It will be then clear what physical or chemical properties are required for the first order transition.

Second, in the models of endocytosis, a more detailed interaction mechanism between actin filaments and the Sla2 cap required for exerting pulling forces could be added. At present, the models treat the interaction as a step function. The Sla2 cap is attached to the moving actin network when there is enough actin, and left on the membrane otherwise. The step function mechanism creates artifacts that might be prevented if a smoother interaction

mechanism is used.

Third, some requirements and predictions of the models call for experimental verifications. For example, the possible biological mechanisms that can lead to negative feedback from F-actin on Las17 need to be screened by experiments. Two possible experiments could verify whether the negative feedback is caused by F-actin pulling Las17 molecules off membrane or by membrane curvature generation. First, the curvature effect can be examined if the osmotic pressure can be dramatically increased. The high osmotic pressure can reduce the membrane curvature, and can be achieved by diluting the cell suspension with a medium having low ionic concentration [101]. If the Las17 count still drops and eventually vanishes, then we will know that the membrane curvature can not cause the negative effect. Second, the curvature effect can also be examined if the membrane curvature can be generated without F-actin. We can achieve this requirement by treating the cells with Latrunculin, and then constitutively activating channels that transport glycerol out of the cell, such as Fps1 [130, 131]. This could allow other proteins to create membrane curvature, even without F-actin. In this case, if the Las17 count still drops and eventually vanishes, we will then know that the membrane curvature leads to the negative feedback. Also, the oscillations in actin and regulator counts, seen in Chapter 4, might be observed in experiments with appropriate conditions. For example, we can treat budding yeast cells with varying concentrations of CK-666, a molecule that can interfere with Arp2/3 complex activation, to reduce the branching rate. Some gene transformations might also match the requirement for the oscillations predicted by the PDE model, which is to properly reduce the branching rate and increase the Las17 assembly rate.

Finally, the PDE model developed in Chapter 4 can be viewed as a general growth model. The model can describe biological systems that can grow, in addition to the actin network. For example, the clathrin coat, which can expand and create membrane curvature, might be modeled using a similar PDE. The growth model can also calculate the spatial distribution of polymerized molecules. These molecules diffuse in the cytoplasm and occasionally add to growing polymers of the same type of molecules. It is hard to describe the growth part of this process using the traditional diffusion-reaction equation approach.

In short, the author looks forward to seeing applications and/or expansions of the ideas and methods implemented in this thesis.

BIBLIOGRAPHY

[1] Thomas D Pollard and John A Cooper. Actin, a central player in cell shape and movement. *Science*, 326(5957):1208–1212, 2009.

[2] Xinxin Wang, Brian J Galletta, John A Cooper, and Anders E Carlsson. Actin-regulator feedback interactions during endocytosis. *Biophysical Journal*, 110(6):1430–1443, 2016.

[3] Richard FitzHugh. Impulses and physiological states in theoretical models of nerve membrane. *Biophysical journal*, 1(6):445, 1961.

[4] Alexander B Verkhovsky, Tatyana M Svitkina, and Gary G Borisy. Self-polarization and directional motility of cytoplasm. *Current Biology*, 9(1):11–S1, 1999.

[5] Alexis J Lomakin, Kun-Chun Lee, Sangyoon J Han, Duyen A Bui, Michael Davidson, Alex Mogilner, and Gaudenz Danuser. Competition for actin between two distinct f-actin networks defines a bistable switch for cell polarization. *Nature cell biology*, 2015.

[6] Andrew R Houk, Alexandra Jilkine, Cecile O Mejean, Rostislav Boltyanskiy, Eric R Dufresne, Sigurd B Angenent, Steven J Altschuler, Lani F Wu, and Orion D Weiner. Membrane tension maintains cell polarity by confining signals to the leading edge during neutrophil migration. *Cell*, 148(1):175–188, 2012.

[7] Yuan Xiong, Chuan-Hsiang Huang, Pablo A Iglesias, and Peter N Devreotes. Cells navigate with a local-excitation, global-inhibition-biased excitable network. *Proceedings of the National Academy of Sciences*, 107(40):17079–17086, 2010.

[8] Bruce L Goode, Julian A Eskin, and Beverly Wendland. Actin and endocytosis in budding yeast. *Genetics*, 199(2):315–358, 2015.

[9] Brian J Galletta, Anders E Carlsson, and John A Cooper. Molecular analysis of Arp2/3 complex activation in cells. *Biophysical journal*, 103(10):2145–2156, 2012.

[10] Andrea Picco, Markus Mund, Jonas Ries, François Nédélec, and Marko Kaksonen. Visualizing the functional architecture of the endocytic machinery. *eLife*, 4:e04535, 2015.

[11] Michael E Young, John A Cooper, and Paul C Bridgman. Yeast actin patches are networks of branched actin filaments. *The Journal of cell biology*, 166(5):629–635, 2004.

[12] Fatima-Zahra Idrissi, Anabel Blasco, Anna Espinal, and María Isabel Geli. Ultrastructural dynamics of proteins involved in endocytic budding. *Proceedings of the National Academy of Sciences*, 109(39):E2587–E2594, 2012.

[13] Vladimir Sirotkin, Julien Berro, Keely Macmillan, Lindsey Zhao, and Thomas D Pollard. Quantitative analysis of the mechanism of endocytic actin patch assembly and disassembly in fission yeast. *Molecular biology of the cell*, 21(16):2894–2904, 2010.

[14] Yidi Sun, Adam C Martin, and David G Drubin. Endocytic internalization in budding yeast requires coordinated actin nucleation and myosin motor activity. *Developmental cell*, 11(1):33–46, 2006.

[15] Jian Liu, Yidi Sun, David G Drubin, and George F Oster. The mechanochemistry of endocytosis. *PLoS Biol*, 7(9):e1000204, 2009.

[16] Julien Berro, Vladimir Sirotkin, and Thomas D Pollard. Mathematical modeling of endocytic actin patch kinetics in fission yeast: disassembly requires release of actin filament fragments. *Molecular biology of the cell*, 21(16):2905–2915, 2010.

[17] Daniel Irimia, Guillaume Charras, Nitin Agrawal, Timothy Mitchison, and Mehmet Toner. Polar stimulation and constrained cell migration in microfluidic channels. *Lab on a Chip*, 7(12):1783–1790, 2007.

[18] Wanda Kukulski, Martin Schorb, Marko Kaksonen, and John AG Briggs. Plasma membrane reshaping during endocytosis is revealed by time-resolved electron tomography. *Cell*, 150(3):508–520, 2012.

[19] Uri Alon. *An introduction to systems biology: design principles of biological circuits*. CRC press, 2006.

[20] Benjamin A Smith, Shae B Padrick, Lynda K Doolittle, Karen Daugherty-Clarke, Ivan R Corrêa, Ming-Qun Xu, Bruce L Goode, Michael K Rosen, and Jeff Gelles. Three-color single molecule imaging shows WASP detachment from Arp2/3 complex triggers actin filament branch formation. *Elife*, 2:e01008, 2013.

[21] Charles S Peskin, Garrett M Odell, and George F Oster. Cellular motions and thermal fluctuations: the brownian ratchet. *Biophysical journal*, 65(1):316, 1993.

[22] Anders E Carlsson. Growth of branched actin networks against obstacles. *Biophysical journal*, 81(4):1907–1923, 2001.

[23] Joshua L Cherry and Frederick R Adler. How to make a biological switch. *Journal of theoretical biology*, 203(2):117–133, 2000.

[24] Timothy S Gardner, Charles R Cantor, and James J Collins. Construction of a genetic toggle switch in escherichia coli. *Nature*, 403(6767):339–342, 2000.

[25] Steven H Strogatz. *Nonlinear dynamics and chaos: with applications to physics, biology, chemistry, and engineering*. Westview press, 2014.

[26] Jinichi Nagumo, Suguru Arimoto, and Shuji Yoshizawa. An active pulse transmission line simulating nerve axon. *Proceedings of the IRE*, 50(10):2061–2070, 1962.

[27] R Sambeth and A Baumgaertner. Autocatalytic polymerization generates persistent random walk of crawling cells. *Physical review letters*, 86(22):5196, 2001.

[28] Michael M Kozlov and Alex Mogilner. Model of polarization and bistability of cell fragments. *Biophysical journal*, 93(11):3811–3819, 2007.

[29] Marko Kaksonen, Yidi Sun, and David G Drubin. A pathway for association of receptors, adaptors, and actin during endocytic internalization. *Cell*, 115(4):475–487, 2003.

[30] Roshni Basu and Fred Chang. Characterization of dip1p reveals a switch in Arp2/3-dependent actin assembly for fission yeast endocytosis. *Current Biology*, 21(11):905–916, 2011.

[31] Serge Dmitrieff and François Nédélec. Membrane mechanics of endocytosis in cells with turgor. *PLoS Comput Biol*, 11(10):e1004538, 2015.

[32] John Innes Centre. `//https://www.jic.ac.uk/microscopy/more/T5_9.htm`.

[33] Dong Li, Lin Shao, Bi-Chang Chen, Xi Zhang, Mingshu Zhang, Brian Moses, Daniel E Milkie, Jordan R Beach, John A Hammer, Mithun Pasham, et al. Extended-resolution structured illumination imaging of endocytic and cytoskeletal dynamics. *Science*, 349(6251):aab3500, 2015.

[34] Ori Avinoam, Martin Schorb, Carsten J Beese, John AG Briggs, and Marko Kaksonen. Endocytic sites mature by continuous bending and remodeling of the clathrin coat. *Science*, 348(6241):1369–1372, 2015.

[35] R Dyche Mullins. Cytoskeletal mechanisms for breaking cellular symmetry. *Cold Spring Harbor perspectives in biology*, 2(1):a003392, 2010.

[36] Xingyu Jiang, Derek A Bruzewicz, Amy P Wong, Matthieu Piel, and George M Whitesides. Directing cell migration with asymmetric micropatterns. *Proceedings of the National Academy of Sciences of the United States of America*, 102(4):975–978, 2005.

[37] Pablo A Iglesias and Peter N Devreotes. Navigating through models of chemotaxis. *Current opinion in cell biology*, 20(1):35–40, 2008.

[38] Matthew D Onsum and Christopher V Rao. Calling heads from tails: the role of mathematical modeling in understanding cell polarization. *Current opinion in cell biology*, 21(1):74–81, 2009.

[39] Alexandra Jilkine and Leah Edelstein-Keshet. A comparison of mathematical models for polarization of single eukaryotic cells in response to guided cues. *PLoS computational biology*, 7(4):e1001121, 2011.

[40] Alex Mogilner, Jun Allard, and Roy Wollman. Cell polarity: quantitative modeling as a tool in cell biology. *Science*, 336(6078):175–179, 2012.

[41] Alex Mogilner and Jie Zhu. Cell polarity: tension quenches the rear. *Current Biology*, 22(2):R48–R51, 2012.

[42] Nathan W Goehring and Stephan W Grill. Cell polarity: mechanochemical patterning. *Trends in cell biology*, 2012.

[43] AM Turing. The chemical basis of morphogenesis. *Philosophical Transactions of the Royal Society of London. Series B, Biological Sciences*, 237(641):37–72, 1952.

[44] Adriana T Dawes and Leah Edelstein-Keshet. Phosphoinositides and rho proteins spatially regulate actin polymerization to initiate and maintain directed movement in a one-dimensional model of a motile cell. *Biophysical journal*, 92(3):744–768, 2007.

[45] Alexander van Oudenaarden and Julie A Theriot. Cooperative symmetry-breaking by actin polymerization in a model for cell motility. *Nature cell biology*, 1(8):493–499, 1999.

[46] Noa Ofer, Alexander Mogilner, and Kinneret Keren. Actin disassembly clock determines shape and speed of lamellipodial fragments. *Proceedings of the National Academy of Sciences*, 108(51):20394–20399, 2011.

[47] Danying Shao, Herbert Levine, and Wouter-Jan Rappel. Coupling actin flow, adhesion, and morphology in a computational cell motility model. *Proceedings of the National Academy of Sciences*, 109(18):6851–6856, 2012.

[48] Thomas D Pollard and Gary G Borisy. Cellular motility driven by assembly and disassembly of actin filaments. *Cell*, 112(4):453–465, 2003.

[49] Igor L Novak, Boris M Slepchenko, and Alex Mogilner. Quantitative analysis of g-actin transport in motile cells. *Biophysical journal*, 95(4):1627–1638, 2008.

[50] JL McGrath, Y Tardy, CF Dewey Jr, JJ Meister, and JH Hartwig. Simultaneous measurements of actin filament turnover, filament fraction, and monomer diffusion in endothelial cells. *Biophysical journal*, 75(4):2070–2078, 1998.

[51] Tatyana M Svitkina and Gary G Borisy. Arp2/3 complex and actin depolymerizing factor/cofilin in dendritic organization and treadmilling of actin filament array in lamellipodia. *The Journal of cell biology*, 145(5):1009–1026, 1999.

[52] Tatyana M Svitkina, Alexander B Verkhovsky, Kyle M McQuade, and Gary G Borisy. Analysis of the actin–myosin ii system in fish epidermal keratocytes: mechanism of cell body translocation. *The Journal of cell biology*, 139(2):397–415, 1997.

[53] Daniel T Gillespie. Exact stochastic simulation of coupled chemical reactions. *The journal of physical chemistry*, 81(25):2340–2361, 1977.

[54] A E Carlsson, M A Wear, and J A Cooper. End versus side branching by Arp2/3 complex. *Biophysical journal*, 86(2):1074–1081, 2004.

[55] Jie Zhu and A E Carlsson. Growth of attached actin filaments. *The European Physical Journal E*, 21(3):209–222, 2006.

[56] Ikuko Fujiwara, Shin Takahashi, Hisashi Tadakuma, Takashi Funatsu, and Shin'ichi Ishiwata. Microscopic analysis of polymerization dynamics with individual actin filaments. *Nature cell biology*, 4(9):666–673, 2002.

[57] K Doubrovinski and K Kruse. Self-organization of treadmilling filaments. *Physical review letters*, 99(22):228104, 2007.

[58] Fumio Oosawa and Sho Asakura. *Thermodynamics of the Polymerization of Protein*. Academic Press, New York, 1975.

[59] Thomas D Pollard. Rate constants for the reactions of ATP-and ADP-actin with the ends of actin filaments. *The Journal of cell biology*, 103(6):2747–2754, 1986.

[60] Tom Shemesh, Benjamin Geiger, Alexander D Bershadsky, and Michael M Kozlov. Focal adhesions as mechanosensors: a physical mechanism. *Proceedings of the National Academy of Sciences of the United States of America*, 102(35):12383–12388, 2005.

[61] Fei Wang, Paul Herzmark, Orion D Weiner, Supriya Srinivasan, Guy Servant, and Henry R Bourne. Lipid products of PI(3)Ks maintain persistent cell polarity and directed motility in neutrophils. *Nature cell biology*, 4(7):513–518, 2002.

[62] Christian Westendorf, Jose Negrete, Albert J Bae, Rabea Sandmann, Eberhard Bodenschatz, and Carsten Beta. Actin cytoskeleton of chemotactic amoebae operates close to the onset of oscillations. *Proceedings of the National Academy of Sciences*, 110(10):3853–3858, 2013.

[63] John Condeelis. How is actin polymerization nucleated *in vivo? Trends in cell biology*, 11(7):288–293, 2001.

[64] A E Carlsson. Stimulation of actin polymerization by filament severing. *Biophysical journal*, 90(2):413–422, 2006.

[65] Fabian Heinemann, Holger Doschke, and Manfred Radmacher. Keratocyte lamellipodial protrusion is characterized by a concave force-velocity relation. *Biophysical journal*, 100(6):1420–1427, 2011.

[66] Jun Allard and Alex Mogilner. Traveling waves in actin dynamics and cell motility. *Current opinion in cell biology*, 25(1):107–115, 2013.

[67] Jonathon A Ditlev, Nathaniel M Vacanti, Igor L Novak, and Leslie M Loew. An open model of actin dendritic nucleation. *Biophysical journal*, 96(9):3529–3542, 2009.

[68] Harvey T McMahon and Emmanuel Boucrot. Molecular mechanism and physiological functions of clathrin-mediated endocytosis. *Nature reviews Molecular cell biology*, 12(8):517–533, 2011.

[69] Jasper Weinberg and David G Drubin. Clathrin-mediated endocytosis in budding yeast. *Trends in cell biology*, 22(1):1–13, 2012.

[70] Olivia L Mooren, Brian J Galletta, and John A Cooper. Roles for actin assembly in endocytosis. *Annual review of biochemistry*, 81:661–686, 2012.

[71] Steeve Boulant, Comert Kural, Jean-Christophe Zeeh, Florent Ubelmann, and Tomas Kirchhausen. Actin dynamics counteract membrane tension during clathrin-mediated endocytosis. *Nature cell biology*, 13(9):1124–1131, 2011.

[72] Marko Kaksonen, Christopher P. Toret, and David G. Drubin. A modular design for the clathrin- and actin-mediated endocytosis machinery. *Cell*, 123:305–320, 2005.

[73] Thomas A Burke, Jenna R Christensen, Elisabeth Barone, Cristian Suarez, Vladimir Sirotkin, and David R Kovar. Homeostatic actin cytoskeleton networks are regulated by assembly factor competition for monomers. *Current Biology*, 24(5):579–585, 2014.

[74] Michal Skruzny, Thorsten Brach, Rodolfo Ciuffa, Sofia Rybina, Malte Wachsmuth, and Marko Kaksonen. Molecular basis for coupling the plasma membrane to the actin cytoskeleton during clathrin-mediated endocytosis. *Proceedings of the National Academy of Sciences*, 109(38):E2533–E2542, 2012.

[75] Pilong Li, Sudeep Banjade, Hui-Chun Cheng, Soyeon Kim, Baoyu Chen, Liang Guo, Marc Llaguno, Javoris V Hollingsworth, David S King, Salman F Banani, et al. Phase transitions in the assembly of multivalent signalling proteins. *Nature*, 483(7389):336–340, 2012.

[76] Sudeep Banjade and Michael K Rosen. Phase transitions of multivalent proteins can promote clustering of membrane receptors. *eLife*, 3:e04123, 2014.

[77] Ammar Madania, Pascal Dumoulin, Sandrine Grava, Hiroko Kitamoto, Claudia Schärer-Brodbeck, Alexandre Soulard, Violaine Moreau, and Barbara Winsor. The saccharomyces cerevisiae homologue of human wiskott–aldrich syndrome protein las17p interacts with the arp2/3 complex. *Molecular Biology of the Cell*, 10(10):3521–3538, 1999.

[78] Roshni Basu and Fred Chang. Characterization of dip1p reveals a switch in arp2/3-dependent actin assembly for fission yeast endocytosis. *Current Biology*, 21(11):905–916, 2011.

[79] Qian Chen and Thomas D Pollard. Actin filament severing by cofilin dismantles actin patches and produces mother filaments for new patches. *Current Biology*, 23(13):1154–1162, 2013.

[80] Roshni Basu, Emilia Laura Munteanu, and Fred Chang. Role of turgor pressure in endocytosis in fission yeast. *Molecular biology of the cell*, 25(5):679–687, 2014.

[81] Orion D Weiner, William A Marganski, Lani F Wu, Steven J Altschuler, and Marc W Kirschner. An actin-based wave generator organizes cell motility. *PLoS biology*, 5(9):e221, 2007.

[82] Arthur Millius, Naoki Watanabe, and Orion D Weiner. Diffusion, capture and recycling of SCAR/WAVE and Arp2/3 complexes observed in cells by single-molecule imaging. *Journal of cell science*, 125(5):1165–1176, 2012.

[83] Carl Co, Derek T Wong, Sarah Gierke, Vicky Chang, and Jack Taunton. Mechanism of actin network attachment to moving membranes: barbed end capture by N-WASP WH2 domains. *Cell*, 128(5):901–913, 2007.

[84] Agnieszka N Urbanek, Adam P Smith, Ellen G Allwood, Wesley I Booth, and Kathryn R Ayscough. A novel actin-binding motif in las17/wasp nucleates actin filaments independently of arp2/3. *Current Biology*, 23(3):196–203, 2013.

[85] Mohammed Saleem, Sandrine Morlot, Annika Hohendahl, John Manzi, Martin Lenz, and Aurélien Roux. A balance between membrane elasticity and polymerization energy sets the shape of spherical clathrin coats. *Nature communications*, 6, 2015.

[86] Kazuya Tsujita, Tadaomi Takenawa, and Toshiki Itoh. Feedback regulation between plasma membrane tension and membrane-bending proteins organizes cell polarity during leading edge formation. *Nature cell biology*, 2015.

[87] Kazunari Takano, Kiminori Toyooka, and Shiro Suetsugu. EFC/F-BAR proteins and the N-WASP–WIP complex induce membrane curvature-dependent actin polymerization. *The EMBO journal*, 27(21):2817–2828, 2008.

[88] Yidi Sun, Susheela Carroll, Marko Kaksonen, Junko Y Toshima, and David G Drubin. PtdIns(4,5)P2 turnover is required for multiple stages during clathrin-and actin-dependent endocytic internalization. *The Journal of cell biology*, 177(2):355–367, 2007.

[89] Christopher J Stefan, Steven M Padilla, Anjon Audhya, and Scott D Emr. The phosphoinositide phosphatase Sjl2 is recruited to cortical actin patches in the control of vesicle formation and fission during endocytosis. *Molecular and cellular biology*, 25(8):2910–2923, 2005.

[90] Hasna Ahyayauch, Ana V Villar, Alicia Alonso, and Félix M Goñi. Modulation of PI-specific phospholipase C by membrane curvature and molecular order. *Biochemistry*, 44(34):11592–11600, 2005.

[91] Anders E Carlsson. Dendritic actin filament nucleation causes traveling waves and patches. *Physical review letters*, 104(22):228102, 2010.

[92] K Doubrovinski and K Kruse. Cytoskeletal waves in the absence of molecular motors. *EPL (Europhysics Letters)*, 83(1):18003, 2008.

[93] WR Holmes, AE Carlsson, and L Edelstein-Keshet. Regimes of wave type patterning driven by refractory actin feedback: transition from static polarization to dynamic wave behaviour. *Physical biology*, 9(4):046005, 2012.

[94] Gillian L Ryan, Heather M Petroccia, Naoki Watanabe, and Dimitrios Vavylonis. Excitable actin dynamics in lamellipodial protrusion and retraction. *Biophysical journal*, 102(7):1493–1502, 2012.

[95] Anders E Carlsson and Philip V Bayly. Force generation by endocytic actin patches in budding yeast. *Biophysical journal*, 106(8):1596–1606, 2014.

[96] Marko Kaksonen, Christopher P Toret, and David G Drubin. Harnessing actin dynamics for clathrin-mediated endocytosis. *Nature Reviews Molecular cell biology*, 7(6):404–414, 2006.

[97] Brian J Galletta and John A Cooper. Actin and endocytosis: mechanisms and phylogeny. *Current opinion in cell biology*, 21(1):20–27, 2009.

[98] Fatima-Zahra Idrissi, Helga Grötsch, Isabel M Fernández-Golbano, Cristina Presciatto-Baschong, Howard Riezman, and María-Isabel Geli. Distinct acto/myosin-i structures associate with endocytic profiles at the plasma membrane. *The Journal of cell biology*, 180(6):1219–1232, 2008.

[99] Ina Weisswange, Timothy P Newsome, Sibylle Schleich, and Michael Way. The rate of N-WASP exchange limits the extent of Arp2/3-complex-dependent actin-based motility. *Nature*, 458(7234):87–91, 2009.

[100] George H Duffey. *Physical Chemistry*. McGraw Hill, New York, 1982.

[101] Soheil Aghamohammadzadeh and Kathryn R Ayscough. Differential requirements for actin during yeast and mammalian endocytosis. *Nature cell biology*, 11(8):1039–1042, 2009.

[102] IM De Marañon, Pierre-André Marechal, and Patrick Gervais. Passive response of *Saccharomyces cerevisiae* to osmotic shifts: cell volume variations depending on the physiological state. *Biochemical and biophysical research communications*, 227:519–523, 1996.

[103] Jörg Schaber, Miquel Àngel Adrover, Emma Eriksson, Serge Pelet, Elzbieta Petelenz-Kurdziel, Dagmara Klein, Francesc Posas, Mattias Goksör, Mathias Peter, Stefan Hohmann, et al. Biophysical properties of *Saccharomyces cerevisiae* and their relationship with hog pathway activation. *European Biophysics Journal*, 39(11):1547–1556, 2010.

[104] Nicolas Minc, Arezki Boudaoud, and Fred Chang. Mechanical forces of fission yeast growth. *Current Biology*, 19(13):1096–1101, 2009.

[105] CUDA Toolkit. //https://developer.nvidia.com/cuda-toolkit.

[106] Vérane Achard, Jean-Louis Martiel, Alphée Michelot, Christophe Guérin, Anne-Cécile Reymann, Laurent Blanchoin, and Rajaa Boujemaa-Paterski. A primer-based mechanism underlies branched actin filament network formation and motility. *Current biology*, 20(5):423–428, 2010.

[107] Agnieszka Collins, Anthony Warrington, Kenneth A Taylor, and Tatyana Svitkina. Structural organization of the actin cytoskeleton at sites of clathrin-mediated endocytosis. *Curr. Biol.*, 21(14):1167–1175, 2011.

[108] Dirk Winter, Terry Lechler, and Rong Li. Activation of the yeast Arp2/3 complex by Bee1p, a WASP-family protein. *Current biology*, 9(9):501–505, 1999.

[109] Rajat Rohatgi, Le Ma, Hiroaki Miki, Marco Lopez, Tomas Kirchhausen, Tadaomi Takenawa, and Marc W Kirschner. The interaction between n-wasp and the arp2/3 complex links cdc42-dependent signals to actin assembly. *Cell*, 97(2):221–231, 1999.

[110] Kuo-Kuang Wen and Peter A Rubenstein. Acceleration of yeast actin polymerization by yeast Arp2/3 complex does not require an Arp2/3-activating protein. *Journal of Biological Chemistry*, 280(25):24168–24174, 2005.

[111] Voytek Okreglak and David G Drubin. Cofilin recruitment and function during actin-mediated endocytosis dictated by actin nucleotide state. *The Journal of cell biology*, 178(7):1251–1264, 2007.

[112] Lisa D Belmont and David G Drubin. The yeast v159n actin mutant reveals roles for actin dynamics in vivo. *The Journal of cell biology*, 142(5):1289–1299, 1998.

[113] Meng-Chi Lin, Brian J Galletta, David Sept, and John A Cooper. Overlapping and distinct functions for cofilin, coronin and aip1 in actin dynamics in vivo. *Journal of cell science*, 123(8):1329–1342, 2010.

[114] Pekka Lappalainen and David G Drubin. Cofilin promotes rapid actin filament turnover in vivo. *Nature*, 388(6637):78–82, 1997.

[115] Michal Skruzny, Ambroise Desfosses, Simone Prinz, Svetlana O Dodonova, Anna Gieras, Charlotte Uetrecht, Arjen J Jakobi, Marc Abella, Wim JH Hagen, Joachim Schulz, et al. An organized co-assembly of clathrin adaptors is essential for endocytosis. *Developmental Cell*, 33(2):150–162, 2015.

[116] Sarah L Barker, Linda Lee, B Daniel Pierce, Lymarie Maldonado-Báez, David G Drubin, and Beverly Wendland. Interaction of the endocytic scaffold protein pan1 with the type i myosins contributes to the late stages of endocytosis. *Molecular biology of the cell*, 18(8):2893–2903, 2007.

[117] Howard C. Berg. *Random Walks in Biology*. Princeton University Press, 1993.

[118] Rajesh Arasada and Thomas D Pollard. Distinct roles for f-bar proteins cdc15p and bzz1p in actin polymerization at sites of endocytosis in fission yeast. *Current Biology*, 21(17):1450–1459, 2011.

[119] King Lam Hui, Sae In Kwak, and Arpita Upadhyaya. Adhesion-dependent modulation of actin dynamics in Jurkat T cells. *Cytoskeleton*, 71(2):119–135, 2014.

[120] Till Bretschneider, Kurt Anderson, Mary Ecke, Annette Müller-Taubenberger, Britta Schroth-Diez, Hellen C Ishikawa-Ankerhold, and Günther Gerisch. The three-dimensional dynamics of actin waves, a model of cytoskeletal self-organization. *Biophysical journal*, 96(7):2888–2900, 2009.

[121] Günther Gerisch, Britta Schroth-Diez, Annette Müller-Taubenberger, and Mary Ecke. PIP3 waves and PTEN dynamics in the emergence of cell polarity. *Biophysical journal*, 103(6):1170–1178, 2012.

[122] Y. Yang, M. Su, and M. Wu. Visualizing collective dynamics of endocytic proteins. *Mol. Biol. Cell*, 25:Abstract 1689, 2014.

[123] David B Hoffman, Chad G Pearson, Tim J Yen, Bonnie J Howell, and ED Salmon. Microtubule-dependent changes in assembly of microtubule motor proteins and mitotic spindle checkpoint proteins at ptk1 kinetochores. *Molecular Biology of the Cell*, 12(7):1995–2009, 2001.

[124] S Blair Hedges and Prachi Shah. Comparison of mode estimation methods and application in molecular clock analysis. *BMC bioinformatics*, 4(1):31, 2003.

[125] C Baker Brachmann, Adrian Davies, Gregory J Cost, Emerita Caputo, Joachim Li, Philip Hieter, and JD Boeke. Designer deletion strains derived from *Saccharomyces cerevisiae* S288C: a useful set of strains and plasmids for PCR-mediated gene disruption and other applications. *YEAST-CHICHESTER-*, 14:115–132, 1998.

[126] Mark A Sheff and Kurt S Thorn. Optimized cassettes for fluorescent protein tagging in *Saccharomyces cerevisiae*. *Yeast*, 21(8):661–670, 2004.

[127] Brian J Galletta, Dennis Y Chuang, and John A Cooper. Distinct roles for Arp2/3 regulators in actin assembly and endocytosis. *PLoS biology*, 6(1):e1, 2008.

[128] James A Waddle, Tatiana S Karpova, Robert H Waterston, and John A Cooper. Movement of cortical actin patches in yeast. *The Journal of cell biology*, 132(5):861–870, 1996.

[129] Yasushi Hiraoka, John W Sedat, and David A Agard. Determination of three-dimensional imaging properties of a light microscope system. partial confocal behavior in epifluorescence microscopy. *Biophysical journal*, 57(2):325, 1990.

[130] Simon Avery, Malcolm Stratford, and Pieter Van West. *Stress in yeasts and filamentous fungi*, volume 27. Academic Press, 2007.

[131] Markus J Tamás, Kattie Luyten, F Chris W Sutherland, Agustin Hernandez, Jacobus Albertyn, Hadi Valadi, Hong Li, Bernard A Prior, Stephanus G Kilian, Jose Ramos, et al. Fps1p controls the accumulation and release of the compatible solute glycerol in yeast osmoregulation. *Molecular microbiology*, 31(4):1087–1104, 1999.

[132] Chiharu Higashida, Tai Kiuchi, Yushi Akiba, Hiroaki Mizuno, Masahiro Maruoka, Shuh Narumiya, Kensaku Mizuno, and Naoki Watanabe. F-and g-actin homeostasis regulates mechanosensitive actin nucleation by formins. *Nature cell biology*, 15(4):395–405, 2013.

[133] Sujata Guha Roy, Yasuhiro Nozaki, and Sem H Phan. Regulation of α-smooth muscle actin gene expression in myofibroblast differentiation from rat lung fibroblasts. *The international journal of biochemistry & cell biology*, 33(7):723–734, 2001.

[134] James R Bamburg and O'Neil P Wiggan. Adf/cofilin and actin dynamics in disease. *Trends in cell biology*, 12(12):598–605, 2002.

[135] Mary Katherine Bradford, Karen Whitworth, and Beverly Wendland. Pan1 regulates transitions between stages of clathrin-mediated endocytosis. *Molecular biology of the cell*, 26(7):1371–1385, 2015.

[136] Günther Gerisch, Mary Ecke, Britta Schroth-Diez, Silke Gerwig, Ulrike Engel, Lucinda Maddera, and Margaret Clarke. Self-organizing actin waves as planar phagocytic cup structures. *Cell adhesion and migration*, 3(4):373–382, 2009.

[137] Jiro Toshima, Junko Y Toshima, Mara C Duncan, M Jamie TV Cope, Yidi Sun, Adam C Martin, Scott Anderson, John R Yates, Kensaku Mizuno, and David G Drubin. Negative regulation of yeast eps15-like arp2/3 complex activator, pan1p, by the hip1r-related protein, sla2p, during endocytosis. *Molecular biology of the cell*, 18(2):658–668, 2007.

[138] Yoichiro Mori, Alexandra Jilkine, and Leah Edelstein-Keshet. Wave-pinning and cell polarity from a bistable reaction-diffusion system. *Biophysical journal*, 94(9):3684–3697, 2008.

[139] Daniel Feliciano and Santiago M Di Pietro. Slac, a complex between sla1 and las17, regulates actin polymerization during clathrin-mediated endocytosis. *Molecular biology of the cell*, 23(21):4256–4272, 2012.

[140] Adam C Martin, Matthew D Welch, and David G Drubin. Arp2/3 atp hydrolysis-catalysed branch dissociation is critical for endocytic force generation. *Nature cell biology*, 8(8):826–833, 2006.